QUASIELASTIC NEUTRON SCATTERING STUDY ON THE DYNAMICAL PROPERTIES OF AN AROMATIC HYDROGEN BOND

vorgelegt von
Master of Science
Niina Jalarvo
aus Finnland

Fakultät II – Mathematik und Naturwissenschaften
der Technischen Universität Berlin
zur Erlangung des akademischen Grades
Doktor der Naturwissenschaften

genehmigte Dissertation

Promotionsausschuss:
Vorsitzender: Prof. Dr. Siegfried Hess
Berichter/Gutachter: Prof. Dr. Ferenc Mezei
Berichter/Gutachter: Dr. Arnaud Desmedt von der Université Bordeaux I - CNRS

Tag der Wissenschaftlichen Aussprache: 14.6.2005

Berlin 2005

D 83

Zusammenfassung

Im Rahmen der vorliegenden Dissertation wurden die dynamischen Eigenschaften von aromatischen Wasserstoffverbindungen am Beispiel eines typischen Vertreters, Ammonium Tetraphenylborat (ATPB), mit Hilfe von quasielastischer inkohärenter Neutronenstreuung (QENS) in einem breiten Temperaturbereich ($20 \leq T \leq 350K$) untersucht. In ATPB ist ein Ammonium-Kation zwischen vier Phenylringen benachbarter Tetraphenylborat-Anionen eingeschlossen. Dabei dient jeder einzelne Phenylring als ein Wasserstoffbindungsempfänger für das Ammonium-Ion. Zur Reproduktion der QENS-Spektren wurden verschiedene Modelle für die lokalen Diffusionsbewegungen des Ammonium-Ions und des Phenylrings herangezogen.

Die Bewegungen des Ammonium-Ions wurden als kontinuierlicher Übergang von quantenmechanischen Rotationen bei tiefen Temperaturen zu klassischen diffusiven Rotationsbewegungen bei hohen Temperaturen interpretiert. Im Temperaturbereich $67K \leq T \leq 350K$ rotieren die Ammonium-Ionen um eine C_2/C_3-Achse. Die Korrelationszeit variiert für diese Bewegung von 12.5ps bei T=350K bis 1253ps bei T=67K. Als Aktivierungsenergie der Rotationen des Ammonium-Ions wurde 3.2kJ/mol ermittelt. Dies zeigt, dass die Energiebarriere für eine Rotation der Ammonium-Ionen extrem niedrig ist. Bei Temperaturen unterhalb von 67K wurden quantenmechanische Rotationen der Ammonium-Ionen beobachtet. Darüber hinaus wurden im Rahmen dieser Studie Librations-Anregungszustände von Ammonium bei 4.3meV und 8.2meV identifiziert.

Bei Temperaturen oberhalb von 200K zeigten sich auf der gemessenen Zeitskala lokale diffusive Orientierungsbewegungen der Phenylringe. Diese Bewegungen werden als Librationen aus der Ebene der Phenylringe heraus bewertet. Umorientierungswinkel und Sprung-Frequenz der Librationen der Phenylringe nehmen bei steigenden Temperaturen zu. Bei Raumtemperatur betrug der Umorientierungswinkel der Librationen der Phenylringe $7 \pm 2^\circ$ und die Korrelationszeit 150 ± 50ps. Dieses Ergebnis lässt die Vorstellungen von aromatischen Wasserstoff-bindungen in einem neuen Licht erscheinen. Die aromatischen Wasserstoffbindungen sind extrem flexibel und ermöglichen sowohl dem Donator als auch dem Akzeptor Umorientierungen.

Abstract

In this work the dynamical properties of a prototypical example of the aromatic hydrogen bond, ammonium tetraphenylborate (ATPB), have been studied by quasielastic incoherent neutron scattering (QENS) in a broad temperature range ($20 \leq T \leq 350K$). In ATPB an ammonium cation is trapped between four phenyl rings of the two adjacent tetraphenylborate anions and each phenyl ring serves as a hydrogen bond acceptor for the ammonium ion. Models for local diffusive motions of reorientation of ammonium and the phenyl rings have been considered to reproduce the QENS spectra.

The motions of the ammonium ions are explained as a continuous transition from quantum–mechanical rotations at low temperatures to classical diffusive rotations at high temperatures. In a temperature range of $67K \leq T \leq 350K$ classical diffusive rotations of the ammonium ions around a C_2/C_3 axis were found. The correlation time for this motion varies from 12.5ps at T=350K to 1253ps at T=67K and the activation energy was determined to be 3.2kJ/mol. This result shows that the ammonium ions have to overcome an exceptionally low barrier to rotate. At temperatures below 67K quantum–mechanical rotations of the ammonium ions were observed. Additionally, in this work excited librational states of ammonium were identified at 4.3meV and 8.2meV.

At temperatures above 200K local diffusive motions of orientation of the phenyl rings were found within the experimental time-window. These motions of the phenyl rings are explained as librations out of the plane. The reorientation angle and the jump rate of the librations of the phenyl rings increase with increasing temperatures. At room temperature the librations of the phenyl rings were found to have a reorientation angle of $7 \pm 2^\circ$ and a correlation time of 150 ± 50ps. This result sheds new light on the phenomenon of aromatic hydrogen bonds showing that they are extremely flexible and allow for reorientation of both, the donor and the acceptor.

Acknowledgements

Completition of this work has been possible because of the suport and assistance received from many people. It is my pleasure to pay due to these people, at least in some small way, through acknowledgement here.

I am sincerely grateful to my supervisor Professor Dr. Ferenc Mezei for giving me the opportunity to work as a member of his department (SF1) at the Hahn-Meitner-Institute and receiving his continuous support, guidance and encouragement.

I also owe my gratitude to my co-supervisor Dr. Ruep E. Lechner for the invaluable discussions, advises and remarks.

Furthermore I express my thanks to Dr. Arnaud Desmedt, for providing great help in the early stages of my postgraduate studies and valuable support during the NEAT experiments.

I am grateful for Professor Dr. Siegfried Hess for his interest and effort for being the chairman of the defence committee.

Several people have been at the group of NEAT-spectrometer during my time as a graduate student. I would like to thank Dr. Margarita Russina, Dr. Jörg Pieper, Dr. Alexanda Buchsteiner and Berndt Urban, as all of them have aided in the completition of this work.

I also owe my thanks to Karen Diederichsen, for her help with many practical problems and especially for her effort to correct my english texts.

Many colleagues have provided valuable support and delighting company duringmy time that I have spended to complete my PhD thesis. I'm thankful for Dr. Heloisa N. Bordallo, Dr. Dimitri Argyriou, Dr. Nadir Aliouane, Dr. Christofer Milne, Dr. Markus Strobl, Dr. Jorge Hernandez-Velasco, Dr. Carlos Fehr, Dr. Olga Russina, Dr. Abdelkrim Chemseddine and Dr. Silke Felber.

I am also grateful to Professor Dr. Jürgen Eckert for the inspiring discussions.

I want to express my warmest thanks to my friend Alexander Zafiriou, for his continuous support, patience and love.

Last, but certainly not the least, I want to express my thanks to my family in Finland, my parents Airi and Jouko Jalarvo, my brother Robert Jalarvo, my grandmothers Irene Lehto and Irma Jalarvo, for their support in all fields of life. Sydämelliset kiitokset kannustuksestanne, tuestanne ja rakkaudestanne näiden vuosien varrella.

Table of contents

1 INTRODUCTION

1.1 Hydrogen bonding – a fascination forever

For the first time the idea of **hydrogen bonding** was presented by Latimer and Rodebush [1] in 1920. Even decades later, H-bonding still fascinates researchers in the fields of physics, chemistry, biology and material science and thus each year thousands of papers are published on this topic. The fundamental importance of the H-bonds is based on their role in molecular association as their functional importance is derived from both thermodynamic and kinetic reasons. Although the H-bond is stronger than most other intermolecular forces, it is much weaker than for instance the ionic bond or the covalent bond. The intermediate energy range that the H-bond covers, allows it to associate or dissociate quickly at ambient temperatures. These characteristics provide conditions which are necessary for biological reactions. On the other hand, the H-bonds are able to control and direct the chemical structures because they possess some degree of orientational preference and sufficient strength. For these reasons, the H-bonding remains as an interesting and significant phenomenon to research.

1.2 The principle of hydrogen bonding

The H-bond is based on an attractive intermolecular interaction that exists between two partial electric charges of opposite polarity. As the name "hydrogen bond" implies, one part of the bond involves a hydrogen atom. The hydrogen atom must be attached to a strongly electronegative atom, like sodium or oxygen, which is called the H-bond donor. This electronegative atom attracts the electron cloud of the hydrogen atom and, by decentralizing the cloud, leaves the hydrogen atom with a positive partial charge. Because of the small size of the hydrogen atom, the partial charge represents a large charge density. An H-bond is formed when subsequently the strong positive charge density attracts a negative partial charge of another atom or molecule, which then becomes the H-bond acceptor. The H-bonds can be described following: X—H...A, where X is the donor and A is the acceptor in the H-bond.

1.3 Definition of aromatic hydrogen bonding

The H-bonds can be classified depending on the nature and the interaction strengths of the donor and the acceptor groups. With respect to the main interest of this work, only the category of π-acceptors will be considered here. In systems with π-electrons, like multiple bonds C≡C and C=C or aromatic rings, the negative charge of their π-electron cloud can serve as an acceptor for the H-bond (a detailed description of the H-bonds with the π-acceptors can be found in literature e.g. [2]). The most important π-acceptors are the phenyl (Ph) groups, which occur in a wide range of chemical substances from organometallic to biological molecules.

The π-electrons of the aromatic rings are localized on the both sides of the flat ring, so that there is a small negative partial charge on the face of the ring and a small positive partial charge on the hydrogen atoms on the edges as shown in ***Fig 1-1.*** The negative partial charge on the face of the phenyl ring can attract a molecule or ion, where the hydrogen atom has a positive partial charge, and thus **an aromatic hydrogen bonding*** arises.

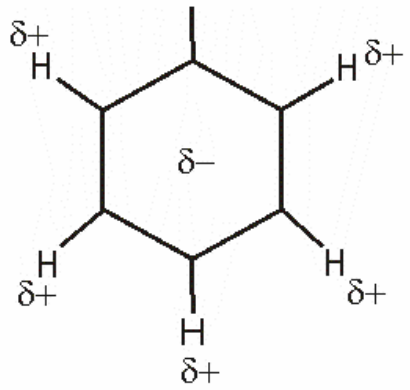

Fig 1-1 *Charge distribution of the phenyl ring.*

* more precisely X–H···Ph

1.4 Aromatic hydrogen bonding in literature

Both theoretical calculations and experimental studies have been performed to understand the nature and the properties of the aromatic H-bonds. Levitt and Perutz have shown in their theoretical study [3] the existence of a significant interaction between an H-bond donor and the centre of an aromatic ring, which is about half as strong as a normal H-bond. A few years later Worth and Wade have performed force-field calculations for an aromatic H-bond, which explained that the potential energy surface is shallow over a very large region, and the donor can move over the entire face of the aromatic ring with only small energy changes [4]. In some structural studies [5], [6], [7] it has been shown that the donor X—H points time average to the midpoint of the aromatic ring, but there are as well examples of very off-centred arrangements, where X—H apparently points to a particular aromatic C—C bond [8] or even to an individual C atom [9]. These results indicate that the directionality of the aromatic H-bond is extremely flexible.

The theoretical calculations for the potential energy minimum of the aromatic H-bond vary roughly from 2kcal/mol to 4kcal/mol. A congruent description of the aromatic H-bonds has not yet been found. Desiraju and Steiner concluded the main absences of such a description in their book *The Weak Hydrogen Bond In Structural Chemistry and Biology* [10]: “So far a concurrent theoretical model for the aromatic H-bond is to be determined, and especially the bond geometry that represents the global energy minimum is still to be established.”

On the other hand a number of studies have been published on the function and significance of aromatic H-bonds in biological systems. In fact, a study of the interactions of drugs with human haemoglobin [11] first suggested that the interaction between an amino group and phenyl rings could be described as an H-bond. This discovery motivated Burley & Petsko [12], [13] to search for similar interactions between 33 highly refined protein structures. They concluded that

such a NH···Ph interaction is more favourable than the typical non-bonding aromatic-aromatic interaction* and it occurs more frequently than random.

Furthermore, several examples have shown that the aromatic H-bonds play a role in both, the protein structure and the ligand binding interactions, as well as in some specific protein-DNA interactions [14], [15], [16] & [17]. It was also shown, that the strength of the aromatic H-bond, which varies between 2 and 4kcal/mol as the existing physical models propose, significantly contributes to the energy of protein stabilization which is in range of 5 to 10 kcal/mol [18]. Finally, determination of a concurrent theoretical model of the aromatic H-bond would shed new light on the question about the role of the aromatic H-bonds in biological systems.

1.5 Ammonium tetraphenylborate

With respect to the aromatic hydrogen bonds, tetraphenylborate salts are a particularly interesting substance class. The tetraphenylborate anion† is a quintessential example of π-acceptors. Bakshi et al. [19] have calculated that in this anion, each phenyl ring caries a delocalized partial charge of 0.19 e, making them very capable aromatic acceptors. In consequence tetraphenyl-borate salts have been extensively used as model systems for studies. The simplest member of this category, ammonium tetraphenylborate‡ (hereafter called ATPB), is a prototypical system to understand aromatic H-bonds.

* about 1-2kcal/mol
† $B(C_6H_5)_4^-$
‡ $NH_4B(C_6H_5)_4$

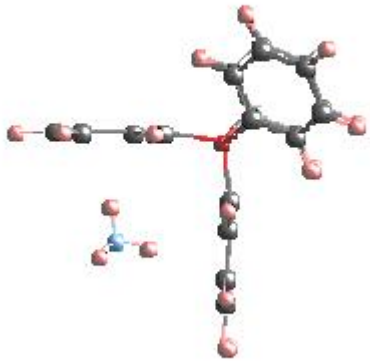

Fig 1-2 *ATPB molecule.*

Steiner *et al*. [6] have characterized the structure of the ATPB by neutron diffraction. An ATPB molecule contains a tetraphenylborate anion and an ammonium cation, like shown in ***Fig 1-2*** . Boron is located in the middle of the anion with the four phenyl rings attached around it. The covalent angles around the B atom are significantly distorted from tetrahedral geometry so that the phenyl groups form pairs of two almost perpendicular aromatic rings.

The ATPB crystals have tetragonal unit cells, with point group $I\bar{4}2m$. The cations and anions are arranged in chains along the tetragonal c axis, like illustrated in ***Fig 1-3***. In these chains two neighbouring $B(C_6H_5)_4^-$ anions form an aromatic cage, inside which the NH_4^+ cation is located. Each of the N^+-H···Ph interactions can form an aromatic H-bond. The chains are arranged in the unit cell as shown in ***Fig 1-4*** . Between the chains, there are short lateral contacts in a diagonal plane of the unit cell. In these contacts, phenyl rings form herringbone-type Ph···Ph interactions.

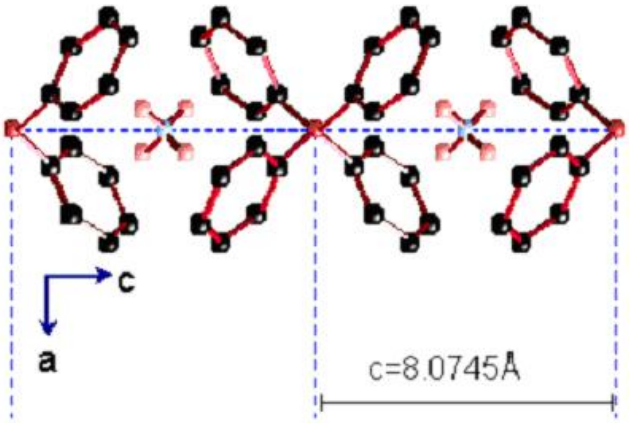

Fig 1-3 *ATPB chain along c-axis.*

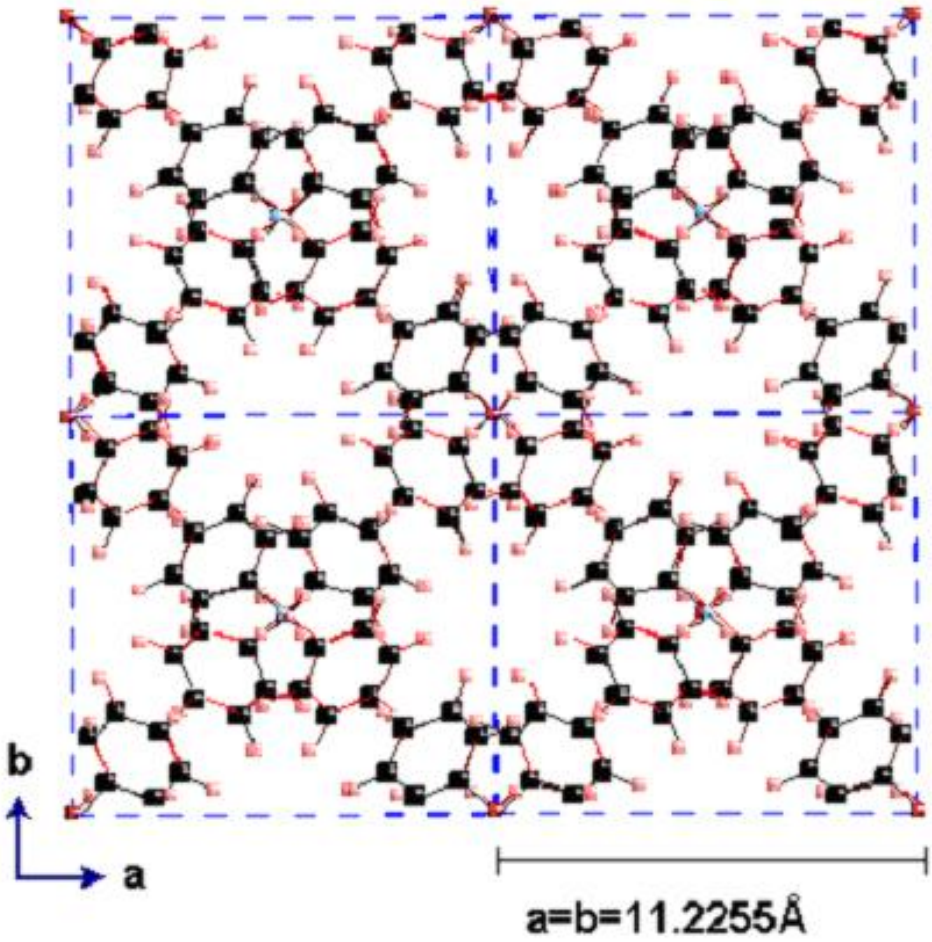

Fig 1-4 *Four unit cells of ATPB*

1.6 Outline of this work

In the following chapter the theoretical aspects of neutron scattering are described in detail. The basic principles of neutron scattering are introduced and the development of the dynamical expressions of neutron scattering is outlined. Special focus is on the quasielastic incoherent neutron scattering. Finally scattering functions for different types of motions are separated.

The third chapter begins with a description of sample preparation. Then the principle of a time-of-flight multichopper spectrometer is introduced, and this is followed by some details about the spectrometer NEAT. Additionally, some aspects of data processing are mentioned in this chapter and specified in ***Appendix*** B. Finally an overview of the measured data is given.

The fourth chapter includes data analysis and results. Several models for both the motions of the ammonium ions and the phenyl rings are developed to interpret the experimental data. Deuteration of the ammonium ion is used as a tool to separate the motions of the phenyl rings from those originating from the ammonium ions. The experimental data were reproduced by the theoretical models which explain the motions of the ammonium ions and the phenyl rings in a broad temperature range.

In the last chapter the results are discussed and an outlook for further investigations is given.

2 THEORETICAL ASPECTS OF NEUTRON SCATTERING

Neutron scattering is a powerful tool to probe the microscopic dynamical and geometrical properties of condensed matter. The energies of cold and thermal neutrons are of the order of microscopic excitations in condensed matter and the wavelengths of cold and thermal neutrons are comparable to the intermolecular distances. Neutrons have no electrical charge and can thus easily and deeply penetrate the material, since there is no Coulomb interaction between the neutrons and the nuclei of the sample.

Quasielastic incoherent neutron scattering (QENS) is an especially appropriate method for the study of the dynamical properties of the ATPB molecules, as it contains many hydrogen atoms, which have the largest incoherent neutron scattering cross section.

2.1 Properties of neutrons

Neutrons are uncharged particles with a mass $m = 1{,}675 \cdot 10^{-24} g$. The energy E of a neutron with a velocity $\vec{v}$ is just its kinetic energy

$E = \frac{1}{2} m\vec{v}^2$	**Eq 2-1**

and its momentum $\vec{p}$ is

$\vec{p} = m\vec{v}$	**Eq 2-2**

Neutrons can also be considered as plane waves and according to the *de Broglie relations* plane waves can be described by a wave vector $\vec{k}$ and a wavelength λ

$\vec{k} = \frac{\vec{p}}{\hbar}$	**Eq 2-3**

$\lambda = \frac{2\pi}{\left\|\vec{k}\right\|} = \frac{h}{\vec{p}}$	**Eq 2-4**

Thermal neutrons are produced by fission in a nuclear reactor and thermalized with a moderator at a temperature T. Due to the Maxwell law their average thermal energy amounts to

$E = \frac{3}{2} k_B T$	**Eq 2-5**

where k_B is the *Boltzmann constant*. Cold neutrons are obtained by equilibration at very low temperatures in a cold source. The energies and wavelengths of cold neutrons are roughly in the range of

$0.8meV \leq E \leq 5meV$	**Eq 2-6**
$10Å \geq \lambda \geq 4Å$	**Eq 2-7**

2.2 Kinematics of neutron scattering

Neutron scattering events are described by means of energy and momentum transfer. The kinematics of a neutron scattering event is shown in ***Fig 2-1***.

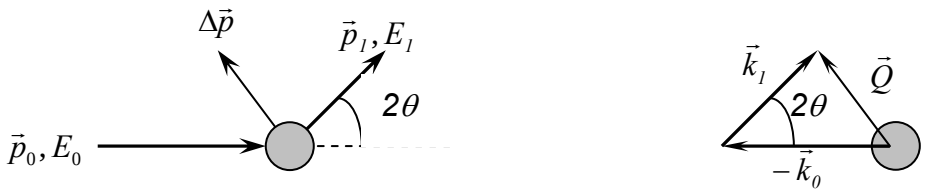

Fig 2-1 *Neutron scattering kinematics in real space (left) and in reciprocal space (right).*

A neutron with incident momentum $\vec{p}_0$ and incident wave-vector $\vec{k}_0$ has an incident energy

$$E_0 = \frac{p_0^2}{2m} = \frac{\hbar^2 k_0^2}{2m}$$	**Eq 2-8**

After interactions with the sample the neutron scatters to the direction 2θ, with a momentum $\vec{p}_1$, a wave-vector $\vec{k}_1$ and energy E_1. As with any particle scattering technique, the energy and the momentum conservation are the two basic principles of neutron scattering. The energy conservation allows to define the energy transfer of the incident and scattered neutrons

$$\hbar\omega = E_1 - E_o = \frac{\hbar^2}{2m}\left(\vec{k}_1^{\,2} - \vec{k}_0^{\,2}\right)$$	**Eq 2-9**

Eventually, the momentum conservation makes it possible to define the scattering vector $\vec{Q}$

$$\hbar\vec{Q} = \vec{p}_1 - \vec{p}_0 = \hbar\vec{k}_1 - \hbar\vec{k}_o$$	**Eq 2-10**

$\vec{Q}$ is often also called as momentum transfer. The magnitude of $\vec{Q}$ is related to the incident and scattered neutron energies and to the scattering angle 2θ as follows

$$Q^2 = \frac{2m}{\hbar^2}\left(E_0 + E_1 - 2\sqrt{E_0 E_1}\cos 2\theta\right)$$	**Eq 2-11**

Both the sign and the magnitude of the energy transfer are used to classify the neutron scattering event, as shown in ***Fig 2-2*** [20].

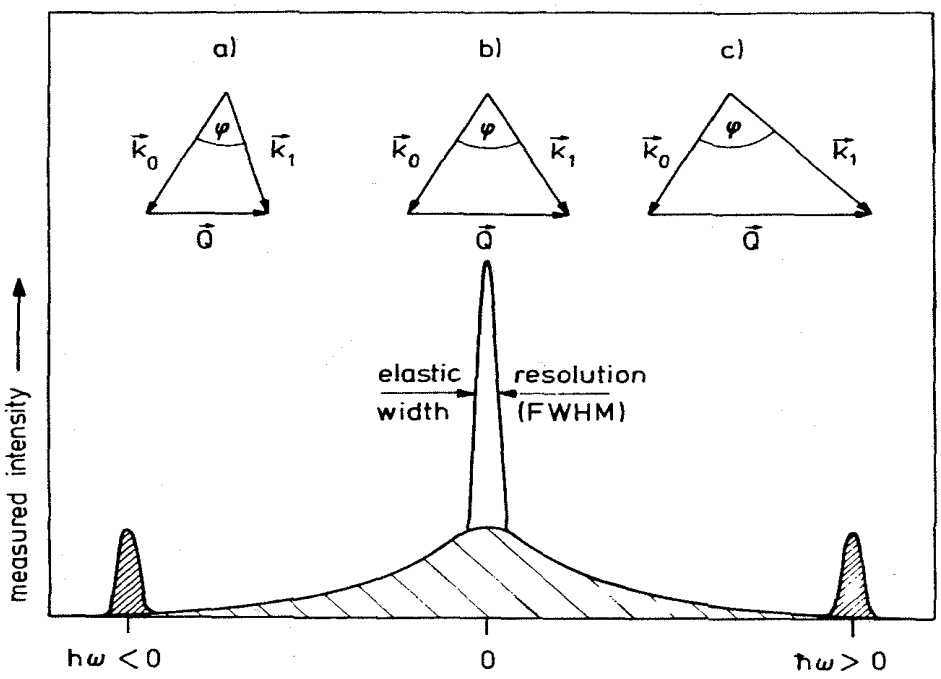

Fig 2-2 *A neutron scattering spectrum as a function of the energy transfer. The elastic peak is shown with its experimental energy resolution width. The momentum conservation triangles are shown for processes of a) neutron energy loss, b) elastic scattering and c) neutron energy gain.*

Neutron scattering is considered elastic, when $\Delta\hbar\omega=E_1-E_0=0$, i.e. the neutrons do not change their energy in the scattering process. If neutrons either gain (i.e. $\Delta\hbar\omega>0$), or loose energy (i.e. $\Delta\hbar\omega<0$) in the scattering process, the scattering is called inelastic. The Doppler-like broadening of otherwise elastically scattered neutrons (for instance, due to the reorientational or translational diffusive motions of particles in the sample material) is called quasielastic neutron scattering (QENS).

2.3 Dynamics of neutron scattering

When an incident neutron encounters the sample it will

a) pass through the sample without changing its physical features, or
b) be absorbed by the nucleus, or
c) be scattered by a nucleus.

To develop a model of the interaction between incident neutrons and nuclei of the sample, it is necessary to derive the proper formalism from the quantum mechanical scattering theory. While the following chapter will present an outline of this procedure, a more detailed description can be found in literature, e.g. [21] and [22].

2.3.1 Fermi pseudopotential

The nucleus-nucleus interaction is known to be of the order 10^{-14}-10^{-15}m which is significantly smaller than the wavelength of the cold neutrons*. Waves of any kind scattered by an object considerably smaller than the wavelength of the scattered waves are spherically symmetric i.e. the scattering is isotropic. Therefore the scattering event can be characterized by a single parameter called scattering length, b. The scattering length of each atom-type is different, as well as that of each isotope. Furthermore, the relative spin orientation of the nuclei has an effect on the scattering length. The scattering lengths are experimentally determined values, given e.g. in reference [23] and [24]. The interaction between a neutron located at $\vec{r}$ and a nucleus with the scattering length b_j at the position $\vec{R}_j$ can be modeled with the Fermi pseudopotential. For a system with numerous nuclei, the Fermi pseudopotential is given as a sum of individual neutron-nuclei interactions

$$V(\vec{r}) = \left(\frac{2\pi\hbar^2}{m_n} \right) \sum_j b_j \delta(\vec{r} - \vec{R}_j) \qquad \text{Eq 2-12}$$

where the sum is built over all the nuclei present in the sample. The Fermi pseudopotential is an appropriate approximation for the potential that is both short ranged and gives the right symmetry for the scattered waves.

* of the order 10^{-10}m

2.3.2 Neutron scattering cross-section

The quantity measured in a neutron scattering experiment is the double differential cross-section

$\frac{\partial^2 \sigma}{\partial \Omega \partial E_1}$	**Eq 2-13**

that gives the proportion of neutrons with an incident energy E_0 scattered into a solid angle element $d\Omega$ with an energy between E_1 and E_1+dE_1.

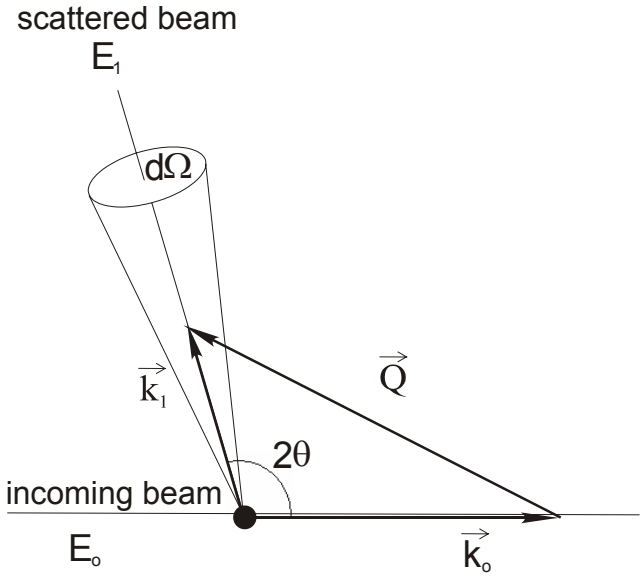

Fig 2-3 *Scattering geometry from a single core*

The geometry of the scattering experiment is shown in ***Fig 2-3 .*** An incident neutron with a wave vector $\vec{k}_0$ is scattered into a state with wave vector $\vec{k}_1$. Before and after the interaction with the neutron, the sample can be described by the quantum states λ_0 and λ_1, respectively. The probability that the combined state of the neutron and the sample makes the transition from the initial state $|\vec{k}_0 \lambda_0\rangle$, to the final state $|\vec{k}_1 \lambda_1\rangle$ is given by Fermi's Golden Rule

$\sum_{\substack{\vec{k}_1 \\ in\ d\Omega}} W_{\vec{k}_0,\lambda_0 \to \vec{k}_1,\lambda_1} = \frac{2\pi}{\hbar} \rho_{\vec{k}_1} \left\| \langle \vec{k}_1 \lambda_1 \| V \| \vec{k}_0 \lambda_0 \rangle \right\|^2$	**Eq 2-14**

where $\rho_{\vec{k}_1}$ is the density of the final states of the neutrons described by $\vec{k}_1$ in $d\Omega$ and V is the interaction potential between the nuclei in the sample and the neutron. Using the Born approximation for the cross-section, the double differential cross section (***Eq 2-13***) is given

$$\frac{\partial^2\sigma}{\partial\Omega\partial E_1} = \frac{\vec{k}_1}{\vec{k}_0}\sum_{\lambda_0\lambda_1} p_{\lambda_0}\left|\left\langle \vec{k}_1\lambda_1\middle|V\middle|\vec{k}_0\lambda_0\right\rangle\right|^2 \delta(\hbar\omega + E_{\lambda_0} - E_{\lambda_1}) \qquad \textbf{Eq 2-15}$$

where the δ-function is included to ensure the energy conservation with the neutron energy transfer $\hbar\omega$, the initial sample energy E_{λ_0} and the final sample energy E_{λ_1}. p_{λ_0} is the probability that the initial state of the sample is λ_0. This probability is given by Boltzmann distribution

$$p_{\lambda_0} = \frac{1}{Z}e^{-E_{\lambda_0}\beta},\ \ with\ \ \beta = \frac{1}{k_B T},\ \ and\ \ Z = \sum_{\lambda_0} e^{-E_{\lambda_0}\beta} \qquad \textbf{Eq 2-16}$$

k_B is the Boltzmann constant, Z the partition function of the sample and T the sample temperature.

After a further manipulation and including the Fermi pseudopotential, the double differential scattering cross-section can be written as

$$\frac{\partial^2\sigma}{\partial\Omega\partial E_1} = \frac{1}{2\pi\hbar}\frac{k_1}{k_0}\sum_{j,i}\overline{b_j b_i}\int\left\langle e^{-i\vec{Q}\vec{R}_i(0)}e^{i\vec{Q}\vec{R}_j(t)}\right\rangle e^{-i\omega t}dt \qquad \textbf{Eq 2-17}$$

Where the average $\overline{b_j b}_i$ of $b_j b_i$ is used to describe the random isotope distributions and random nuclear spin orientations. b_j and b_i are the scattering lengths of the j^{th} and i^{th} nuclei, $\vec{R}_i(0)$ is the position operator of the i^{th} nucleus at time zero, $\vec{R}_j(t)$ is the position operator of the j^{th} nucleus at time t, and $\langle\ \rangle$ denotes a thermal average.

2.3.3 Coherent and incoherent scattering

The average $\overline{b_j b_i}$ for cases $j=i$ and $j\neq i$ is given as follows

$\overline{b_j b_i}^{\,j=i} = \overline{b^2}$ and $\overline{b_j b_i}^{\,j\neq i} = (\bar{b})^2$	**Eq 2-18**

Then the ***Eq 2-17*** can be written as a sum of two components, due to the different mean values for cases $j=i$ and $j\neq i$ as follows

$\frac{\partial^2\sigma}{\partial\Omega\partial E_1} = \frac{1}{2\pi\hbar}\frac{k_1}{k_0}(\bar{b})^2\sum_{j,i}^{j\neq i}\int\left\langle e^{-i\vec{Q}\vec{R}_i(0)}e^{i\vec{Q}\vec{R}_j(t)}\right\rangle e^{-i\omega t}dt$ $+\frac{1}{2\pi\hbar}\frac{k_1}{k_0}\overline{b^2}\sum_{j}^{j=i}\int\left\langle e^{-i\vec{Q}\vec{R}_j(0)}e^{i\vec{Q}\vec{R}_j(t)}\right\rangle e^{-i\omega t}dt$	**Eq 2-19**

While the first part of the sum gives the correlations between the positions of the same nucleus at different times and the correlation between the positions of different nuclei at different times, the second part of the sum only gives the correlation between the positions of the same nuclei at different times. This leads to the introduction of *coherent* and *incoherent* scattering, related to the terms of the sum in ***Eq 2-19*** respectively. Contrary to incoherent scattering, the waves scattered from different atoms of the same crystal can interfere in coherent scattering. This can be explained by the fact that the neutron interacting with the sample does not see a crystal of uniform scattering potential. Instead the scattering varies from one point to the next in the sample. Only the average scattering potential can lead to interference effects, therefore $(\bar{b})^2$ can be used to describe coherent scattering. Since the deviations from the average potential are randomly distributed, and thus they cannot lead to interference effects, therefore incoherent scattering is proportional to the mean-square deviation.

Consequently, the coherent and the incoherent scattering cross section into all directions are defined as follows

$$\sigma_{coh} = 4\pi(\bar{b})^2$$ $$\sigma_{inc} = 4\pi\left(\overline{b^2} - \bar{b}^2\right)$$	**Eq 2-20**

The scattering cross-section has the dimension of surface, and its unit is barn[*].

.

Subsequently, the double differential cross section can be re-written

$$\frac{\partial^2\sigma}{\partial\Omega\partial\omega} = \frac{1}{8\pi^2\hbar}\frac{k_1}{k_0}\sigma_{coh}\sum_{j,i}\int\left\langle e^{-i\vec{Q}\vec{R}_i(0)}e^{i\vec{Q}\vec{R}_j(t)}\right\rangle e^{-i\omega t}dt$$ $$+\frac{1}{8\pi^2\hbar}\frac{k_1}{k_0}\sigma_{inc}\sum_{j}\int\left\langle e^{-i\vec{Q}\vec{R}_j(0)}e^{i\vec{Q}\vec{R}_j(t)}\right\rangle e^{-i\omega t}dt$$ $$=\left(\frac{\partial^2\sigma}{\partial\Omega\partial\omega}\right)_{coh}+\left(\frac{\partial^2\sigma}{\partial\Omega\partial\omega}\right)_{inc}$$	**Eq 2-21**

The coherent scattering contains information about the correlation between the positions of different nuclei and the collective excitations in a sample. The incoherent scattering component can provide information about the individual nuclei and single particle excitations in the sample. The different scattering lengths of different atoms and isotopes, results to different scattering cross sections. Hydrogen has considerably larger incoherent cross section compared to all the other elements (see ***Table 1***). Due to this property hydrogenous materials are suitable to be studied by incoherent neutron scattering techniques. The neutron scattering of ammonium tetraphenylborate is strongly dominated by the incoherent scattering of hydrogen and since the main focus of this work is on single particle properties, incoherent neutron scattering is a suitable tool for investigations.

[*] 1 barn= 10^{-24}cm^2

Element (Symbol)	σ_{coh} (barns)	σ_{inc} (barns)
Hydrogen (H)	1.7599	79.91
Deuterium (D)	5.597	2.04
Carbon (C)	5.554	0.001
Nitrogen (N)	11.01	0.49
Boron (B)	3.54	1.70

Table 1 *Thermal-neutron scattering cross sections of some elements for condensed matter research by Sears [24].*

2.3.4 Scattering functions

The pair-correlation function describes the position of nuclei in space and time, and is given for N nuclei as

$$G(\vec{R},t)=\frac{1}{N}\sum_{i,j}^{N}\left\langle \delta\left\{\vec{R}+\vec{R}_i(0)-\vec{R}_j(t)\right\}\right\rangle \qquad \textbf{Eq 2-22}$$

If $j=i$, the pair correlation function is called self pair-correlation function. The space Fourier transformation of the pair-correlation function $G(\vec{Q},t))$ is called intermediate scattering function

$$I(\vec{Q},t)=\int_{-\infty}^{\infty}G(\vec{R},t)e^{i\vec{Q}\cdot\vec{R}}dR=\frac{1}{N}\sum_{i,j}\left\langle e^{-i\vec{Q}\cdot\vec{R}_i(0)}e^{i\vec{Q}\cdot\vec{R}_j(t)}\right\rangle \qquad \textbf{Eq 2-23}$$

A time Fourier transform of the intermediate scattering functions leads to the scattering function (also often called as a dynamic structure factor), that provides information on the sample states as a function of energy and momentum

$$S(\vec{Q},\omega)=\frac{1}{2\pi\hbar}\int_{-\infty}^{\infty}I(\vec{Q},t)e^{-i\omega t}dt \qquad \textbf{Eq 2-24}$$

Each of the functions $G(\vec{R},t)$, $I(\vec{Q},t)$ and $S(\vec{Q},\omega)$ can describe the sample properties perfectly. However, only $I(\vec{Q},t)$ and $S(\vec{Q},\omega)$ can be experimentally observed. Both of them can be divided into a coherent and an incoherent part as a consequence of the reasons that were presented above.

With respect to the study presented in this work, it is reasonable to consider the incoherent parts only

$$I_{inc}(\vec{Q},t)=\frac{1}{N}\sum_{j=1}^{N}\left\langle e^{-i\vec{Q}\cdot\vec{R}_j(0)}e^{i\vec{Q}\cdot\vec{R}_j(t)}\right\rangle$$	**Eq 2-25**
$$S_{inc}(\vec{Q},\omega)=\frac{1}{2\pi\hbar}\frac{1}{N}\sum_{j=1}^{N}\int_{-\infty}^{\infty}\left\langle e^{-i\vec{Q}\cdot\vec{R}_j(0)}e^{i\vec{Q}\cdot\vec{R}_j(t)}\right\rangle e^{-i\omega t}dt$$	**Eq 2-26**

Consequently the relationship between the incoherent scattering function and the incoherent double differential scattering cross section can be written as

$$\left(\frac{\partial^2\sigma}{\partial\Omega\partial E}\right)_{inc}=\frac{\sigma_{inc}}{4\pi\hbar}\frac{\vec{k}_1}{\vec{k}_o}NS_{inc}(\vec{Q},\omega)$$	**Eq 2-27**

2.3.5 Detailed balance

The probability that a neutron gains an energy ω is different from the probability that a neutron looses an energy ω in the scattering process. The scattering function for neutrons gaining energy is related to the scattering function for neutrons loosing energy with the detailed balance condition, the mathematical form is given by

$$S\ (\vec{Q},\omega)=e^{\frac{\hbar\omega}{k_BT}}S(Q,-\omega)$$	**Eq 2-28**

The comparison with the experimental data requires a correction, in order to observe the symmetric scattering function. Therefore the experimental data must be corrected by a detailed balance factor

$S^{sym}(Q,\omega) = e^{-\frac{\hbar\omega}{2k_BT}} S^{\exp}\bar{Q},\omega)$	**Eq 2-29**

where $S^{sym}(Q,\omega)$ is the symmetric form of the structure factor that is invariant under a change in sign of the ω.

2.3.6 Separation of different motions

The incoherent scattering function includes the position vector of the scattered neutrons $\vec{R}(t)$, which can be separated into two different components, depending on the different types of motion

$\vec{R}(t) = \vec{r}_e\ (t) + \vec{u}(t)$	**Eq 2-30**

$\vec{u}(t)$ is the displacement vector of the nucleus from its equilibrium position inside the molecule due to the internal vibrations (zero-point motion). $\vec{r}_e\ (t)$ describes the instantaneous location of this equilibrium position at a time t, with respect to an externally fixed coordinate system. Thus $\vec{r}_e\ (t)$ can describe the diffusive motions of the entire molecule and it can be separated into two parts

$\vec{r}_e\ (t) = \vec{r}_e^{\,T}(t) + \vec{r}_e^{\,R}(t)$	**Eq 2-31**

where $\vec{r}_e^{\,T}(t)$ is related to translational diffusion of the molecule and $\vec{r}_e^{\,R}(t)$ is related to rotational diffusion of the molecule around its centre of mass. Furthermore a case of a solid material (like the used ATPB samples) is considered. Then the centre of mass of the molecule is restricted to well-defined

positions and thus translational diffusion usually does not occur on a time-scale relevant for experimental observations. Around these well-defined positions anyhow, small fluctuations occur as a result of thermal agitation. Therefore for a solid sample can be written

$\vec{r}_e^{\,T}(t) = \vec{r}_T + \vec{u}_T(t)$	**Eq 2-32**

$\vec{u}_T(t)$ is related to the thermal fluctuations and $\vec{r}_T$ is related to the translational diffusion, which is not time dependent for a solid sample. In liquids translational diffusion of the molecule can occur. In this case the term describing translational diffusion is time dependent. However, this case is not discussed here as the focus of this work is on the properties of solid samples.

When the molecule rotates around its centre of mass, it is very convenient to describe the rotation by instantaneous jumps between several equilibrium orientations. Moreover between the jumps, the molecule assumes an orientation where small-amplitude rotational oscillations (librations) occur, which depend on intermolecular interactions. Therefore

$\vec{r}_e^{\,R}(t) = \vec{r}_R(t) + \vec{u}_R(t)$	**Eq 2-33**

$\vec{r}_R(t)$ is time dependent if several equilibrium orientations exist and time independent if one precise equilibrium orientation occurs. $\vec{u}_R(t)$ is the deviation vector, corresponding to the librations.

For a solid sample $\vec{R}(t)$ can be expressed as

$\vec{R}(t) = \vec{r}_R(t) + \vec{u}_R(t) + \vec{u}_T(t) + \vec{u}(t)$	**Eq 2-34**

The intermediate incoherent scattering function can be written as

$I_{inc}(\vec{Q},t) = \left\langle e^{-i\vec{Q}\left[\vec{r}_R(0)+\vec{u}_R(0)+\vec{u}_T(0)+\vec{u}(0)\right]} e^{i\vec{Q}\left[\vec{r}_R(t)+\vec{u}_R(t)+\vec{u}_T(t)+\vec{u}(t)\right]} \right\rangle$	**Eq 2-35**

The position vector $\vec{R}(t)$ describes three different types of motion, which occur on different timescales. Compared to intramolecular or lattice vibrations, reorientations of molecules are rather slow processes. It is reasonable to separate the intermediate incoherent scattering function according to these three different types of motion.

L*attice contribution*	$I_{inc}^{L}(\vec{Q},t) = \left\langle e^{-i\vec{Q}\left[\vec{u}_R(0)+\vec{u}_T(0)\right]} e^{i\vec{Q}\left[\vec{u}_R(t)+\vec{u}_T(t)\right]} \right\rangle$	**Eq 2-36**
Reorientational term	$I_{inc}^{R}(\vec{Q},t) = \left\langle e^{-i\vec{Q}\left[\vec{r}_R(0)\right]} e^{i\vec{Q}\left[\vec{r}_R(t)\right]} \right\rangle$	**Eq 2-37**
Intramolecular vibrations	$I_{inc}^{V}(\vec{Q},t) = \left\langle e^{-i\vec{Q}[\vec{u}(0)]} e^{i\vec{Q}[\vec{u}(t)]} \right\rangle$	**Eq 2-38**

Subsequently ***Eq 2-35*** rewrites

$I_{inc}(\vec{Q},t) = I_{inc}^{L}(\vec{Q},t) I_{inc}^{R}(\vec{Q},t) I_{inc}^{V}(\vec{Q},t)$	**Eq 2-39**

The Fourier transformation of $I_{inc}(\vec{Q},t)$ leads to the incoherent scattering function for different kinds of motions

$S_{inc}(\vec{Q},\omega) = S_{inc}^{L}(\vec{Q},\omega) \otimes S_{inc}^{R}(\vec{Q},\omega) \otimes S_{inc}^{V}(\vec{Q},\omega)$	**Eq 2-40**

where the symbol $\otimes$ denotes the convolution product.

2.3.7 Elastic, quasielastic and inelastic scattering

Dividing the incoherent intermediate scattering function into time-independent and into time-dependent parts as follows

$I_{inc}(\vec{Q},t) = I_{inc}(\vec{Q},\infty) + I_{inc}(\vec{Q},t)$	**Eq 2-41**

and taking its Fourier transform leads to

$S_{inc}(\vec{Q},\omega) = I_{inc}(\vec{Q},\infty)\delta(\omega) + S_{inc}^{inel}(\vec{Q},\omega)$	**Eq 2-42**

where $I_{inc}(\vec{Q},\infty)\delta(\omega)$ is a purely elastic component and $S_{inc}^{inel}(\vec{Q},\omega)$ includes information about the microscopic dynamics of the sample.

The quasielastic contribution, which will be separated from the inelastic scattering below originates from the diffusive motions and can be described by $S_{inc}^{R}(\vec{Q},\omega)$ for a solid sample. The lattice contribution and the intramolecular vibrations described by $S_{inc}^{L}(\vec{Q},\omega)$ and $S_{inc}^{V}(\vec{Q},\omega)$ respectively, produce the inelastic spectra outside of the quasielastic region. $S_{inc}^{V}(\vec{Q},\omega)$ produces broadened lines at relatively high energy transfer values connected to the vibrational levels of the molecule. $S_{inc}^{L}(\vec{Q},\omega)$ leads to a broad band of scattered intensity in the surrounding area of the quasielastic region and produces a small flat background in the quasielastic region.

Besides the motion of particles around their equilibrium positions due to $S_{inc}^{L}(\vec{Q},\omega)$ and $S_{inc}^{V}(\vec{Q},\omega)$ causes Q–dependent attenuation of the scattering intensity. The form of the attenuation is obtained by describing the oscillation of these particles around their equilibrium positions as quantum mechanical harmonic oscillator given as

$S_{inc}(\vec{Q},\omega) = e^{-2W}\delta(\hbar\omega)$	**Eq 2-43**

where $2W = Q^2\left\langle u^2 \right\rangle$ and the exponential term is known as the Debye-Waller factor. $\left\langle u^2 \right\rangle$ denotes mean-square displacement of a particle from its equilibrium positions.

Because the rotational diffusion, described by $S_{inc}^{R}(\vec{Q},\omega)$, is the basic quantity of interest in this work and the vibrations and librations of the particles are much faster than the diffusive motions, it is reasonable to introduce them as an inelastic background in the quasielastic region. Thus the quasielastic incoherent scattering function can be given as

$S_{inc}^{qe}\vec{Q},\omega) = e^{-\left\langle u^2 \right\rangle Q^2}\left[I_{inc}^{R}(\vec{Q},\infty)\delta(\omega) + S_{inc}^{R}(\vec{Q},\omega) + S_{inc}^{I}(\vec{Q},\omega)\right]$	**Eq 2-44**

where $S_{inc}^{I}(\vec{Q},\omega)$ is the inelastic background in the quasielastic region caused by $S_{inc}^{L}(\vec{Q},\omega)$ and $S_{inc}^{V}(\vec{Q},\omega)$. $S_{inc}^{R}(\vec{Q},\omega)$ represents the quasielastic term and where I_{inc}^{R} is called elastic incoherent structure factor (EISF)

Integrating the incoherent scattering function over the energy transfer at constant $\vec{Q}$ according to ***Eq 2-24*** leads to

$\int_{-\infty}^{\infty} S_{inc}^{R}(\vec{Q},\omega)d\omega = \int_{-\infty}^{\infty} I_{inc}^{R}(\vec{Q},t)\delta(t)dt = I_{inc}^{R}(\vec{Q},0) = 1$	**Eq 2-45**

This means that EISF is the fraction of the total quasielastic intensity contained in the purely elastic peak. If the elastic component and the wider quasielastic component can be separated, the EISF is a measurable quantity, evaluated from the ratio

$EISF(\vec{Q}) = \frac{I^{el}(\vec{Q})}{I^{el}(\vec{Q}) + I^{qe}(\vec{Q})}$	**Eq 2-46**

where $I^{el}(\vec{Q})$ and $I^{qe}(\vec{Q})$ are the integrated intensities corresponding to the elastic and quasielastic part of the spectra, respectively.

In the experimental data the elastic scattering appears, instead of an infinitely sharp line, as a peak-shaped curve with an energy width corresponding to the instrumental resolution. This width defines the magnitude of the time-scale over which the diffusive motions are observable. The typical time-scale for a time-of-flight instrument is in the range of 10^{-10}-10^{-12}s. If the diffusive motions are significantly slower than the instrumental resolution, they cannot be distinguished from the elastic peak. On the other hand, if the diffusive motions are much faster than the instrumental resolution, the quasielastic component will be a very broad and flat term. Therefore it is important to note that the characteristic times of the diffusive motions studied by quasielastic incoherent neutron scattering have to be of the same order as the instrumental resolution. While the width of the quasielastic component can reveal information on the characteristic times of the diffusive motions, the Q-dependent EISF provides information about the nature of the diffusive motion itself.

3 EXPERIMENTAL

3.1 Sample preparation

3.1.1 Ammonium tetraphenylborate, $NH_4(C_6H_5)_4B$ (hereafter ATPB)

Following the instruction of Westerhaus et al. [25] the ATPB-powder was prepared from sodiumtetraphenylborate $Na(C_6H_5)_4B$ and ammoniumchloride NH_4Cl, both commercially available. Equimolar amounts of $Na(C_6H_5)_4B$ and NH_4Cl were dissolved in water at room temperature. The white salt of ATPB precipitated immediately and it was washed with acetone for recrystallization. To verify its purity and crystallinity, the sample was examined by X-ray diffraction (HUBER Imaging Plate Guinier Camera G670) at room temperature. A structural model was refined against the observed X-ray data using the Fullprof suite (see ***Fig 3-1***). As input for the simulations the crystallographic data published by Steiner et al [6] was used. As shown in ***Table 2***, the cell parameters obtained from the X-ray measurement are comparable to [6].

Cell parameters of ATPB	a (Å)	b (Å)	c (Å)	α	β	γ
ATPB sample used in this work	11.25	11.25	8.08	90°	90°	90°
Steiner et al. [6]	11.2255	11.2255	8.0745	90°	90°	90°

Table 2 *Unit cell parameters of the ATPB.*

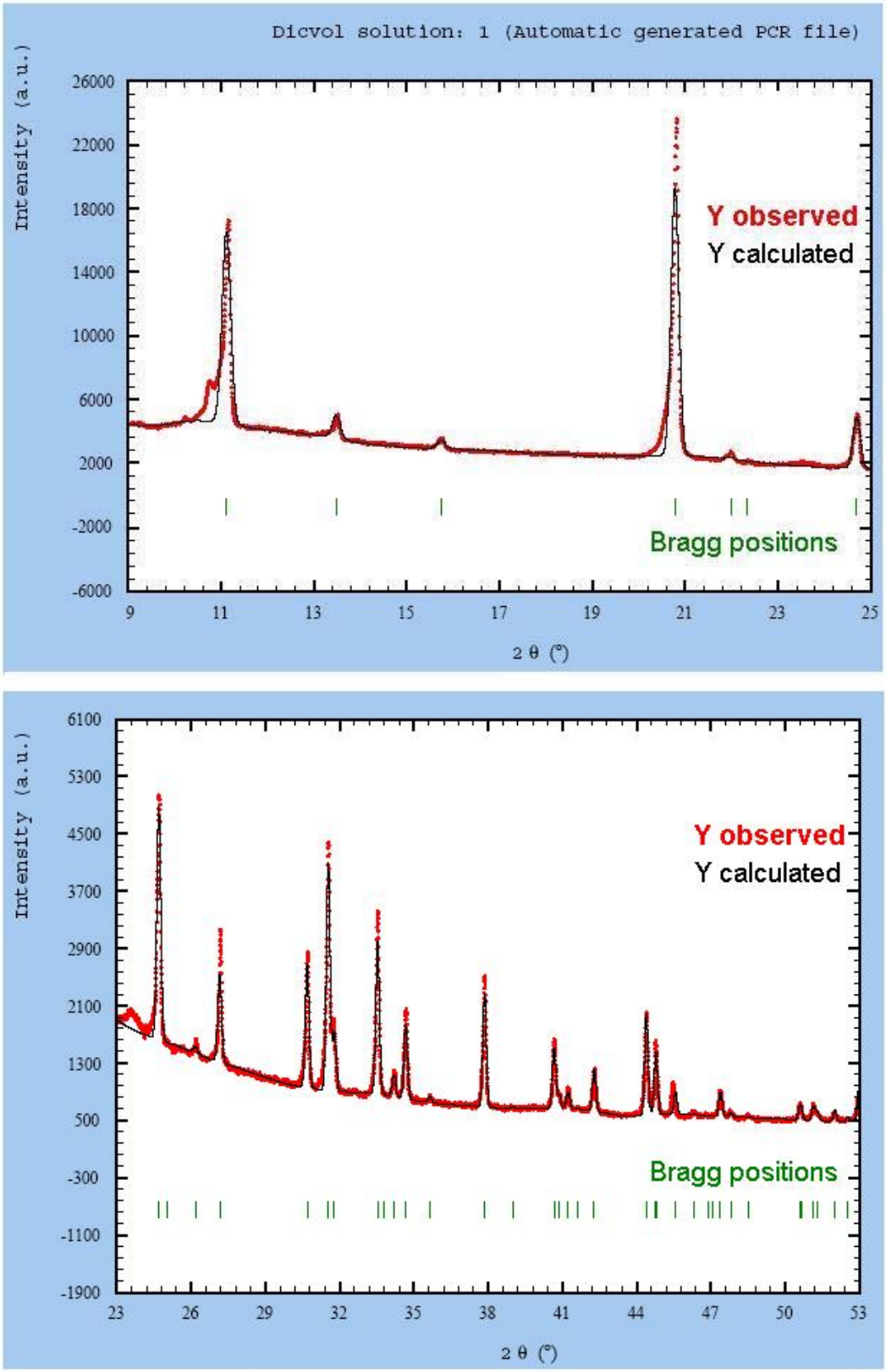

Fig 3-1 *X-ray diffraction pattern of the ATPB sample, here shown up to a diffraction angle of 53°. In the upper figure the region 5°<2θ<25° is shown. In the lower figure the region 23°<2θ<53° is shown rescaled. The measurement is shown red, while the black line represents the simulated X-ray pattern for the ATPB. For the simulations we used the crystallographic data published by Steiner et al [6]. The Bragg peak positions, used to define the structure are indicated with green marks.*

3.1.2 Ammonium-deuterated tetraphenylborate, $ND_4(C_6H_5)_4B$ (hereafter ATPB-d)

The use of selective deuteration is a very powerful approach in inelastic neutron scattering (INS). In order to get more insight on the motions of phenyl rings, a sample with deuterated ammonium ions ND_4 $(C_6H_5)_4B$ (hereafter called ATPB-d) was prepared. Due to the drastically lower incoherent cross section of the D atoms, the motions of the ND_4 groups are "selectively" excluded. The ATPB-d was prepared by using commercially available products: ND_4Cl and $Na(C_6H_5)_4B$. Equimolar amounts of these powders were separately dissolved in D_2O at room temperature in a closed argon atmosphere. After mixing the solutions a white salt of ATPB-d precipitates immediately. For recrystallization, the ATPB-d salt was subsequently washed with deuterated acetone $(CD_3)_2CO$. The ATPB-d was examined by X-ray diffraction (HUBER Imaging Plate Guinier Camera G670). The X-ray pattern (see ***Fig 3-2***) is similar to that of the ATPB and thus confirms the crystallinity of the ATPB-d.

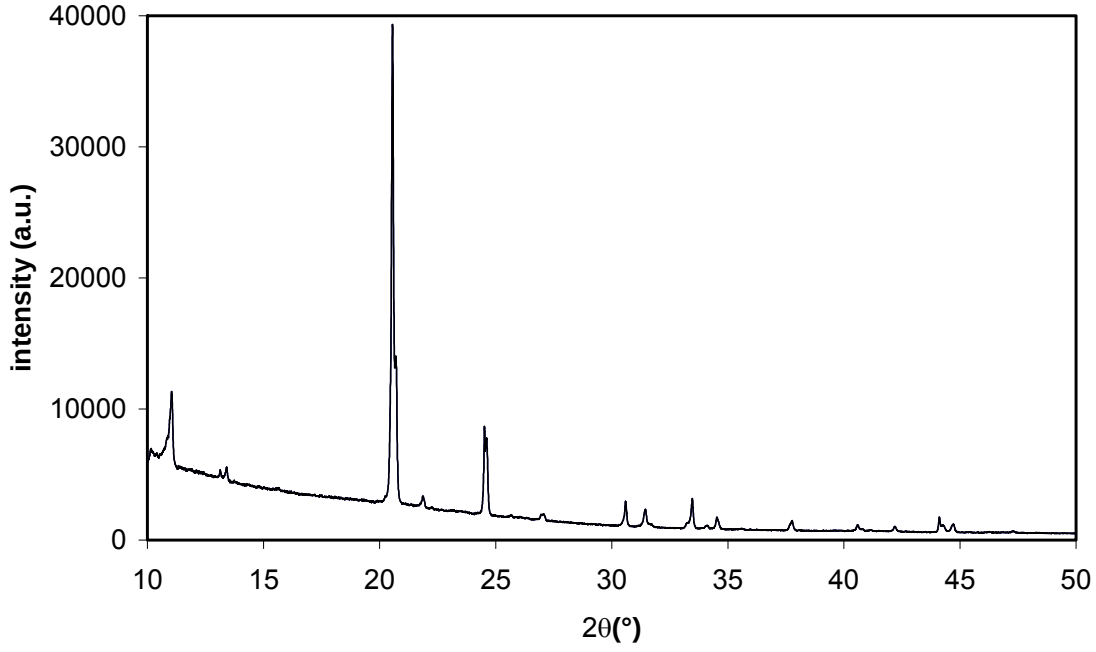

Fig 3-2 *X-ray diffraction pattern of the ATPB-d sample, here shown diffraction angle up to 50°.*

Some difficulties at the sample preparation were caused by the instability of the ND_4Cl. This compound is highly hygroscopic, and rather quick exchange of deuterium into hydrogen can occur, if ND_4Cl is exposed to air. To avoid this exchange all the preparations were carried out in a glove box filled with argon. The commercial product of ND_4Cl was only available with a nominal deuteration of 98%. However, the IR-measurement indicates that the deuteration percentage was even lower, as shown in ***Fig 3-3***.

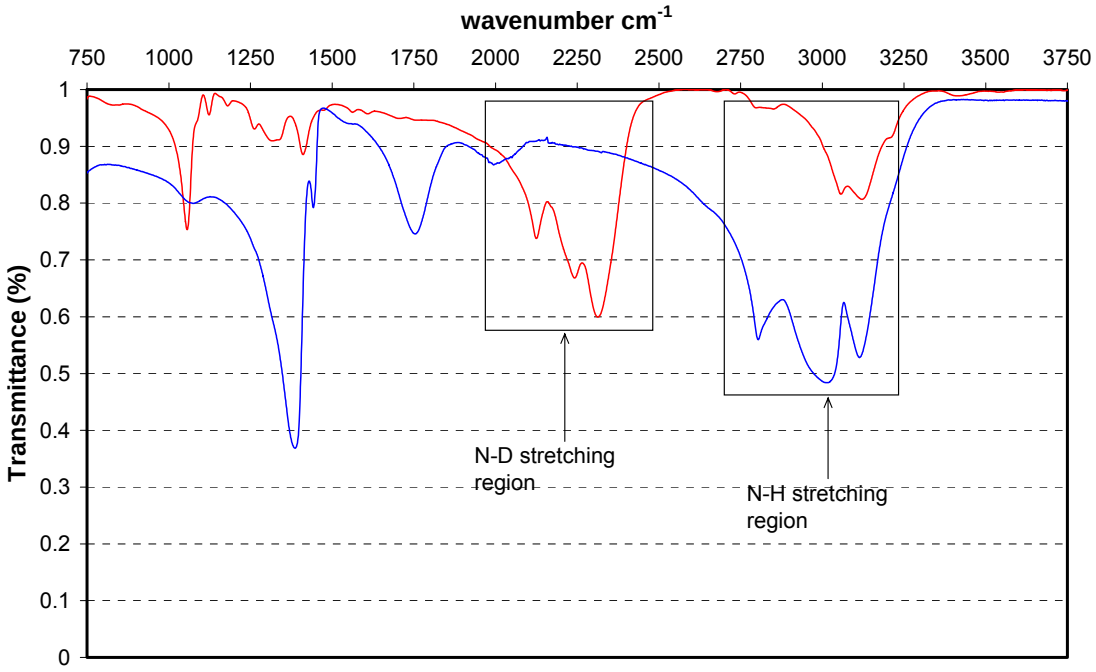

Fig 3-3 *Infrared spectrum of ND_4Cl (the red line) and NH_4Cl (the blue line), measured with Bruker-spectrometer at room temperature. The fundamental frequencies of NH_4Cl have been assigned in literature [26]. The fact that we observe by IR both $\gamma_{N\text{-}D}$ and $\gamma_{N\text{-}H}$ indicates that the selective deuteration was not 100%.*

Furthermore, as both D_2O and $(CD_3)_2CO$ also contain a microscopic amount (less that 0.1%) of non-deuterated molecules, it is possible that un-deuteration for the ammonium ions can be caused. Consequently, the chemical formula for the ATPB-d should be written as follows $N(D_x H_y)_4 (C_6H_5)_4 B$, with x+y=1. The percentage of the ammonium-deuteration in the ATPB-d was carefully determined by the neutron scattering time-of-flight data, measured at NEAT. The method as well as the percentage of deuteration will be described in ***Section 4.1***.

3.2 Quasielastic incoherent neutron scattering experiments

The quasielastic incoherent neutron scattering (QENS) experiments were performed at NEAT time-of-flight spectrometer. The spectrometer faces the cold source of the 10MW research reactor at the Berlin Neutron Scattering Centre (BENSC) at the Hahn-Meitner-Institut (HMI) in Berlin.

3.2.1 Time-of-flight instrument NEAT

NEAT is a direct geometry time-of-flight multichopper spectrometer [27, 28, 29]. A schematic of the instrument is shown in ***Fig 3-4.***

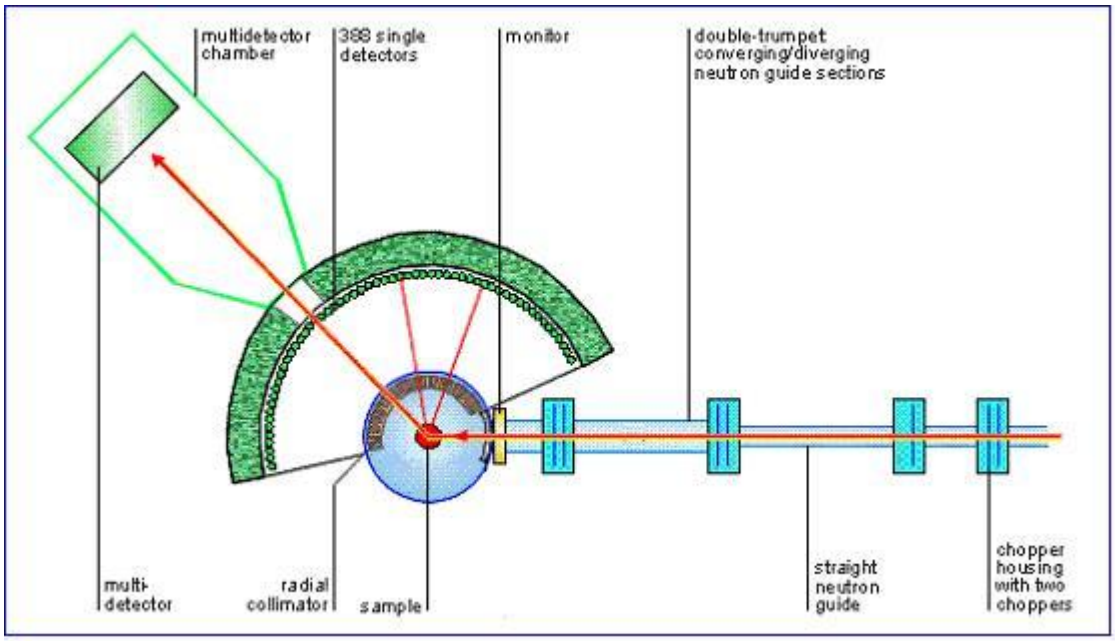

Fig 3-4 *A schematic of the spectrometer NEAT*

The operating principle of NEAT is following: Periodic pulses of 'monochromatic' neutrons are produced from incident 'white' neutron beam by seven phased disc choppers, each of which has neutron transparent apertures of variable widths. A pair of counter rotating choppers is used to create neutron pulses by chopping the incident beam, and another pair to select a narrow wavelength band from these pulses. The remaining three choppers are used to optimize the

neutron beam. The time and energy widths of the neutron pulses are variable in large ranges by varying the speed of the choppers, the chopper windows and the neutron wavelength (details are given in ***Appendix*** A). Behind the last chopper, in front of the sample, there is located a monitor which counts a tiny proportion of the incident neutrons. This monitor reveals information on the flux of the incident neutron beam and thus on the number of neutrons that arriving at the sample.

Monochromatic neutron pulses arrive at the sample at exactly known times. The scattered neutrons are detected between 13.35° and 136.65° by 388 single detectors located 2.5m from the sample. The detected neutrons are histogrammed according to their time-of-flight. Then the final energy of the detected neutrons can be defined as

$$E_1 = \frac{1}{2} m_n \left(\frac{2.5m}{t_{of-flight}} \right)^2 \qquad \textbf{Eq 3-1}$$

The final neutron energies together with the known incident neutron energy and the scattering angle allow us to determine the partial differential scattering cross-section.

To illustrate the operation of such a time-of-flight spectrometer, a neutron flight-path diagram as a function of neutron time-of-flight is shown in ***Fig 3-5*** [30] for the IN5 spectrometer (located at the ILL, Grenoble France). This example demonstrates the filter function of various discs of the chopper cascade in an experiment in which the rotational motion of OH^- ions in cubic Na OH [31] was studied at an incident neutron wavelength of 4Å. In this diagram the vertical axis represents the flight-path between the different elements of the chopper cascade. The first chopper (CH1) is located at the flight path origin, and it defines the initial time-distribution of the neutron pulse. CH_P is the pre-monochromator, which stops the larger part of the “white” beam by reducing the pulse frequency, in order to avoid frame-overlap at the detectors. CH2 selects the ‘monochromatic’ wavelength band for the experiment. Furthermore the wavelength distribution after the scattering event is shown, where S represents

the sample position. Neutrons which gained energy during the scattering process arrive faster to the detectors (D), while neutrons which lost energy during the scattering process arrive later at the detectors. The elastic scattering produces a sharp peak in the spectra at the position where the neutrons arrive with the incident wavelength.

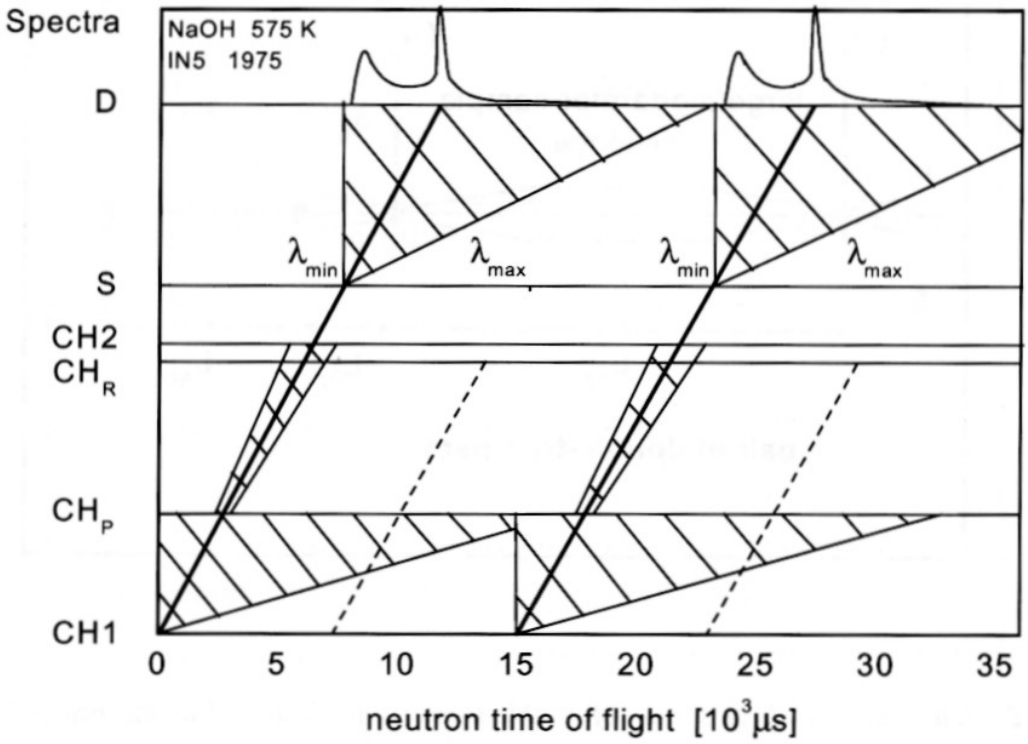

Fig 3-5 *Neutron flight-path diagram for a configuration of a time-of-flight multichopper spectrometer (IN5)* [30].

3.2.2 Experimental details

For a neutron scattering experiment a suitable amount of sample has a transmission probability on the range of 80% to 95%. A higher transmission might lead to problems with the statistical accuracy, while a lower transmission might cause problems with the multiple scattering effect.

The transmission probability is given as

$$P_{tr} = \exp\left[-\frac{(\sigma_{sc} + \sigma_{abs}) \cdot N_A \cdot m \cdot d}{V \cdot M}\right] \qquad \textbf{Eq 3-2}$$

where σ_{sc} and σ_{abs} are the cross-sections of scattering and absorption, respectively. N_A is the Avogadro's number, m the mass of the sample, M the molecular mass of the sample, $V = d\pi r^2$ volume of the sample container, d the thickness of the sample container and r the radius of the sample container. Now a suitable quantity of the sample can be defined as

$$m = -\frac{\ln(P_{tr}) \cdot \pi \cdot r^2 \cdot M}{(\sigma_{sc} + \sigma_{abs}) \cdot N_A} \qquad \textbf{Eq 3-3}$$

The mass of ATPB and ATPB-d samples varied from 0.41g to 0.6g resulting in a transmission probability of 0.9 to 0.85. The samples were placed into an aluminium container with a thickness of 0.4mm. The sample was examined in reflection geometry, i.e. the angle α between the sample plane and the incident neutron beam was kept equal to 45°.

During the time-of-flight experiments the number of neutrons are detected at various scattering angles and separated into channels depending on their time-of-flight. A number of steps must be performed to extract the incoherent scattering function from the so-called raw time-of-flight data. Then the time-of-flight data can be analysed in order to get information about the diffusive motions in the sample material. Therefore, the raw NEAT data were corrected for detector efficiency and sample-geometry dependent attenuation. Additionally the background was subtracted using the data from a measurement of the empty sample container, the data were normalized to the elastic scattering of vanadium, transformed to the energy scale and interpolated to constant Q values. Additionally several detectors can be grouped together to obtain better statistics. These proceedings were carried out by the FITMO4 software [32], which was developed to analyse the time-of-flight data measured at NEAT. More details of the data processing are given in ***Appendix*** B. The QENS spectra

for ATPB were recorded at eleven different temperatures between 20K and 350K, at four different energy resolutions ΔE=32μeV, ΔE=56μeV, ΔE=98μeV and ΔE=182μeV. For ATPB-d the QENS spectra were recorded at 300K, at an energy resolution ΔE=32μeV. Data acquisition times were 24h, 10h and 6h for energy resolutions 32μeV and 56μeV, 98μeV and 182μeV, respectively.

Some aspects of the instrumental resolution have already been discussed in ***sections 2.3.7*** and ***3.2.1***. In addition, it should be considered how the instrumental resolution appears in the measured data, in order to interpret the experimental data correctly. Due to a limited the instrumental resolution, the incident neutron beam is not purely monochromatic, but broadened depending on the energy distribution of the incident neutrons. Consequently in the experimental data, any function that is explained as a δ-function of energy transfer in theory, appears as a broadened line, the shape and the width of which depends on the resolution function $R(Q, \omega)$. Therefore the measured value of $S(Q, \omega)$ is given as

$$S(Q,\omega) = S'(Q,\omega) \otimes R(Q,\omega) = \int_{-\infty}^{\infty} S'(Q,\omega') R(Q,(\omega-\omega')d\omega'$$	**Eq 3-4**

where $S'(Q,\omega)$ is the theoretical scattering function.

The width and the shape of the instrumental resolution have to be defined in a measurement and normally the elastic scattering of vanadium gives a good approximation. The resolution function of the spectrometer NEAT has a Gaussian shape at the energy resolutions used. It should also be noted that the width of the energy resolution is not constant as a function of the energy transfer. This is especially important for the inelastic neutron scattering data treatment. An expression for the width of a resolution function as a function of the energy transfer for time-of-flight multichopper spectrometers has been developed [33].

3.2.3 Experimental data

An overview of the corrected experimental data is given in ***Fig 3-6*** and ***Fig 3-7***. In ***Fig 3-6*** the spectra of ATPB are shown at an energy resolution of 98μeV at room temperature. The data were sorted into nine groups, in order to obtain better statistics. Three selected groups are shown, each one denoted with its average Q-value. The observed relatively large elastic intensity suggests that about 83% of the hydrogen atoms are attached to the phenyl rings. The corresponding rescaled quasielastic component is shown in the insert. Note, that a quasielastic component indicates that the proton dynamics in the sample occur on a time scale accessible by the instrument (10^{-9}...10^{-13}s). As expected, the elastic intensity decreases as the intensity of the quasielastic component increases with higher Q-values. With decreasing temperatures, the intensity of the quasielastic component is reduced, but it is still obvious even at 20K. In ***Fig 3-7*** the temperature dependence of the quasielastic component at the energy resolution of 56μeV is shown. The data were sorted into two groups to obtain better statistics, the average Q-value in the shown case amounts to 2$Å^{-1}$.

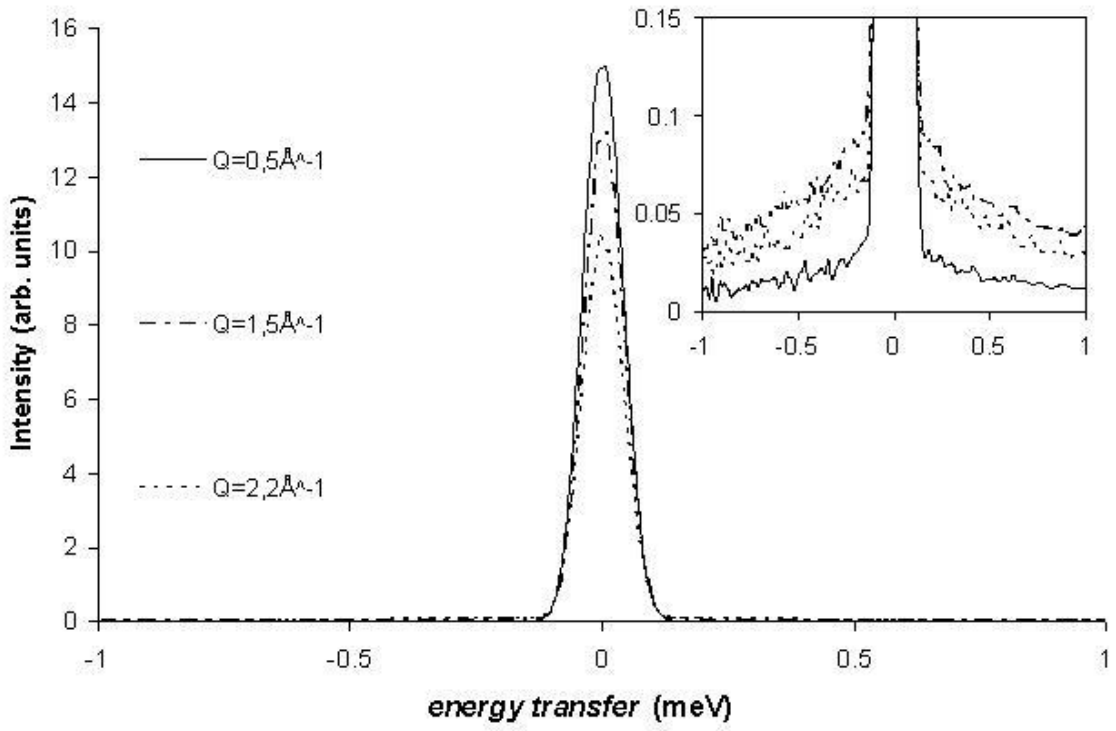

Fig 3-6 *Measured ATPB spectra at three different Q-values with ΔE=98μeV and T=300K. The insert shows the rescaled spectra revealing the quasielastic component.*

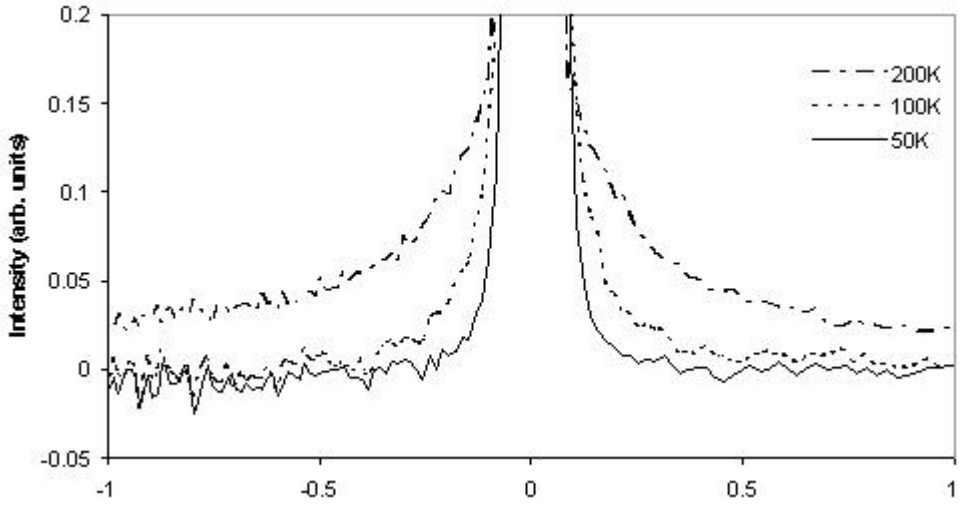

Fig 3-7 *The measured ATPB spectra at three different temperatures at ΔE=98μeV and Q=2Å^{-1}. The spectra were rescaled to show the quasielastic component.*

4 EXPERIMENTAL RESULTS

4.1 Ammonium-deuteration percentage of ATPB-d

To determine the fraction of deuterated ammonium ions, x, in the $N(D_xH_y)_4(C_6H_5)_4B$, the NEAT measurements at identical experimental conditions (i.e. same configuration, same temperature, same sample orientation, same exposure time) of both samples: ATPB and ATPB-d were compared. ***Fig 4-1*** shows the raw time-of-flight spectra summed over all spectra (i.e. all scattering angles ranging from 13° to 137° were grouped together).

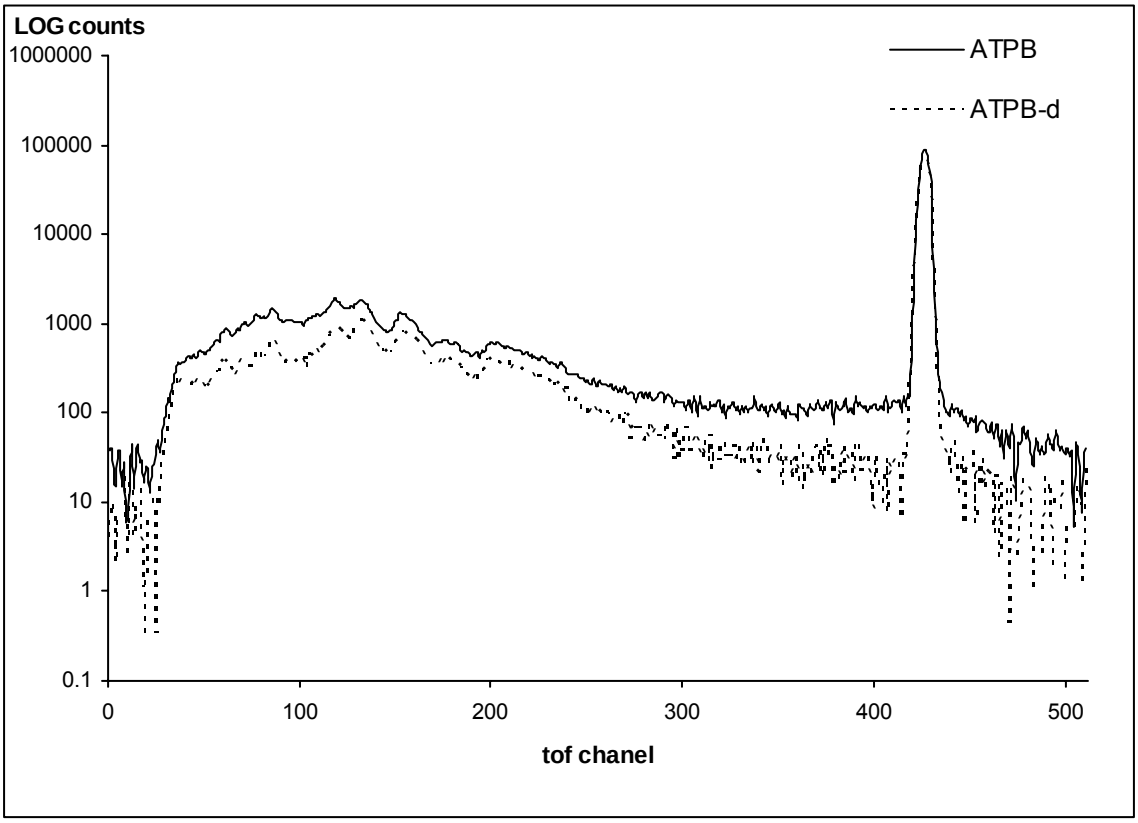

Fig 4-1 *Time-of-flight spectra of ATPB-d and ATPB summed over all spectra, measured at NEAT, at T=300K a wavelength of 8Å, an energy resolution of 30μeV, and an exposure time of 43200s.*

The spectra were not corrected, only the background was subtracted using a spectrum obtained by measuring the empty sample container. Finally, the spectra of the ATPB and the ATPB-d were integrated over all the time-of-flight channels. The integrated scattering intensities amounted to $I_{sc}^{ATPB} = 699647$ and $I_{sc}^{ATPB-d} = 489770$ for the ATPB and the ATPB-d, respectively. The ratio of the integrated scattering intensities results in

$I_{sc}^{ATPB-d} / I_{sc}^{ATPB} = 0.70$	**Eq 4-1**

An integrated scattering intensity I_{sc} corresponds to scattering into a solid angle $\Omega_{NEAT}/4\pi$ which is covered by the detectors of the spectrometer NEAT and is proportional to the scattering probability into any defined solid angle $\Omega/4\pi$.

$I_{sc} \propto P_{sc}$	**Eq 4-2**

Subsequently the ratio of the integrated scattering intensities equals to the ratio of the scattering probabilities

$\frac{I_{sc}^{ATPB-d}}{I_{sc}^{ATPB}} = \frac{P_{sc}^{ATPB-d}}{P_{sc}^{ATPB}}$	**Eq 4-3**

The scattering probability over 4π at well-known experimental conditions can be calculated, if the exact molecular formula of the sample and the number of molecules in the sample are known. The scattering probability of the ATPB sample can be calculated and then P_{sc}^{ATPB-d} can be solved from the ***Eq 4-3***.

The scattering probability can be calculated as follows

$P_{sc} = 1 - (P_{tr} + P_{abs})$	**Eq 4-4**

where the probability of transmission P_{tr} and the probability of absorption P_{abs} are given by

$$P_{tr} = \exp\left[-\frac{(\sigma_{sc}+\sigma_{abs})\cdot N\cdot d}{V}\right]$$	**Eq 4-5**
$$P_{abs} = 1-\exp\left[-\frac{\sigma_{abs}\cdot N\cdot d}{V}\right]$$	**Eq 4-6**

σ_{sc} and σ_{abs} are the cross sections for scattering and absorption. N, V and d are the number of particles, the volume and the thickness of the sample, respectively. The mass of the samples are known to be m^{ATPB}=0.6g and $m^{ATPB\text{-}d}$=0.41g, the thickness of the cylindrical sample container is constant, d=0.4mm and the transmission and absorption probabilities can be written as follows

$$P_{tr} = \exp\left[-\frac{(\sigma_{sc}+\sigma_{abs})\cdot N_A\cdot m}{\pi\cdot r^2\cdot M}\right]$$	**Eq 4-7**
$$P_{abs} = 1-\exp\left[-\frac{\sigma_{abs}\cdot N_A\cdot m}{\pi\cdot r^2\cdot M}\right]$$	**Eq 4-8**

where N_A is the Avogadro's number ($6.022\cdot10^{23}$mol^{-1}), r the radius of the sample container (2.5cm) and M the molecular mass of the sample (M^{ATPB}=337.25g/mol and $M^{ATPB\text{-}d}$=340.38g/mol).

The neutron scattering cross section values are dependent on the used wavelength. The cross section values vary slightly when the used wavelength satisfies the Bragg condition, but reduces dramatically when the Bragg cut-off is reached. Anyhow, with the used relative large wavelength of 8Å the Bragg condition is still satisfied for the ATPB crystal and thus a good approximation of the scattering probabilities can be obtained using the tabulated cross section values. For the absorption cross section values, a correction for 8Å has been made. The values of the scattering and absorption cross-sections as well as the atomic mass of the elements in the ATPB and the ATPB-d and the detailed formulas used to obtain the scattering probabilities are given in ***Appendix C***.

The scattering probability of ATPB [NH_4 $(C_6H_5)_4B$], with m^{ATPB}=0.6g is 0.091058.

In order to determine x, ***Eq 4-3*** must be corrected with the help of the monitor-rates. The ratio of the scattering probabilities corrected with the monitor-rates is termed ***ratio(x)*** and equals the ratio of the integrated scattering intensities

$$\frac{P_{sc}^{ATPB-d}(x)\cdot MR^{ATPB-d}}{P_{sc}^{ATPB}\cdot MR^{ATPB}} = ratio(x) = \frac{I_{sc}^{ATPB-d}}{I_{sc}^{ATPB}} = 0.70 \qquad \textbf{Eq 4-9}$$

where $MR^{ATPB\text{-}d}$ and MR^{ATPB} are the monitor-rates obtained at the measurements of the ATPB-d and the ATPB. The monitor-rate gives the averaged number of neutrons in the incident beam per second during the measurement, detected at the monitor. By correcting the scattering probabilities for the monitor-rates, the different number of neutrons arriving to the sample during the measurements of ATPB and ATPB-d are taken into account.

Now that we know the values of $MR^{ATPB\text{-}d}=39.72685n/s$ and $MR^{ATPB}=37.01387n/s$, it is possible to calculate the $ratio(x)$ for several x values on in the range of $0 \le x \le 1$. After plotting and interpolation, a solution $x=0.766$ is found (see ***Fig 4-2***).

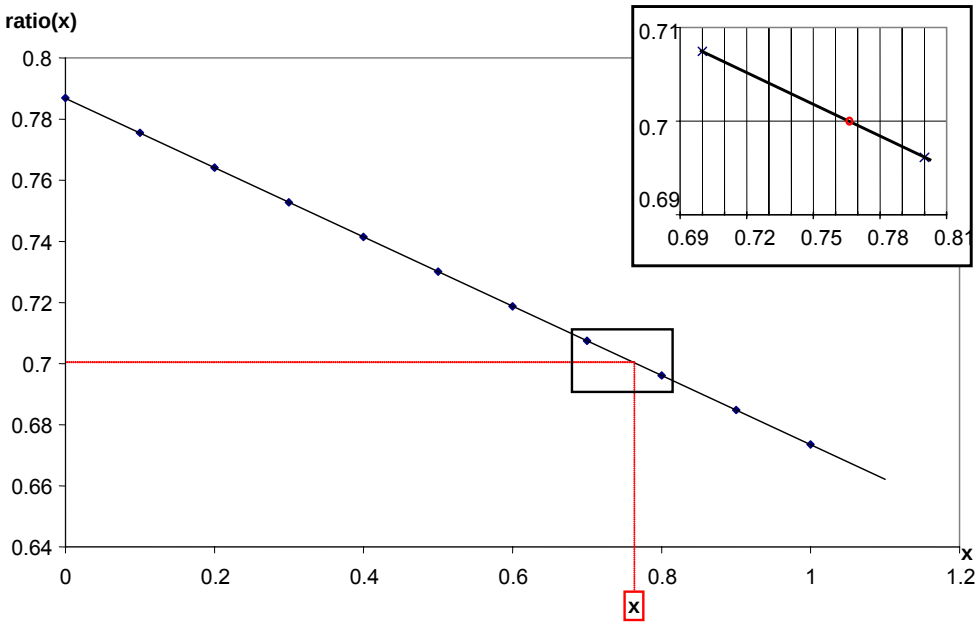

Fig 4-2 *The points show the calculated values of ratio(x). Interpolation of the ratio(x)=0.70 results in an x value that satisfies the* **Eq 4-9**.

Now the exact chemical formula of the ATPB-d sample can be defined as

$N(D_{0.77}H_{0.23})_4(C_6H_5)_4B$	Eq 4-10

This result implies that the selective deuteration was not complete, and thus a contribution from the NH_4 groups, which is proportional to the number of H atoms, is still observable. It can be assumed that the scattering from the ammonium groups is reduced by about 80%, for the ATPB-d sample due to the deuteration ratio and the number of particles in both samples.

4.2 Diffusive motions

In ***section 3.2.3*** the QENS spectra of ATPB at few selected temperatures were shown, and it was pointed out that the quasielastic component is due to the diffusive motions in ATPB. Because the ATPB sample is a solid, it is not expected that translational diffusion would occur on the time scale accessible by the NEAT measurements. Instead, it can be assumed that the rotational diffusion is the source of the observed quasielastic scattering. As observed, the elastic peak is relatively large, compared to the corresponding the quasielastic component. We can argue that this is due to the fact that in ATPB the hydrogen atoms are either attached to the ammonium ions (17%) or to the phenyl rings (83%). Therefore the first step in the data analysis is to consider that the phenyl rings are immobile (on the time scales measured in the NEAT experiments) and that the observed quasielastic component originates only from the motions of the ammonium ions. Later the possibility that the motions of phenyl rings are also observable at the measured time scale will also be considered.

To analyse the QENS data, models for the incoherent scattering functions of isotropic powder samples (rather than single crystals) based on the sample geometry have been developed. Therefore the momentum vectors appearing in the expressions of the cross-sections and the scattering functions are replaced by their moduli. Suitable values for the model parameters can be determined by fitting the theoretical formulas to the measured spectra.

4.2.1 Ammonium reorientations

4.2.1.1 Theoretical models

As already discussed in ***Section 2.3.6*** and ***2.3.7***, rotational diffusion can be described by instantaneous jumps between several equilibrium orientations. Between the jumps, the molecule assumes an orientation, where librations occur. Due to the tetrahedral symmetry of the NH_4^+, several specific models can be considered. Below four models for the whole ammonium ion reorientations and a model for N-H vector libration over the face of the phenyl ring will be described. Finally a model that combines the whole ion reorientations and the libration will be described.

4.2.1.1.1 Continuous isotropic rotational diffusion

There are only very few molecular solids which are close to the limit of free rotation, such are eg. solid hydrogen and methane in some molecular crystals [34]. Anyhow, the previous infrared [59] and Raman [57] studies of ATPB at low temperature show features typical for nearly free rotor.

An approximation of free rotation can be obtained from a model for continuous rotational diffusion. This is assumed when probability to obtain any orientation is the same and the diffusion remains restricted to the surface of a sphere of the radius R.

The scattering law for this motion is given as [35]

$$S_{RD}(Q,\omega) = A_0(Q)\cdot\delta(\omega) + \sum_{\ell=1}^{\infty} A_\ell(Q)\frac{1}{\pi}\frac{\ell(\ell+1)D_r}{\left[\ell(\ell+1)D_r\right]^2+\omega^2} \qquad \text{Eq 4-11}$$

where D_r is rotational diffusion coefficient,

$A_\ell(Q) = (2\ell + 1) j_\ell^2(QR); \quad \ell = 0,1,2...\infty$	**Eq 4-12**

and j_ℓ are the spherical Bessel functions of ℓ order.

In ATPB the ammonium motions can be supposed to be limited to a sphere with a radius of R=0.9Å, which is the N-H distance in the NH_4^+ ion.

4.2.1.1.2 Two-site jump model

Several examples of ammonium ion rotations around a C2-axis have been studied by QENS before e.g. [60] & [36]. In the two-site jump model NH_4^+ rotates around the C2-axis. In this model the tetrahedral ion has two equal equilibrium orientations. The ion makes jumps of 180° around a rotation axis, as shown in ***Fig 4-3***, so that two adjacent H atoms change their places.

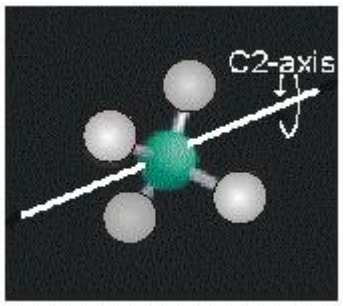

Fig 4-3 *Illustration of NH_4^+ rotation around a C2-axis*

The scattering law for such motion is

$S_2(Q,\omega) = A_{02}(Q) \cdot \delta(\omega) + [1 - A_{02}(Q)] \frac{1}{\pi} \frac{\Delta_2}{\omega^2 + \Delta_2^2}$	**Eq 4-13**

where the half-width at half-maximum (HWHM) Δ_2 of the Lorentzian function, is related to the jump rate of the motion, τ_2^{-1}, by

$\Delta_2 = 2\tau_2^{-1}$	**Eq 4-14**

The Elastic Incoherent Structure Factor (EISF) is

$A_{02}(Q) = \frac{1}{2}[1 + j_0(2Qr_2)]$	**Eq 4-15**

where r_2 is the radius of rotation and j_0 is the spherical Bessel function of zero order

$j_0(x) = \sin(x)/x$	**Eq 4-16**

Knowing the N-H bond length ($d_{N\text{-}H}$) of the NH_4^+ to be 0,9Å [6], the jump distance between the two H atom amounts to

$2r_2 = \frac{2\sqrt{2}}{\sqrt{3}} d_{N-H}$	**Eq 4-17**

4.2.1.1.3 Three-site jump model

Another possible model suggests rotations around a C3-axis, so that one of the hydrogen atoms is immobile (with respect to the timescale provided by the time-of-flight spectrometer NEAT). Examples of ammonium reorientations around a C3-axis can be found in literature, e.g. [37].

The three mobile hydrogen atoms rotate by 120° steps around the axis and change their positions as shown in ***Fig 4-4.***

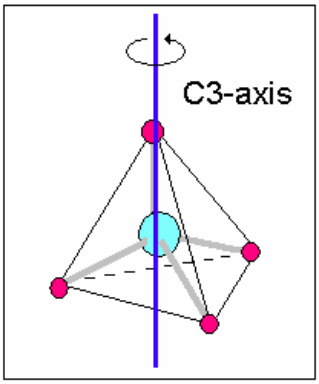

Fig 4-4 *Illustration of* NH_4^+ *rotation around a C3-axis.*

The scattering law for this model is

$$S_3(Q,\omega) = \frac{1}{4} + \frac{3}{4} S_{3sites}(Q,\omega) \qquad \textbf{Eq 4-18}$$

where $S_{3sites}(Q,\omega)$, describes a simple 3-site model of 120° jumps model

$$S_{3sites}(Q,\omega) = A_{3sites}(Q)\cdot\delta(\omega) + [1 - A_{3sites}(Q)]\frac{1}{\pi}\frac{\Delta_3}{\omega^2 + {\Delta_3}^2} \qquad \textbf{Eq 4-19}$$

and the EISF is defined as

$$A_{3sites}(Q) = \frac{1}{3}\left[1 + 2\,j_0\left(Qr_3\sqrt{3}\right)\right] \qquad \textbf{Eq 4-20}$$

where r_3 is the radius of the rotation and $r_3\sqrt{3}$ is the jump distance between the two H atoms.

Using ***Eq 4-19*** and ***Eq 4-20*** the scattering law ***Eq 4-18*** rewrites as

$$S_3(Q,\omega) = A_{03}(Q)\cdot\delta(\omega) + [1 - A_{03}(Q)]\frac{1}{\pi}\frac{\Delta_3}{\omega^2 + {\Delta_3}^2} \qquad \textbf{Eq 4-21}$$

with

$$A_{03}(Q) = \frac{1}{4} + \frac{3}{4} A_{3sites}(Q) = \frac{1}{2}\left[1 + j_0\left(Qr_3\sqrt{3}\right)\right]$$	**Eq 4-22**

As ***Eq 4-15*** (two-site jump model) and ***Eq 4-22*** (three-site jump model, when one of the protons is immobile) are identical for the NH_4^+ rotations, it is theoretically impossible to distinguish these two types of rotations. The only difference is the definition of the HWHM of the quasielastic component.

The HWHM of the Lorentzian function in ***Eq 4-21*** is a proportional to the jump rate of the motion

$$\Delta_3 = \frac{3}{2}\tau_3^{-1}$$	**Eq 4-23**

4.2.1.1.4 Four-site jump model

Another reasonable model suggests that the Hydrogen atoms jump at four sites (corners of a tetrahedron). Ammonium ions rotating due to this model in other compounds have been described previously e.g. [38]. In this model it is assumed that the NH_4^+ undergoes rotations around several C2 and/or C3 axes. In this case the scattering law is

$$S_4(Q,\omega) = A_{04}(Q)\cdot\delta(\omega) + [1 - A_{04}(Q)]\frac{1}{\pi}\frac{\Delta_4}{\omega^2 + {\Delta_4}^2}$$	**Eq 4-24**

with

$$A_{04}(Q) = \frac{1}{4}\left[1 + 3j_0\left(Q\frac{2\sqrt{2}}{\sqrt{3}}d_{N-H}\right)\right]$$	**Eq 4-25**

and

$$\Delta_4 = 4\tau_4^{-1}$$	**Eq 4-26**

The rotations around the C2 and C3 axis are assumed to occur on different timescales. Defining τ_3^{-1} as the jump rate for rotations around the C3 axis and τ_2^{-1} as the jump rate for rotations around the C2 axis, the HWHM can be rewritten as

$$\Delta_4 = \frac{4}{3}\tau_2^{-1} + \tau_3^{-1}$$	**Eq 4-27**

It is impossible to determine τ_3^{-1} and τ_2^{-1} unambiguously, unless the two rotations around the C2 and C3 axis occur on significantly different timescale.

4.2.1.1.5 Libration of ammonium ion

The structural studies of Steiner et al. [6] show that the N-H vector of NH_4^+ points towards the centre of the aromatic rings over the time average, although the H atoms of NH_4^+ have the largest displacement parameters in the crystal structure. Therefore it can be assumed, that NH_4^+ performs large amplitude motions which allow the H atom to move over the whole aromatic face. This kind of motion is explained as a seven-site jump model on a spherical surface [39].

Below, it is assumed that all N-H bonds are equivalent, and thus geometrical description of the motion will be done for only one N-H bond.

Let us assume a rotation axis, noted CR in ***Fig 4-5,*** defined by the middle of a phenyl ring and the position of the N atom of the NH_4^+. The first site, noted S_1 in ***Fig 4-5***, is then defined as the distance r from the Nitrogen atom. Let us now define the six other proton sites, denoted S_i with $i=2...7$ in ***Fig 4-5***. Each of these sites has a probability of $(1-p)/6$. These six equidistant sites are located on a circle perpendicular to the CR axis which has a radius of $r\ sin(\theta)$. The angle θ corresponds to the angle between the CR axis and the N-H vector when one of the sites S_i with $i=2...7$ is occupied.

Thus, a motion of the H atom of NH_4^+ can be described in terms of a 7-site jump model (see ***Fig 4-5***) as follows:

- one site has an occupation probability p, when H points towards the middle of a phenyl ring (S_1)
- the other six sites have an occupation probability of $(1-p)/6$, when H points towards the edge of the phenyl rings (S_i for $i=2...7$).

The seven sites are located on the sphere of the radius r, corresponding to the N-H vector length.

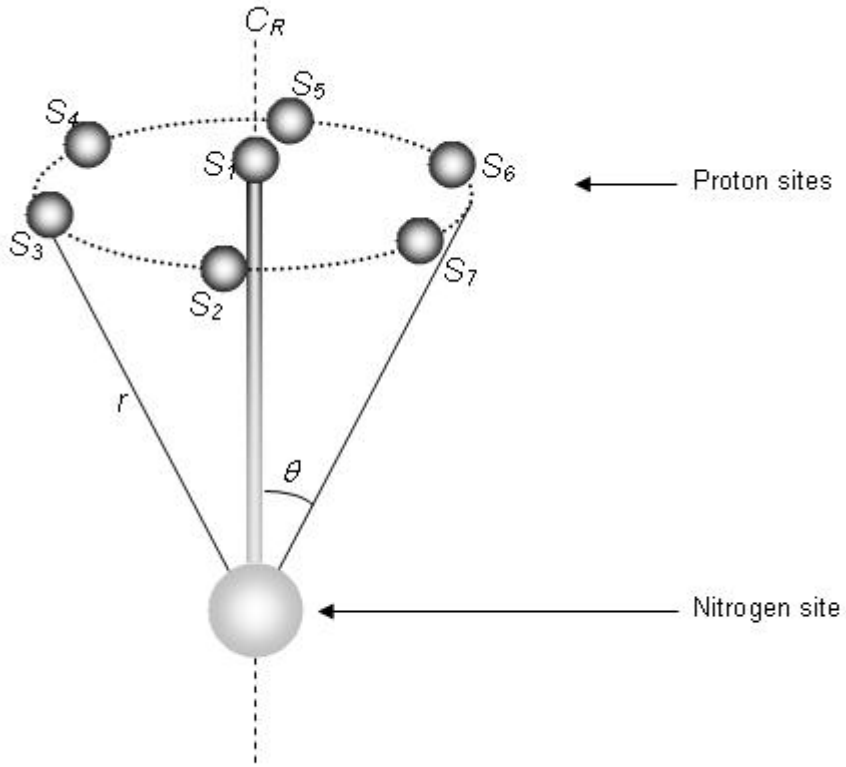

Fig 4-5 *Seven sites visited by the proton of the N-H bond.*

The scattering law for this model is represented by an elastic term added with four additional quasielastic components

$$S_7(Q,\omega) = A_{07}(Q)\cdot\delta(\omega) + \sum_{n=1}^{4} A_{n7}(Q)\cdot\frac{1}{\pi}\frac{\Delta_{n7}}{\omega^2 + \Delta_{n7}^{\ 2}} \qquad \textbf{Eq 4-28}$$

where the EISF $A_{07}(Q)$ is given as

$$A_{07}(Q) = \frac{1}{6}(7p^2 - 2p + 1) + 2p(1-p)\,j_0\left(Qd\sqrt{2(1-\cos\theta)}\right) + \frac{1}{6}(p-1)^2\left[2\,j_0(Qd\sin\theta) + 2\,j_0\left(Qd\sqrt{3}\sin\theta\right) + j_0(2Qd\sin\theta)\right] \qquad \textbf{Eq 4-29}$$

The analytical equations for the four quasielastic structure factors, $A_{n7}(Q)$ for n=1...4, are not given here as they are rather complex. FORTRAN codes to calculate them are given in ***Appendix D.***

The HWHM values Δ_{n7} for *n*=1...4 are

$$\Delta_{17} = \kappa_C + \kappa_R$$

$$\Delta_{27} = \kappa_C + 4\kappa_R$$

$$\Delta_{37} = \kappa_C + 3\kappa_R$$

$$\Delta_{47} = \frac{\kappa_C}{p} \qquad \textbf{Eq 4-30}$$

where κ_R defines the jump rate between two neighbouring sites of the ring (sites S_2 to S_7) and κ_C defines the jump rate from the site S_1 to any of the 6 sites of the ring. One should keep in mind that the probability of site S_1 differs from that of the 6 others sites, so that the jump rate (denoted κ_{j1}) from one site S_j with $j=2..7$ to site S_1 is related to the jump rate (noted $\kappa_{1j} = \kappa_C$) from the site S_1 to one site S_j with $j=2..7$ as

$\kappa_{j1} = \frac{(1-p)}{6p}\kappa_{1j}$	**Eq 4-31**

Assuming that all seven sites have the same probability to be occupied, the jump rate from one site S_j with $j=2...7$ to site S_1 is obviously equal to the jump rate of the site S_1 to one site S_j with $j=2...7$. In other words, if $p=1/7$ in ***Eq 4-31*** leads to $\kappa_{j1} = \kappa_{1j}$ with $j=2...7$.

According to the structural properties, the value of the tilt angle θ can be estimated. It corresponds to half of the angle formed by the Nitrogen atom of the NH_4^+ cation and two opposite carbon atoms of a phenyl rings, i.e. the average value of the tilt angle is $\langle\theta\rangle = 24.6°$ at T=293K and $\langle\theta\rangle = 24.8°$ at T=20K.

Finally, in order to verify this model, the EISF calculated by ***Eq 4-30*** is shown in the ***Fig 4-6*** for a representative set of parameters*. If $p=1$, the EISF equals 1 at any angle, and the proton is in a fixed position S_1 (case (A) in ***Fig 4-6***). The EISF also equals 1 for a tilt angle zero for any probability. If a realistic value is assumed for the tilt angle (e.g. $\theta \approx 25°$) and the observation is limited to a given Q range, then with decreasing probability of the site S_1, the EISF becomes gradually smaller (cases (B), (C) and (D) in ***Fig 4-6***). The last case (E) in ***Fig 4-6*** shows another limit of the model: at a probability of zero and a tilt angle of 90°, the model described in ***Eq 4-28*** is simply a jump model with 6 equivalent and equidistant sites on a circle with a radius r, which is described in [40].

* r was determined as 0.96Å [6]

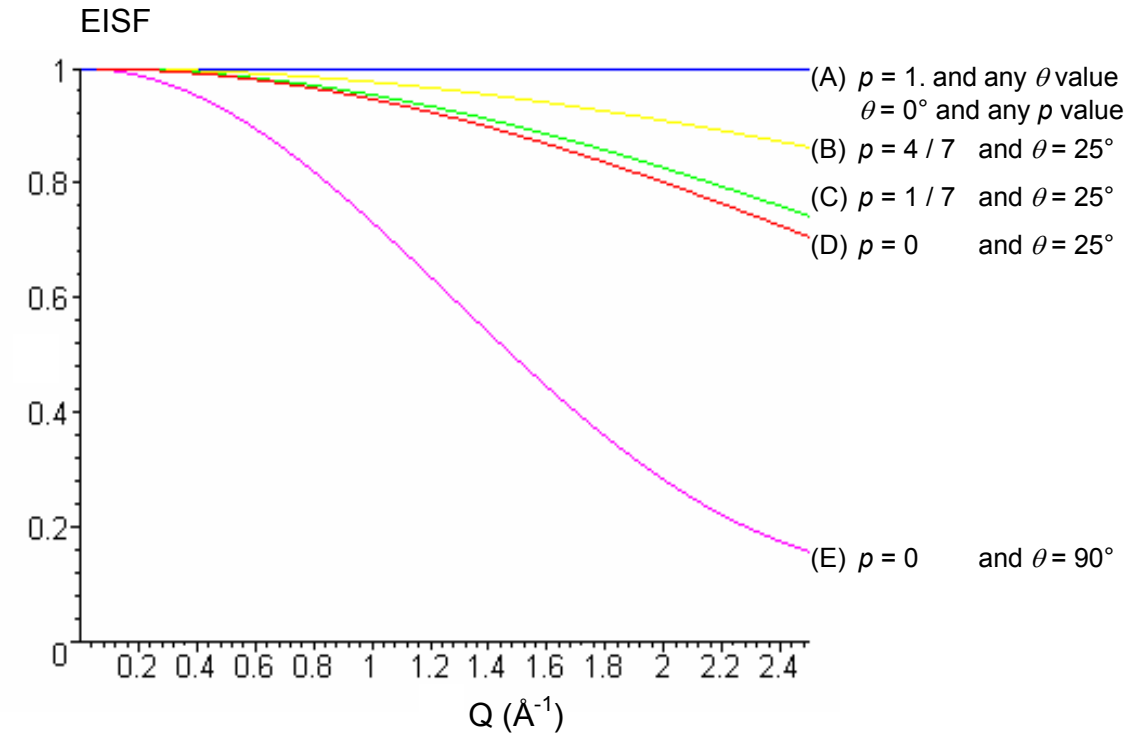

Fig 4-6 *Calculated EISF for different values of θ and p with r=0.96Å.*

4.2.1.1.6 Combination of reorientation and libration

With respect to the symmetry of the sites occupied by NH_4^+, its motions can be described by two components: i) reorientations of the entire NH_4^+ ion and ii) "large amplitude" librations of the N-H vector over the face of the phenyl ring. The Nitrogen atoms (i.e. the centre of mass of NH_4^+) are located in the centre of a distorted tetrahedron (i.e. on a site with $\bar{4}2m$ symmetry). Compared to a perfect tetrahedron (i.e. $\bar{4}3m$ symmetry), the C3 symmetry axis is lost. Consequently, if the NH_4^+ cation is considered to be rigid and thus has a tetrahedral symmetry ($\bar{4}3m$), the $\bar{4}2m$ symmetry of the NH_4^+ site is dynamically understood by a molecular motion (like "large amplitude" librations) in combinations with rotations of the entire NH_4^+ ion.

The reorientations of the entire NH_4^+ ion can be reproduced by one of the jump models described above. The scattering law for any of these three models, given by the equations ***Eq 4-13***, ***Eq 4-21*** and ***Eq 4-24***, is simply the

superimposition of an elastic peak and a quasielastic component with a Lorentzian profile

$$S_{overall}(Q,\omega) = A_0(Q)\cdot\delta(\omega) + (1 - A_0(Q))\frac{1}{\pi}\frac{\Delta}{\omega^2 + \Delta^2} \qquad \textbf{Eq 4-32}$$

where $A_0(Q)$ is the EISF defined in ***Eq 4-15, Eq 4-22*** or ***Eq 4-25*** depending on the model and Δ is the HWHM defined in ***Eq 4-14***, ***Eq 4-22***, ***Eq 4-26*** *or* ***Eq 4-27***.

The combination of the reorientations of the entire NH_4^+ ion with the "large amplitude" librational motions is given by the convolution product of the scattering laws, which assumes that the two motions take place on different timescales and thus no correlations have to be taken into account.

$$S_{eb}(Q,\omega) = S_{overall}(Q,\omega) \otimes S_7(Q,\omega) \qquad \textbf{Eq 4-33}$$

Writing the expressions ***Eq 4-32*** and ***Eq 4-28*** into the equation ***Eq 4-33***, results in a complex quasielastic profile formed by nine Lorentzian functions

$$\begin{aligned} S_{eb}(Q,\omega) &= A_{07}(Q)\cdot A_0(Q)\cdot\delta(\omega) \\ &+ A_{07}(Q)\cdot(1 - A_0(Q))\cdot\frac{1}{\pi}\frac{\Delta}{\omega^2 + \Delta^2} \\ &+ \sum_{n=1}^{4} A_0(Q)\cdot A_{n7}(Q)\cdot\frac{1}{\pi}\frac{\Delta_{n7}}{\omega^2 + {\Delta_{n7}}^2} \\ &+ \sum_{n=1}^{4} A_{n7}(Q)\cdot(1 - A_0(Q))\cdot\frac{1}{\pi}\frac{(\Delta + \Delta_{n7})}{\omega^2 + (\Delta + \Delta_{n7})^2} \end{aligned} \qquad \textbf{Eq 4-34}$$

In this model six independent parameters (r, *p*, θ, κ_R, κ_C and Δ) can be fitted. Two of these parameters are geometrical, i.e. *r*, which depends on the N-H bond length and θ, which can be estimated from the structural results [6].

4.2.1.1.7 Summary of the theoretical models

The theoretical models described above can be classified according to the character of the motion:

- The ***continuous isotropic rotation***, which assumes that the ammonium ion can have any orientation, but that it is arrested in middle of the aromatic cage.
- The ***jump models***, which assume that ammonium has preferential orientations inside the aromatic cage, and it performs jumps between these orientations with a jump rate τ^{-1}.
- The ***large amplitude oscillations*** (librations), which assume that the individual hydrogen atoms of the ammonium ion can librate over the face of the phenyl ring once the ammonium ion has settled on its preferential orientation inside the aromatic cage.

Furthermore a model ***combining the jumps with the librations*** has been introduced.

Fig 4-7 illustrates the elastic incoherent structure factors for the theoretical models described above.

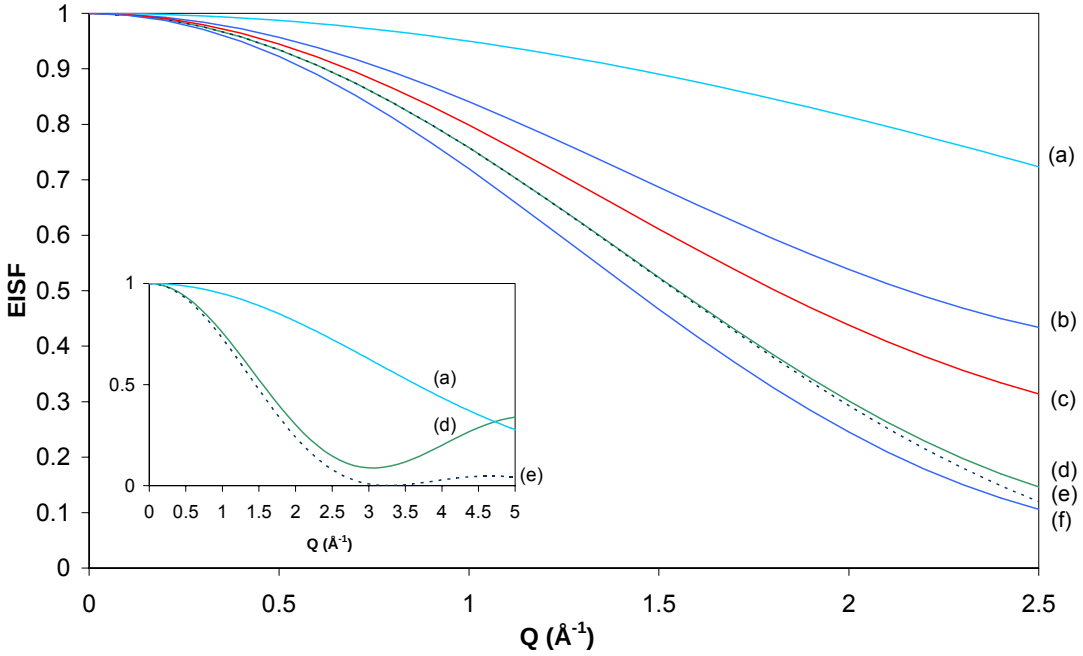

Fig 4-7 *Theoretical models of the elastic incoherent structure factors describing some possible ammonium reorientations in ATPB.*

(a) The librations described by the seven-site jump model in Section 4.2.1.1.5. It is assumed that each site has the same probability.

(b) The two or the three -site jump model described in section 4.2.1.1.2 and 4.2.1.1.3.

(c) The librations (a) combined with the two-site jump model or the three-site jump model (b), as described in section 4.2.1.1.6.

(d) The four-site jump model described in section 4.2.1.1.4.

(e) Dashed line: The continuous rotational diffusion, described in section 4.2.1.1.1. It is assumed that the rotation is limited to a sphere with a radius of 0.9Å, which is the N-H bond length i.e. the ammonium rotates around its centre of mass (nitrogen site) without having a preferential orientation. The first term in Eq 4-12, $\ell = 0$, corresponds to the EISF.

(f) The librations (a) combined with the four-site jump model (d), as described in section 4.2.1.1.6

The Q range accessible by NEAT measurements is shown here. In this Q range the four-site jump model and the continuous rotational diffusion are similar. Differences in the EISF of these motions can only be seen at higher Q values, as shown in the insert.

4.2.1.2 Data analysis

4.2.1.2.1 Phenomenological fits

As a first step of the analysis of the QENS spectra, phenomenological fits were performed in order to find a suitable model for the NH_4^+ reorientations. In this procedure the structure factors EISF (elastic incoherent structure factor) and QISF (quasielastic incoherent structure factor) are fit parameters, as well as the width of the quasielastic component (HWHM=Δ). Only the weight factors for both components are defined assuming that the phenyl rings are immobile on the time scale of our measurements. Therefore the phenyl rings would only contribute to the elastic part of the QENS spectra. The fitted scattering function for the phenomenological procedure is

$$S_{PHE1}(Q,\omega) = e^{-\frac{\hbar\omega}{2k_BT}} e^{-2W} \left\{ \left[\frac{5}{6} + \frac{1}{6} A_0(Q) \right] \delta(\omega) + \frac{1}{6} \left[1 - A_0(Q) \right] \frac{1}{\pi} \frac{\Delta(Q)}{\omega^2 + \Delta^2} + S_{inc}^I(\vec{Q},\omega) \right\} \quad \text{Eq 4-35}$$

where $A_0(Q)$ is the EISF and 1- $A_0(Q)$ is the QISF. $S_{inc}^I(\vec{Q},\omega)$ is the inelastic background, here fitted by a straight line to reproduce qualitatively the contribution of the inelastic spectrum in the QE region. In the phenomenological fitting procedure, the energy transfer window was limited to the range of -1.5meV and 1.5meV.

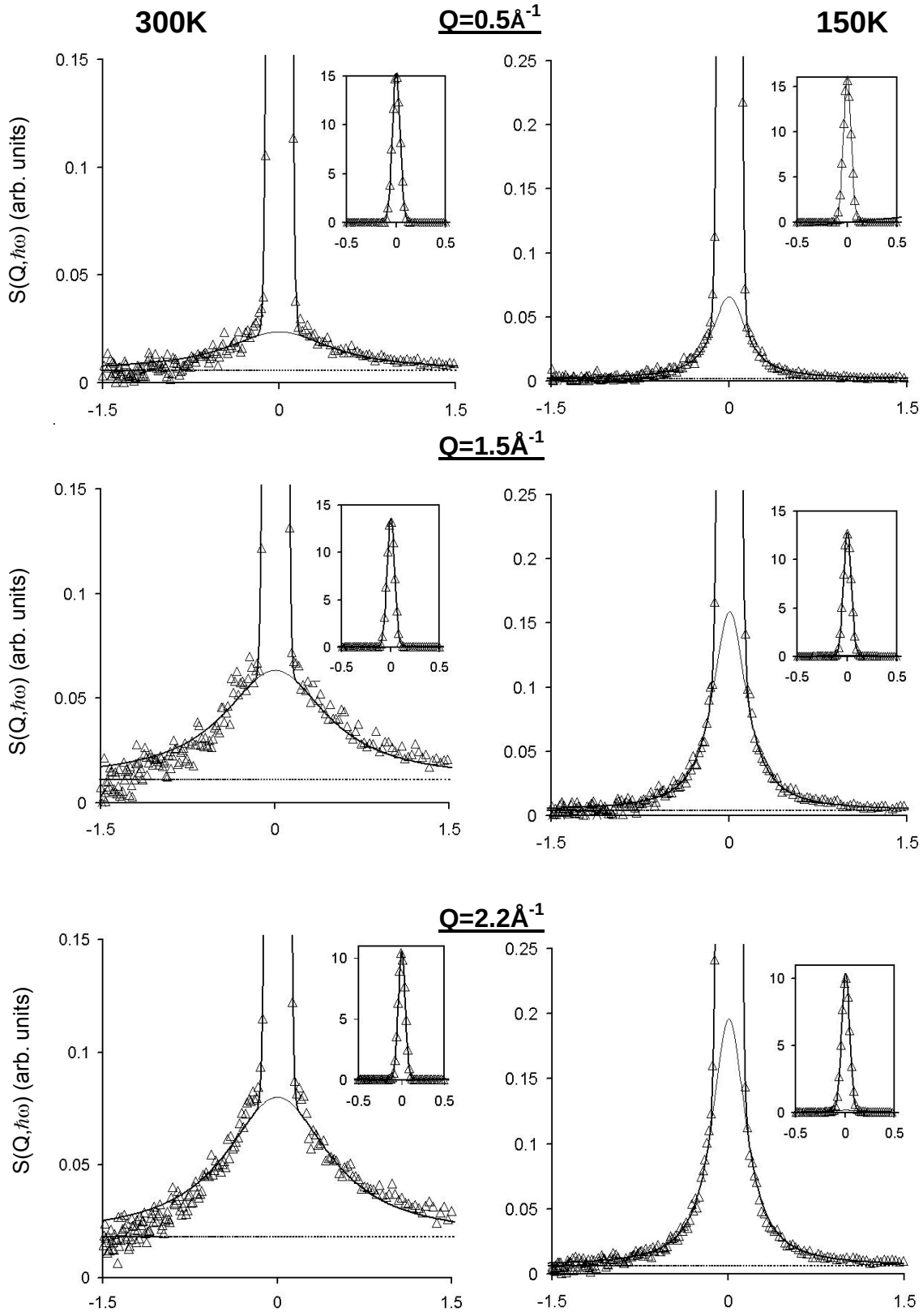

Fig 4-8 *The triangles show the measured ATPB spectra at ΔE=98μeV, T=150K (right hand side) and T=300K (left hand side). The dotted straight line is the fitted background and the Lorentzian shaped line is the fitted QE component. The complete fitted scattering functions are shown in the inserts.*

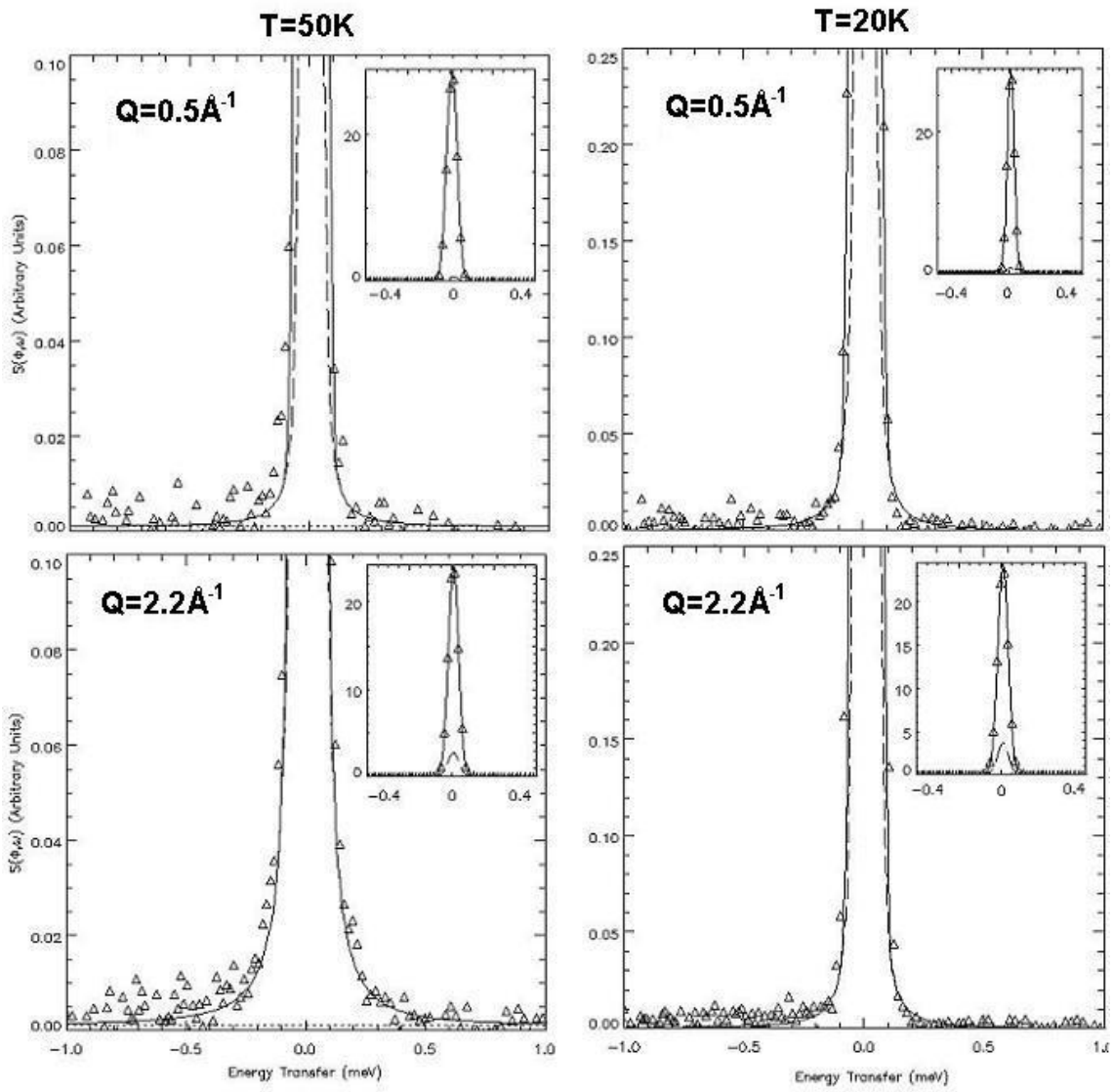

Fig 4-9 *The triangles show the measured ATPB spectra at ΔE=56μeV at T=20K (right hand side) and T=50K (left hand side). The dotted straight line is the fitted background and the Lorentzian shaped line is the fitted QE component. The complete fitted scattering function is shown in the inserts. The complete fitted scattering functions are shown in the inserts.*

In ***Fig 4-8*** the results of the fits at ΔE=98μeV, at T=150K (right hand side) and T=300K (left hand side) are shown at three selected Q-values. The quasielastic contributions are rescaled in order to show the fit quality of the phenomenological Lorentzian function. The corresponding complete spectra are shown in the inserts. This demonstrates how small the quasielastic component is compared to the elastic peak. In the temperature range 200<T<300K the fitted and the experimental data deviate near to the elastic region (see T=300K in ***Fig 4-8***). Because of the nature of the deviations, at least one additional Lorentzian function may be needed to describe the data correctly.

With decreasing temperature the width of the quasielastic component is reduced, due to a slowing down of the diffusive motions. As a consequence another time scale is needed, therefore the fits for temperatures 50K and 20K were produced using higher energy resolution, i.e. ΔE=56μeV (see ***Fig 4-9***). It has to be noted that the experimental QE contribution is broader than the one reproduced here by the fits. The deviations occur at the lower part on the sides of the elastic peak, while the wings of the QE component as well as the height of the elastic peak are both well reproduced. Reason for this kind of deviations can be understood qualitatively regarding to a previous study of Roberts et al. [41], where tunneling of the ammonium ions in ATPB was observed. Our experimental energy resolution was not sufficient to properly separate these tunneling frequencies from the resolution function, but it is expected that the tunneling would cause a slight broadening for the elastic line.

Furthermore, the largest difference between the fitted and the experimental data occurs for any temperature at low Q values (i.e. Q=0.5Å^{-1} in ***Fig 4-8*** and ***Fig 4-9***). In order to get more insight on the motions involved, a careful analysis of the EISF and HWHM was performed.

An approximate description of the diffusive motions of the NH_4^+ ion can be derived from the phenomenological fits by comparing the obtained experimental EISF values to the theoretical ones (explained in the ***Section 4.2.1.1***). Because the experimentally determined EISF values change dramatically at the

temperatures below 150K, two temperature regions were considered separately **(a)** 150K≤T≤300K and **(b)** 20K≤T≤100K.

As shown in ***Fig 4-10*** **(a)** at a temperature T=200K, the experimental EISF values show a behaviour, which almost correspond to the theoretical model of the ammonium ion rotation around the C2/C3 axis. An alternative possibility is to combine the ammonium ion librations with the rotation around the C2/C3 axis. Thus the model of ammonium ion rotations around the C2/C3 axis will be used first to fit the experimental data (see the following section).

As shown in ***Fig 4-10 (b)*** at lower temperatures 20K≤T≤100K, the experimental EISF values do not correspond to the behaviour predicted by the considered theoretical models. Anyhow, regarding to the fit quality at the lower temperatures (see ***Fig 4-9***) it is not assumed that the ammonium motions can be explained as classical diffusive rotations. Therefore conclusions can not be carried out concerning the EISF behaviour at the lower temperatures.

In rotational diffusive motions, a molecule has to overcome the potential energy barrier of its nearest neighbors. The activation energy, which is the difference between the height of the potential barrier and the librational ground state, can be determined by analysing the thermal evolution of the HWHM.

The rotational diffusion is usually found to vary with the temperature with an Arrhenius like behaviour

$\tau^{-1} = \tau_0^{-1} e^{-E_a / k_B T}$	**Eq 4-36**

where τ^{-1} is the jump rate, τ_0^{-1} is the attempt frequency, E_a is the activation energy, k_B is the Boltzmans' constant and T is the temperature.

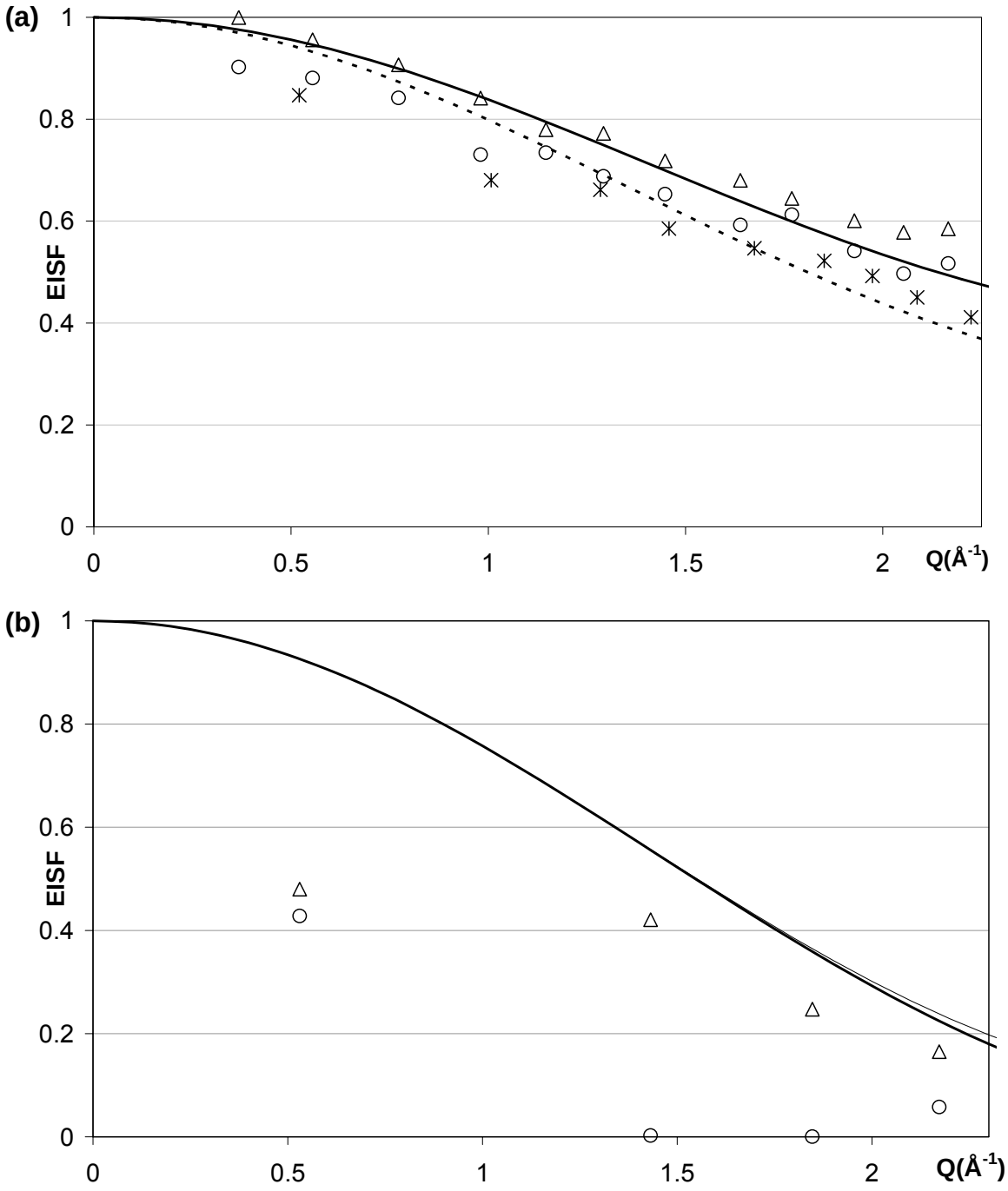

Fig 4-10 *Selected behaviour of the fitted EISF(Q) as determined by the phenomenological fits (symbols) compared with the theoretical models described in the* ***section 4.2.2.1*** *(represented by lines).*

(a) T=200K; ΔE=56μeV(crosses), ΔE=98μeV(circles), ΔE=182μeV(triangles). The solid line is the EISF for the two-/three-site jump model and the dashed line is the EISF for two-/three-site jumps combined with librations.

(b) T=100K; ΔE=56μeV (triangles) and T=20K; ΔE=56μeV (circles). The lines are the EISF for four-site jump model and for the continuous isotropic rotation.

In ***Fig 4-11*** the HWHM values obtained from the phenomenological fits are shown as a function of the inverse temperature. Fitting ***Eq 4-36*** for temperatures between 67≤T≤300K an activation energy of about 3kJ/mol was obtained. As expected, at the temperatures between 20K≤T≤67K the behaviour of the HWHM values does not follow the same behaviour as above 67K. This indicates to a change of the dynamical process in the sample.

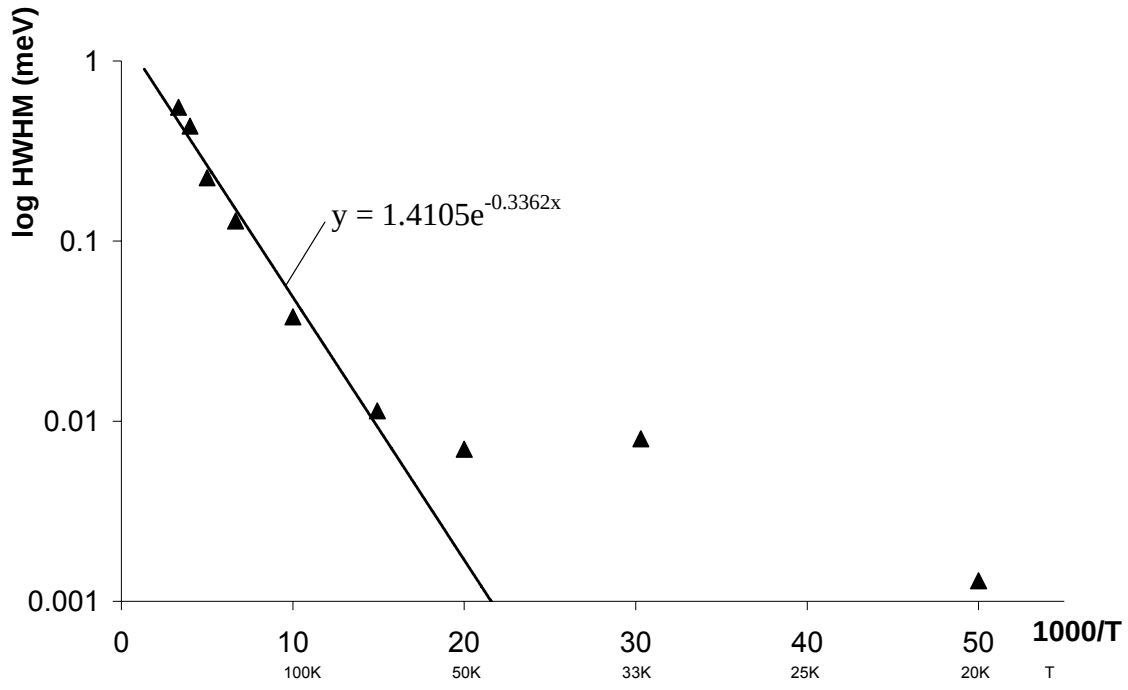

Fig 4-11 *Thermal evolution of the HWHM*

4.2.1.2.2 Two-site jump model

As a second step of the data analysis the two-site jump model was fitted without considering librations. The EISF is here no longer a fit parameter, since it is given by the model. The weight factors were defined in the same way as in the previous section considering only the ammonium ion reorientations. The fitted QE scattering function for the two-site jump model given in the ***Eq 4-13*** can be written as

$$S_{2site-jm}(Q,\omega) = e^{-\frac{\hbar\omega}{2k_BT}} e^{-2W} \left\{ \frac{5}{6} + \frac{1}{6}\left(\frac{1}{2} + \frac{1}{2}\frac{\sin Qd}{Qd} \right)\delta(\omega) + \frac{1}{6}\left(\frac{1}{2} - \frac{1}{2}\frac{\sin Qd}{Qd} \right)\frac{1}{\pi}\frac{2\tau_2^{-1}}{\omega^2 + 4\tau_2^{-2}} + S_{inc}^{1}(\vec{Q},\omega) \right\} \qquad \text{Eq 4-37}$$

where d is jump distance 1.6Å, according to the crystalline structure [6]. The jump rate τ_2^{-1} was the main fit parameter and the inelastic background was fitted with a straight line as a function of ω.

Due to the different nature of the fits, the results of the two-site jump model will be introduced here separately for three temperature regions

i. T>200K

In this temperature range the two-site jump model could not reproduce the total experimentally observed QE intensity. Instead significant deviations occur near the elastic peak between the experimental data and the fitted model, an example at T=300K is shown in ***Fig 4-12***. Comparing these findings with the results presented in the previous section, it becomes obvious that the deviations have a similar nature as those seen in ***Fig 4-8*** at T=300K. As already indicated in context with the phenomenological approach, one Lorentzian function, here the two-site jump model, is not sufficient to explain the QE component observed experimentally. Indeed, an additional narrow QE component is needed to reproduce the experimental data accurately. As the width of the quasielastic component is inversely proportional to the

correlation time of the proton dynamics in the sample, it can be assumed that the narrow component originates from a rather slow motion (compared to the ammonium ion rotations). The librations of the N-H vector explained in ***section 4.2.1.1.6*** are supposed to be faster as they occur between the ammonium ion rotations and can thus hardly be seen as a source of this kind of narrow component. Therefore it can be suggested that the narrow component originates from motions of the phenyl rings. To investigate the origin of this additional quasielastic component accurately, the deuteration of the ammonium ion in ATPB has been used as a tool. In section ***4.2.2*** this question is discussed in detail, and models for possible motions of the phenyl rings are introduced and fitted to the experimental data.

ii. 200K≥T≥67K

In this temperature region, the two-site jump model reproduces the experimental data well, as e.g. shown in ***Fig 4-12*** at T=150K. The deviations observed at the lowest Q values are most probably due to the multiple scattering effect. The jump rates vary from 0.15meV* at T=200K to 0.0033meV† at 67K. The temperature dependence of the jump rate in this temperature region is shown in ***Fig 4-14***. The Arrhenius law (given in ***Eq 4-36***) is fitted to the data points and the resulting activation energy is 3.2kJ/mol. This result is consistent, but more accurate as the one that we found using the phenomenological approach (see previous section).

iii. 50K≥T≥20K

As expected from the results of phenomenological approach and as shown in ***Fig 4-13***, the two-site jump model could not reproduce the total intensity of the QE component. The observed deviations between the experimental data and the fitted two-site jump model are similar as the ones seen when the phenomenological approach was fitted (see ***Fig 4-9***). Our interpretation for the low temperature data was already discussed in the context of the phenomenological approach.

* corresponds to a correlation time of 28ps
† corresponds to a correlation time of 1253ps

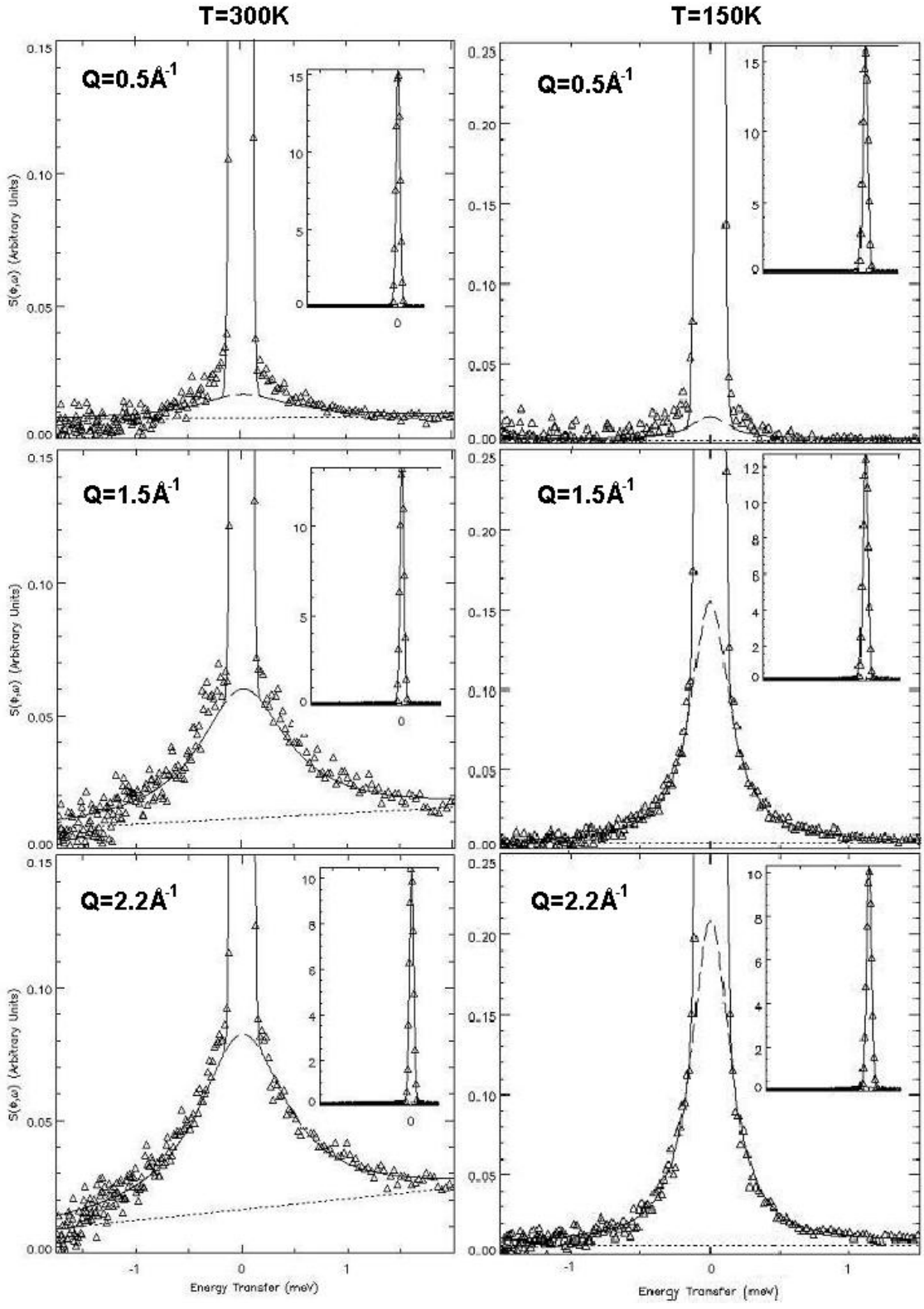

Fig 4-12 *The fitted two-site jump model at ΔE=98μeV, T=300K (right hand side) and T=150K (left hand side). The triangles show the measured ATPB spectra. The dotted straight line is the fitted background and the Lorentzian shaped line is the fitted QE component. The complete fitted scattering functions are shown in the inserts.*

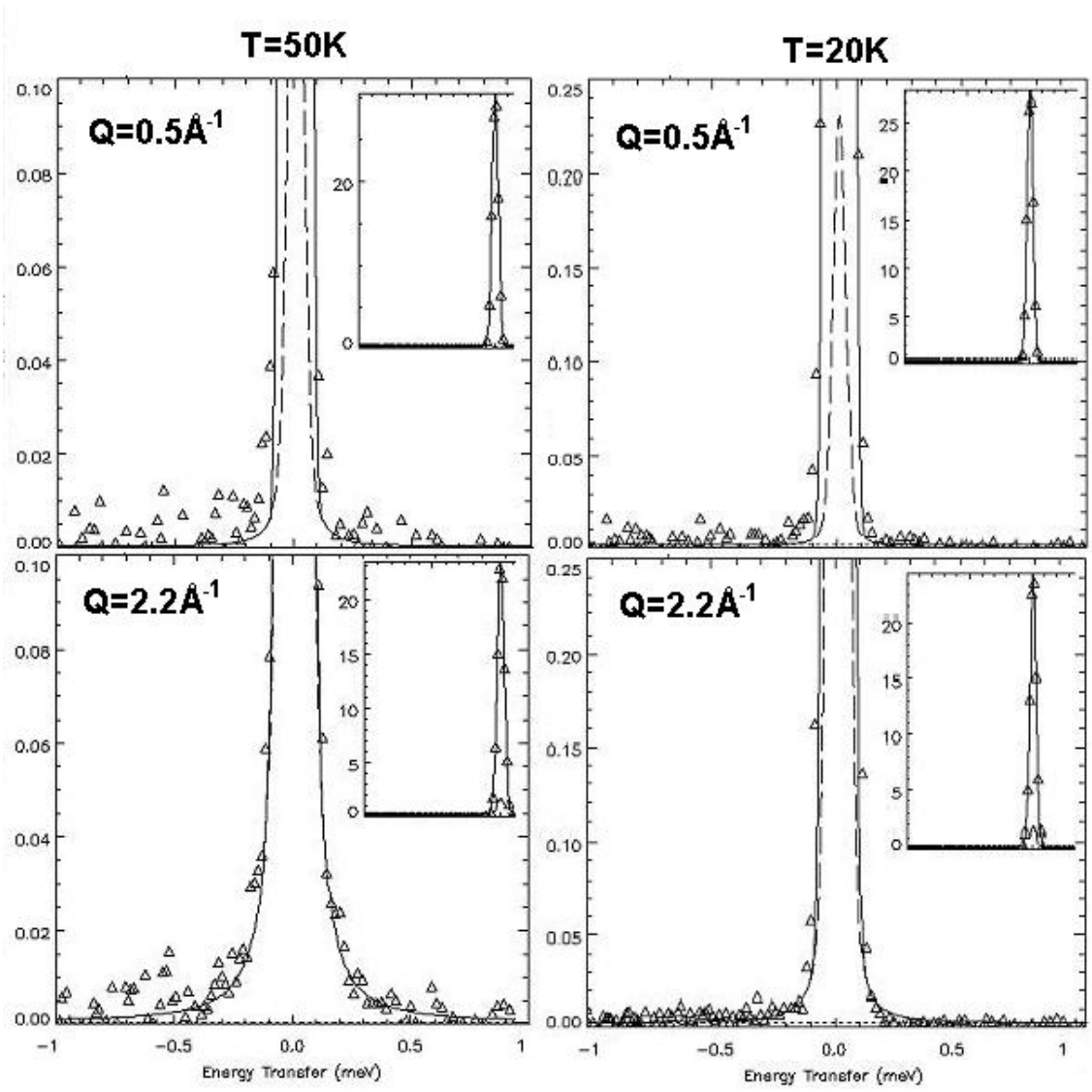

Fig 4-13 *The fitted two-site jump model at ΔE=56μeV, T=50(right hand side) and T=20 (left hand side). The triangles show the measured ATPB spectra. The dotted straight line is the fitted background and the Lorentzian shaped line is the fitted QE component. The complete fitted scattering function is shown in the inserts.*

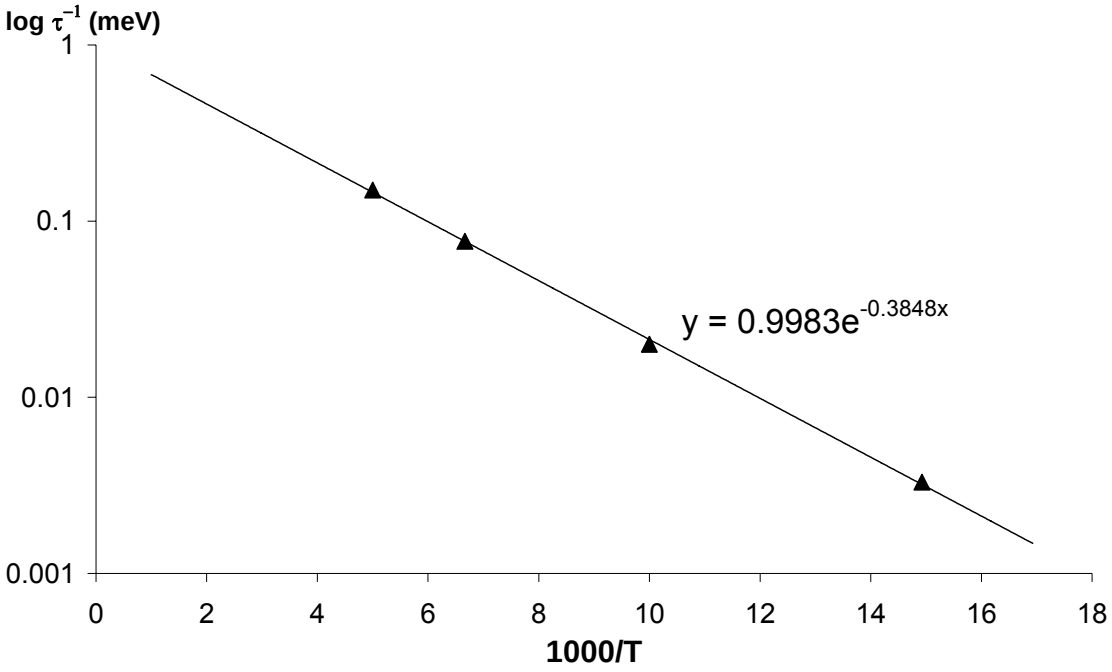

Fig 4-14 *Thermal evolution of the jump rate of the two-site jump model. The experimental points are labeled with triangles. The solid line represents the fitted Arrhenius law.*

4.2.2 Phenyl ring reorientations

According to the results presented in the previous section, the additional narrow QE component may originate from reorientational motions of the phenyl rings. To verify this idea, selective deuteration of the ammonium groups was used to measure the QE component resulting from the phenyl rings. In this chapter theoretical models for possible local diffusive motions of reorientation of the phenyl rings are presented and combined together with the motions of the ammonium ions. Finally the models are tested by fitting them to the experimental data.

As a consequence of the momentum of inertia, the motions of the phenyl rings are expected to be slower than the rotations of the ammonium ions. Furthermore in previous QENS studies on other solid compounds [42], [43] & [44], the local diffusive motions of orientation of the phenyl rings have been observed on a time scale of 10^{-11}s to 10^{-9}s at room temperature. Thus the energy resolution of 32μeV which corresponds to a time scale of about 10^{-10}s was used to measure the QENS spectra of the ATPB-d.

4.2.2.1 Theoretical models

A model for a QE component due to overdamped librational motions of the phenyl rings have been described here, for simplicity, by a reorientational jump-diffusion model. This model concerns reorientation of the phenyl rings around an axis, which passes through its two opposite corners, as shown in ***Fig 4-15***. The phenyl ring is assumed to be rigid, and when the rotation axis is turned, all of the mobile atoms move at same time to the direction of the reorientation. The distance between the positions of the hydrogen atoms before and after the reorientation will herein after be called as “jump distance”. The jump distance is related to the angle of the reorientation, which is defined as shown in the insert of the ***Fig 4-15***. Knowing the crystal structure [6] (given in ***Table 3***), some possible jump distances can be obtained by a simple calculation based on trigonometry.

First the distance from the mobile H atoms (located at C2, C3, C5 and C6 sites) to the rotation axis is calculated. It amounts to 2.165Å. This value is then used to obtain different jump distances (see ***Table 4***.) by varying the reorientation angle α. If an angle $\alpha=180°$ is assumed, the phenyl rings rotate around a C2 axis, and we talk about phenyl ring flips. If the reorientation angle $\alpha<180°$ the phenyl rings librate out of the plane.

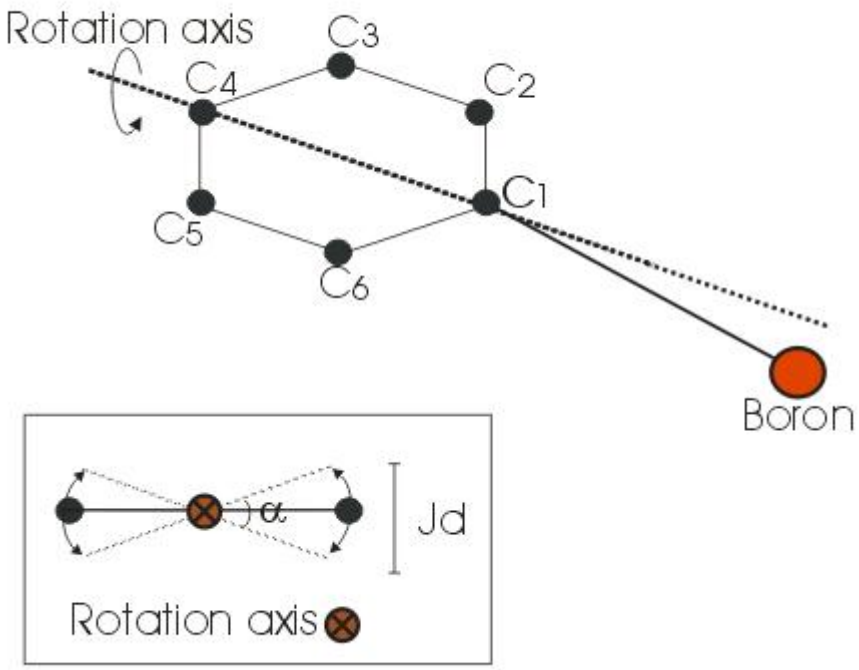

Fig 4-15 *The motions of the phenyl rings in ATPB can be described as a reorientation around an axis, denoted as a dashed line in the larger figure. In the insert the phenyl ring is reviewed at the same plane is shown. The solid line represents the equilibrium position of the phenyl ring, and the dashed lines show the limits of the libration. The jump distance (Jd) is the distance and the reorientation angle α the angle between the extreme positions.*

Distance	(Å)
B-C1	1.638
C-C, mean	1.400
C-H, mean	1.090

Angle	(°)
B-C1···C4	172.8

Table 3 *Geometrical data of ATPB at 293K* [*6*]

Angle α(°)	Jump distance (Å)
180	4.33
135	4.00
90	3.06
60	2.165
45	1.66
30	1.12
15	0.57
10	0.38
5	0.19

Table 4 *Jump distances for different reorientation angles, which results from the ATPB crystallographic structure.*

The theoretical model for this reorientation of the phenyl rings around an axis can be expressed by means of the two-site jump model (see ***section 4.2.1.1.2***), and the Elastic Incoherent Structure Factor (EISF) for the motions of the phenyl rings are thus given by

$$A_{02}(Q) = \frac{1}{2}\left[1 + j_0\left(2Qr^{Ph}\right)\right] \qquad \textbf{Eq 4-38}$$

where $2r^{Ph}$ is the jump distance and j_0 the spherical Bessel function of zero order. The analysis aims at finding a value for the reorientation angle, which is connected to the jump distance. Taking into account that the EISF depends on the jump distance, it is worth to illustrate the Q dependence of EISF for selected jump distances, as shown in ***Fig 4-16***.

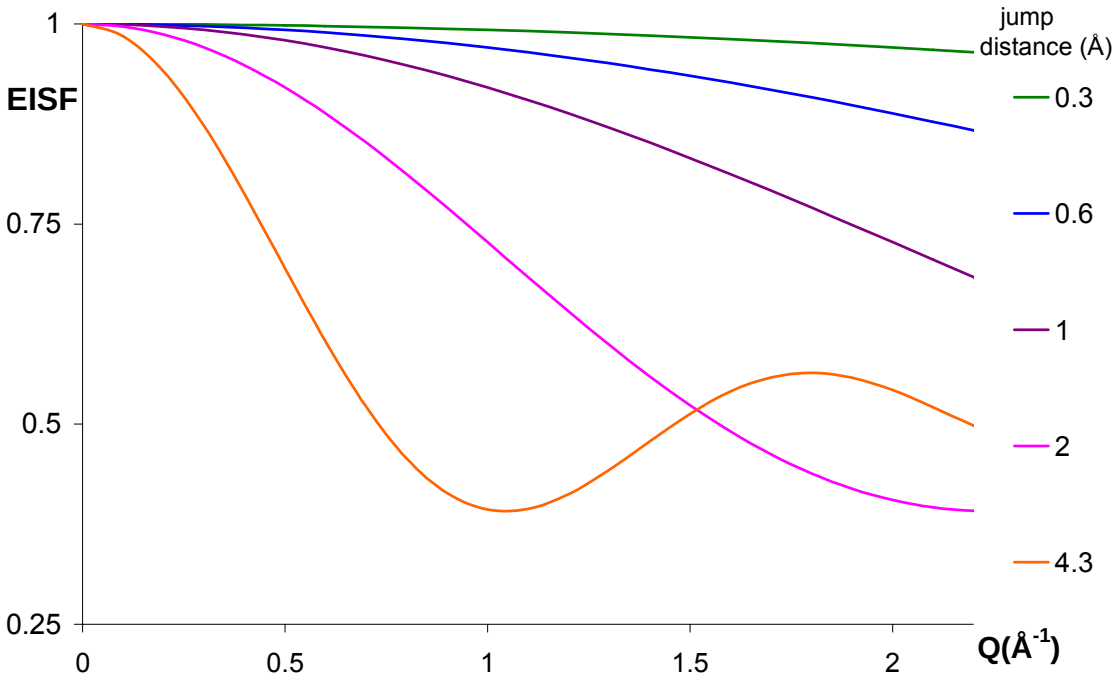

Fig 4-16 *EISF(Q) for phenyl ring flips (jump distance =4.3Å) and librations for several possible jump distances (<4.3Å).*

4.2.2.2 Data analysis

By selective deuteration of the ammonium groups, the measured QE neutron scattering of the ATPB-d sample is dominated by the incoherent contribution of the hydrogen atoms in the phenyl rings. Although the deuteration of ammonium groups was not complete (77%), a drastic reduction of the incoherent contribution of the ammonium ions is expected.

In fact, the contribution of the 77% deuterated ammonium ion rotations only amounts to about 5% of the whole spectrum, about 1% of which results from coherent and about 4% from incoherent scattering. In order to obtain the right intensity factor for the contribution of the ammonium ion, the coherent contribution has to be taken into account as well. The theory describing the intensity distribution of coherent scattering is rather complicated, but not necessary for this analysis. Instead a good approximation of the rotations of the ammonium ions has been obtained by using the percentage of its total

scattering cross section. As shown in the previous section the ammonium ions rotate around C2 axis in a certain temperature range (67K≤T≤300K). This model was also applied to the rotations of the ammonium ions in the ATPB-d.

First to analyse the existence of the second QE component in the ATPB-d sample, only the two-site jump model for the rotations of the ammonium ions was used to reproduce the experimental spectra. The phenyl rings were considered as immobile, contributing only to the elastic intensity.

The two-site jump model for ATPB-d is given by

$$S_{ATPB-d}^{2sites}(Q,\omega) = e^{-\frac{\hbar\varpi}{2k_BT}} \cdot e^{-2W}\left\{\left[\frac{5.3}{100}A_{02}^{Am} + \frac{94.7}{100}\right]\delta(\omega) + \frac{5.3}{100}\cdot\left[1 - A_{02}^{Am}\right]\frac{1}{\pi}\frac{\Delta_{02}^{Am}}{\omega^2 + \left(\Delta_{02}^{Am}\right)^2} + S_{inc}^{I}(Q,\omega)\right\}$$

Eq 4-39

where A_{02}^{Am} is the EISF of the two-site jump model (given by ***Eq 4-15***) and Δ_{02}^{Am} is the HWHM for the rotation of the ammonium ions around the C2 axis. $S_{inc}^{I}(Q,\omega)$ is the inelastic background reproduced by a straight line. The main fit parameter is the Δ_{02}^{Am}.

The result of the fit at T=300K is shown in ***Fig 4-17***. The spectra of all angles were grouped together which results in an average Q value of 1.05Å^{-1}. The jump rate obtained for the partly deuterated ammonium ion rotation around the C2 axis is 0.27meV. Clearly, the experimental intensity of the QE component was not well reproduced by this model and thus an additional QE component has to be introduced to explain the spectra of ATPB-d.

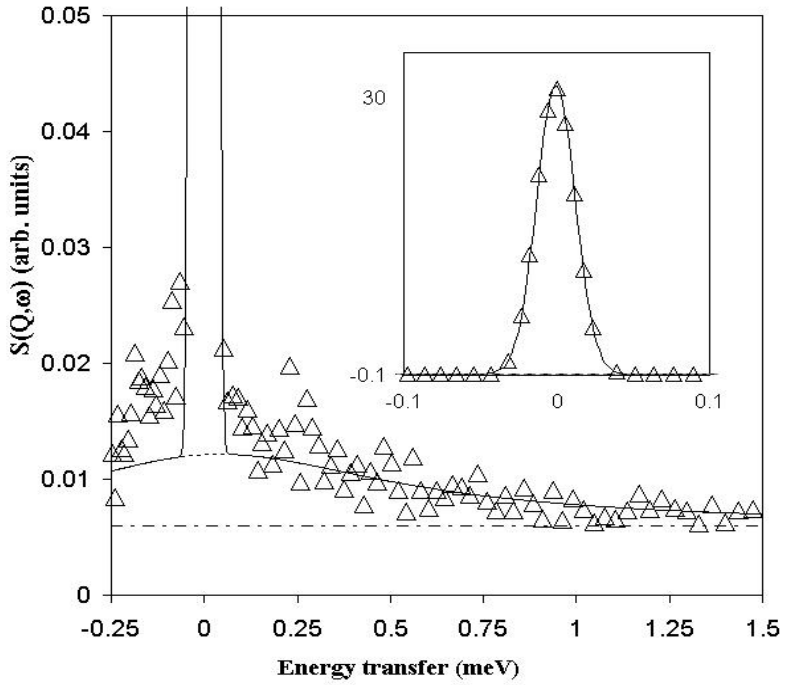

Fig 4-17 *The two-site jump model fitted to the measured spectra of ATPB-d at T=300K, Q=1.05Å^{-1} and ΔE=32μeV. The triangles present the experimental data, the solid line the fitted function, the Lorentzian shaped dashed line is the QE contribution and the straight dashed line is the fitted background. In the insert the corresponding elastic contribution is shown.*

To reproduce the additional QE intensity, the above presented model for the reorientational motions of the phenyl rings should be considered together with the rotations of the ammonium ions. The intensity factor for the motions of the phenyl rings has been obtained by using the total scattering cross section percentage of the mobile protons in the phenyl rings. As the total scattering cross section of the mobile carbon atoms in the phenyl rings is negligible and they are located closer to the rotation axis than the hydrogen atoms their motion produces only very little intensity. Thus the QE component of the carbon scattering is not considered here.

The scattering function combining the two-site jumps of the ammonium ions and the reorientations of the phenyl rings in ATPB-d can now be written as

$$S_{ATPB-d}^{Am\&Ph}(Q,\omega) = e^{-\frac{\hbar\omega}{2k_BT}} \cdot e^{-2W} \left\{ \left[\frac{5.3}{100} A_{02}^{Am} + \frac{68}{100} A_{02}^{Ph} + \frac{26.7}{100} \right] \delta(\omega) \right.$$
$$\left. + \frac{5.3}{100} \cdot \left[1 - A_{02}^{Am} \right] \frac{1}{\pi} \frac{\Delta_{02}^{Am}}{\omega^2 + \left(\Delta_{02}^{Am}\right)^2} + \frac{68}{100} \cdot \left[1 - A_{02}^{Ph} \right] \frac{1}{\pi} \frac{\Delta_{02}^{Ph}}{\omega^2 + \left(\Delta_{02}^{Ph}\right)^2} + S_{inc}^{I}(Q,\omega) \right\}$$

Eq 4-40

where A_{02}^{Am} (given by ***Eq 4-15***) and A_{02}^{Ph} (given by ***Eq 4-38***) are the EISF and Δ_{02}^{Am} and Δ_{02}^{Ph} are the HWHM for the rotation of the ammonium ions and the phenyl rings around the C2 axis respectively. $S_{inc}^{I}(Q,\omega)$ is the inelastic background, produced here by a straight line.

The experimental ATPB-d spectra were reproduced by the model given in ***Eq 4-40***. The energy transfer window was from -0.15meV to 1.5meV and the data were sorted into three groups, to obtain information about the Q dependence of the motions of the phenyl rings. The fit parameters were Δ_{02}^{Ph} and the jump distance of the phenyl ring motions, $2r^{Ph}$ in ***Eq 4-38***.

In ***Fig 4-18*** two fit results for ATPB-d spectra at T=300K, ΔE=32μeV and at Q=1.3Å^{-1} are shown. In both cases the jump rate of the ammonium ions was fixed at 0.27meV. For phenyl ring reorientations were found in (a) a jump distance of 0.2Å, which corresponds to a reorientations angle of about 5° and a jump rate of 0.04meV and in (b) a jump distance of 0.25Å, which corresponds to a reorientations angle of about 7° and a jump rate of 0.03meV. The librations of the phenyl rings produce a rather weak QE component, which is only 0.65% of the whole spectra, when the reorientation angle of 7° is considered and 0.56% when the reorientation angle of 5° is considered. The fits shown here reproduce the experimental data well. However, it is not possible to define the jump distance and the jump rate for the motions of the phenyl rings accurately at same time. At T=300K a jump distance of 0.25±0.05Å corresponding to a reorientation angle of 7°±2° and the jump rate of 0.03±0.01meV were defined.

To verify the hypothesis, that the additional narrow QE component originates from the reorientations of the phenyl rings, the QE spectra of ATPB-d was compared with the ATPB spectra. The model combining the motions of the ammonium ions and the phenyl rings was used to reproduce the experimental data of the ATPB sample. Due to the different scattering cross sections of the samples the weight factors vary from those in ***Eq 4-40***. The fitted scattering function for ATPB is

$$S_{ATPB}^{Am\&Ph}(Q,\omega) = e^{-\frac{\hbar\varpi}{2k_BT}} \cdot e^{-2W} \left\{ \left[\frac{4}{24} A_{02}^{Am} + \frac{16}{24} A_{02}^{Ph} + \frac{4}{24} \right] \delta(\omega) \right.$$
$$\left. + \frac{1}{24} \cdot \left[1 - A_{02}^{Am} \right] \frac{1}{\pi} \frac{\Delta_{02}^{Am}}{\omega^2 + \left(\Delta_{02}^{Am} \right)^2} + \frac{16}{24} \cdot \left[1 - A_{02}^{Ph} \right] \frac{1}{\pi} \frac{\Delta_{02}^{Ph}}{\omega^2 + \left(\Delta_{02}^{Ph} \right)^2} + S_{inc}^{1}(Q,\omega) \right\}$$

Eq 4-41

where Δ_{02}^{Am} and Δ_{02}^{Ph} are the HWHM values, $A_{02}^{Am}(Q)$ (given by ***Eq 4-15***) and $A_{02}^{Ph}(Q)$ (given by ***Eq 4-38***) are the EISF for the rotation of the ammonium ions and the phenyl rings around the C2 axis.

The fits of the ATPB spectra were produced like the ATPB-d fits. In ***Fig 4-19*** the fit results at Q=1.3Å^{-1} are shown at two temperatures (a) T=300K and (b) T=350K. At T=300K the result of the fit is shown with the same parameters that were obtained for ATPB-d in ***Fig 4-18 (b)***, i.e. a jump rate of the phenyl ring reorientations of 0.03meV*, a jump distance of the phenyl ring reorientations of 0.25Å, and a jump rate of the ammonium ions rotations of 0.27meV†. These parameters reproduce the experimental spectra well for both samples. At T=350K the fitted parameters are a jump rate of the ammonium ions of 0.33meV‡, a jump rate of the phenyl rings of 0.045meV§, and a jump distance of the phenyl rings of 0.3Å. This observation indicates that both the jump rate and the jump distance of the librations of the phenyl rings increase with temperature.

* corresponds to a correlation time of 150ps
† corresponds to a correlation time of 15.3ps
‡ corresponds to a correlation time of 12.5ps
§ corresponds to a correlation time of 92ps

(a)

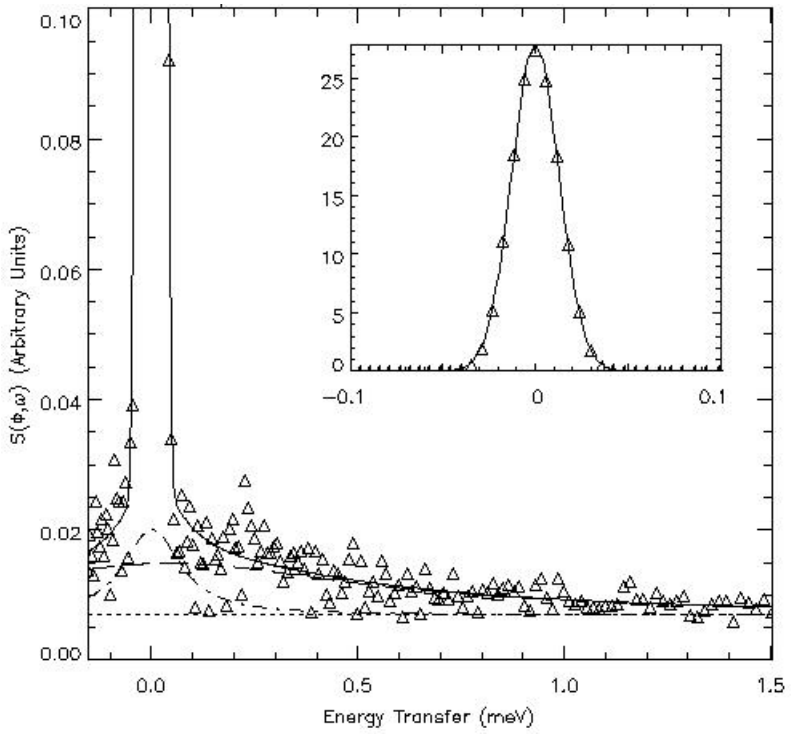

(b)

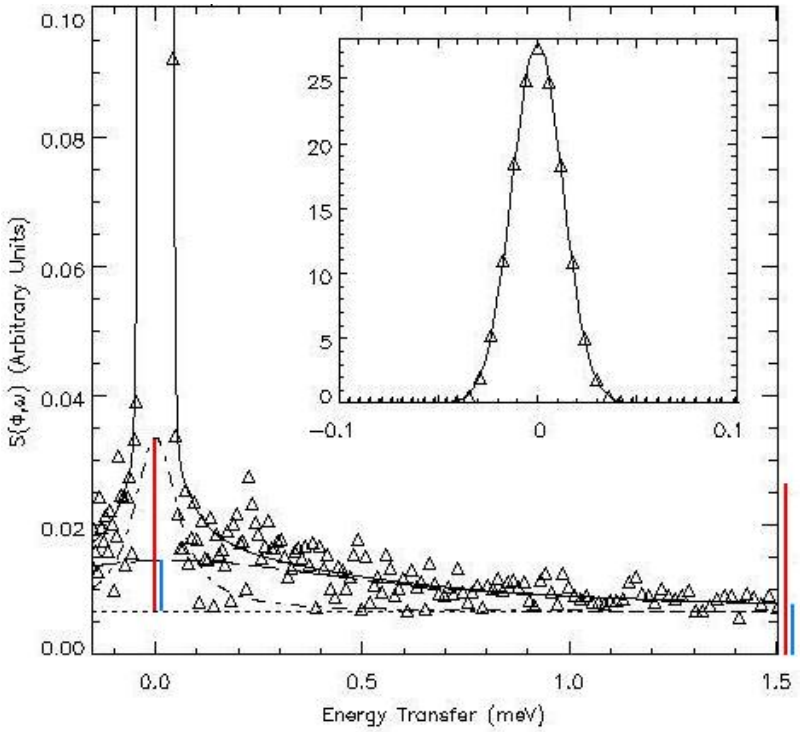

Fig 4-18 *The QENS spectra of ATPB-d (triangles) measured at T=300K, at ΔE=32μeV and at average Q value of 1.3Å^{-1} reproduced by two different sets of fit parameters. The model includes a contribution for the rotations of the ammonium ions around a C_2-axis (broader Lorentzian function) and another contribution for the motions of the phenyl rings (narrower Lorentzian function). The background was fitted by a straight line. The motions of the phenyl rings are described as librations, in the upper figure (a) with a jump distance of 0.2Å and in the lower figure (b) with an jump distance of 0.3Å. The corresponding elastic contributions are shown in the inserts.*

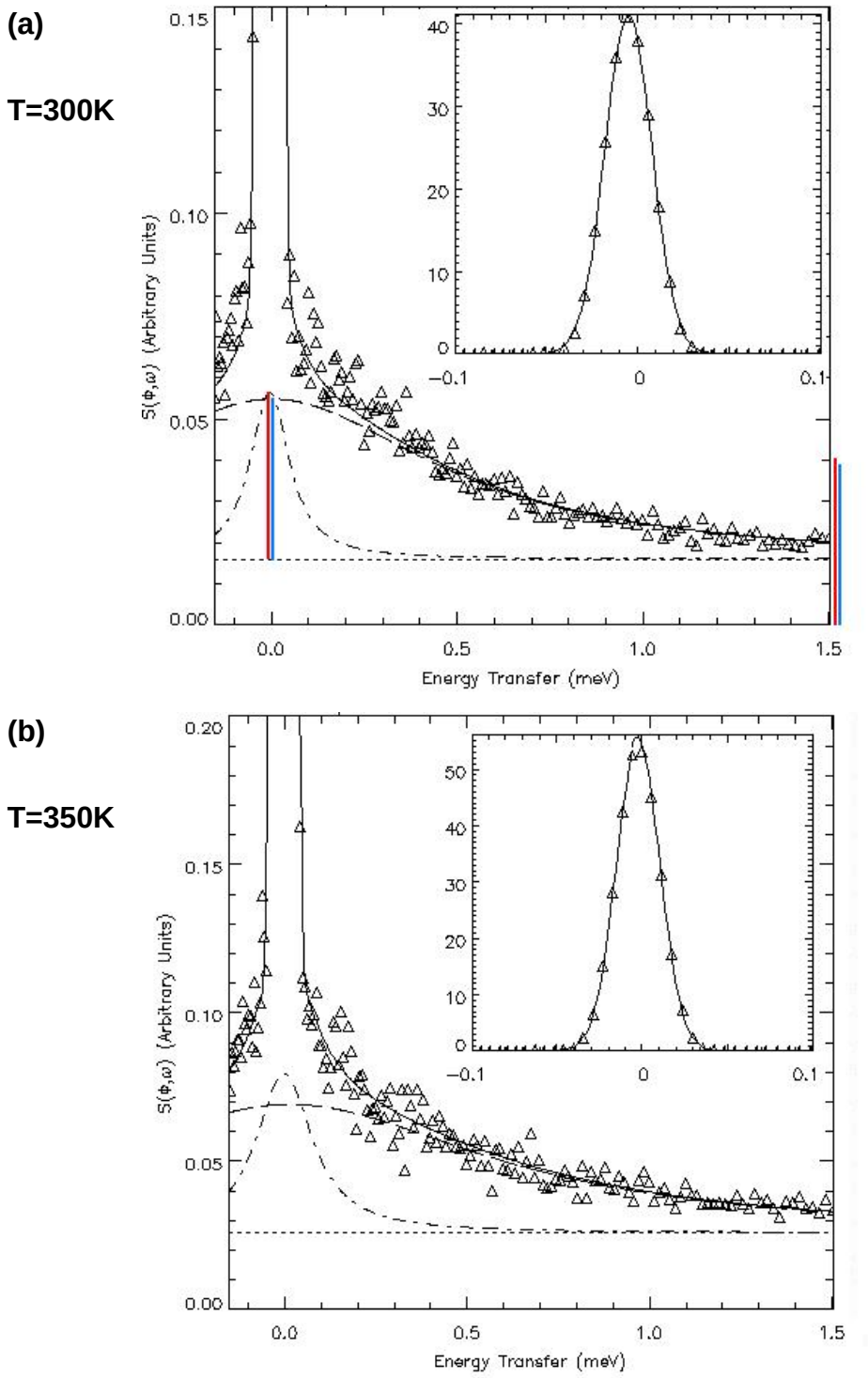

Fig 4-19 *QENS spectra of ATPB (triangles) reproduced by a model including a contribution for the rotations of the ammonium ions around a C_2-axis (broader Lorentzian function) and another contribution for the motions of the phenyl rings (narrower Lorentzian function). The background was fitted by a straight line. The motions of the phenyl rings are described as librations, (a) at T=300K with a jump distance of 0.25Å and (b) T=350K with a jump distance of 0.3Å. The corresponding elastic contributions are shown in the inserts. The data was measured at $\Delta E=32\mu eV$ and at average Q value of 1.3Å^{-1}.*

Due to the different number of particles and the different scattering cross sections of ATPB and ATPB-d, the scattering of ATPB-d has about 70% of the intensity of ATPB (see ***section 4.1***). This holds for the complete molecular unit, but it is also possible to define the ratio of scattering probabilities for individual groups of ATPB-d and ATPB samples. For the mobile particles of the ammonium groups this ratio is

$$\frac{P_{sc}^{ATPB-d}(77\%\ \ deuterated\ \ ammonium)}{P_{sc}^{ATPB}(ammonium)} = 0.206 \qquad \textbf{Eq 4-42}$$

For the phenyl groups the different numbers of the particles in both samples gives this ratio

$$\frac{P_{sc}^{ATPB-d}(mobile\ \ particles\ \ in\ \ phenyl\ \ rings)}{P_{sc}^{ATPB}(mobile\ \ particles\ \ in\ \ phenyl\ \ rings)} = \frac{m^{ATPB-d}}{M^{ATPB-d}} \cdot \frac{M^{ATPB}}{m^{ATPB}} = 0.68 \qquad \textbf{Eq 4-43}$$

The detailed calculations are given in the ***Appendix*** E. These intensity ratios assign the QE components either to the ammonium ions or to the phenyl rings.

Fig 4-18 (b) and ***Fig 4-19 (a)*** allow for a comparison of the relative intensities of the QE components. In both cases the widths of the corresponding QE components are equal, and therefore the ratio of their heights equals to the ratio of their intensities. In both figures, the red line corresponds to the height of the narrow QE component (having HWHM=0.06meV) and the blue line corresponds to the height of the broader component (having HWHM=0.54meV). Reading the heights of these components we get an intensity ratio of

$$I_{QE\ narrow}^{ATPB-d} \Big/ I_{QE\ narrow}^{ATPB} = \frac{0.027}{0.04} = 0.675 \qquad \textbf{Eq 4-44}$$

for the narrower component and

$I_{QE\ broad}^{ATPB-d} \Big/ I_{QE\ nbroad}^{ATPB} = \frac{0.008}{0.039} = 0.205$	**Eq 4-45**

for the broader component.

According to these intensity ratios the narrow QE component is due to the motion of the phenyl rings and the broader one is due to the motion of the ammonium ions.

4.2.2.3 Summary of the motions of the phenyl rings

The analysis of the QENS spectra of ATPB-d revealed an important result: it was proven that the narrow QE component originates from the reorientation of the phenyl rings. This result has not been reported in literature before, and it sheds new light on the picture of the aromatic H-bonds. The reorientation angle and the jump rate of the librations of the phenyl rings increase with increasing temperature. At room temperature

- a reorientation angle of α=7°±2 and
- a correlation time of 150±50ps

were found.

Within the framework of this study, it was not possible to determine the jump rate of the phenyl rings accurately, since the librations only cause a very weak and narrow QE component, which cannot easily be separated from the experimental resolution. The accuracy of the determined jump rates is rather poor and therefore it is not possible to define the activation energy for this motion.

4.3 Inelastic bands

4.3.1 Interpretation of the inelastic bands at room temperature

Five inelastic peaks have been observed in the energy gain side between 2meV and 15meV. The intensities but not the frequencies of these peaks vary with Q. ***Fig 4-20*** shows the INS spectrum of ATPB and ATPB-d obtained at NEAT measurements at T=300K, ΔE=30μeV, Q=1.05Å^{-1}. The QE contributions were subtracted from the INS spectra, as they give a small contribution at the lower end of the energy transfer scale shown here (up to about 5meV). The ATPB-d spectrum has been corrected to correspond to the number of the moles of the ATPB sample (e.g. multiplied by a factor $n_{ATPB}/n_{ATPB\text{-}d}$=1.492, where $n_{ATPB\text{-}d}$ and n_{ATPB} are the number of moles in the ATPB-d and in the ATPB sample).

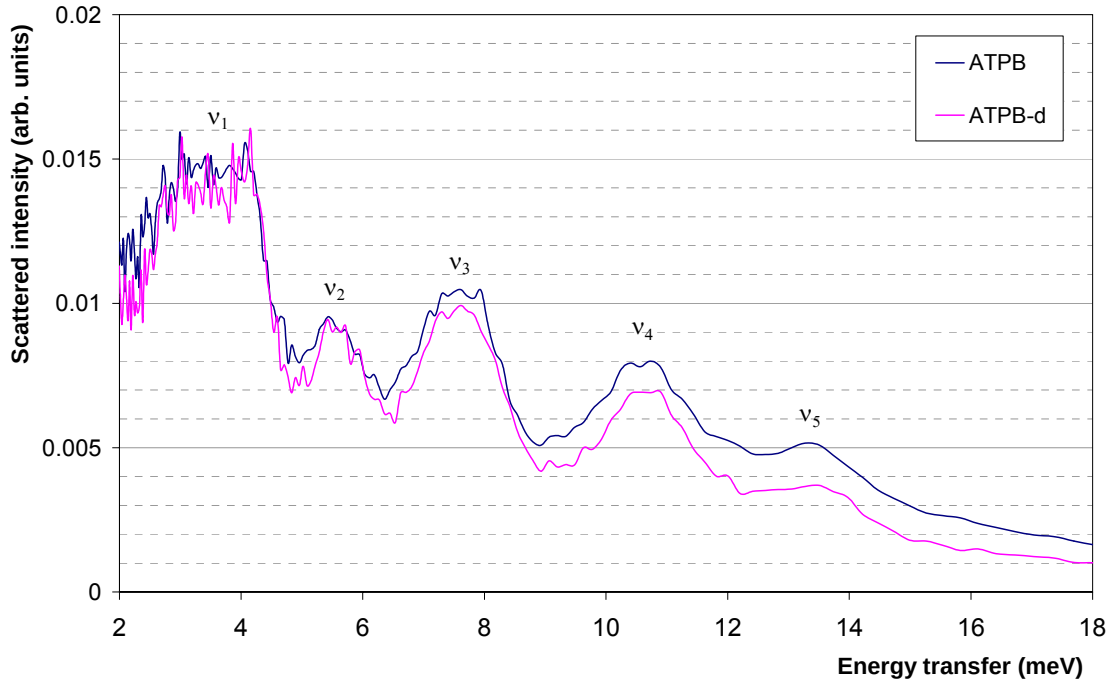

Fig 4-20 *INS spectra for ATPB (blue solid line) and the ATPB-d (pink solid line) measured at T=300K, ΔE=30μeV, Q=1.05Å^{-1}.*

The experimentally observed intensity ratios of ATPB-d and ATPB, for different modes are given in ***Table 6***. The comparison of these ratios with the ratios of the scattering cross sections enables us to assign each mode to either ammonium, phenyl or to the entire molecule. In ***Table 5*** the total scattering cross sections of these components in ATPB and in ATPB-d are shown and the ratios are calculated.

INS Peak	Peak Frequency (meV)	Intensity ratio $\frac{I_{ATPB-d}}{I_{ATPB}}$
ν_1	3.6±0.6	~0.95
ν_2	5.6±0.2	~1
ν_3	7.7±0.2	~0.95
ν_4	10.7±0.2	~0.89
ν_5	13.4±0.2	~0.71

Table 6 *Intensity ratios of ATPB-d and ATPB separately for each single inelastic mode.*

	σ_{tot}^{ATPB}	σ_{tot}^{ATPB-d}	$\frac{\sigma_{tot}^{ATPB-d}}{\sigma_{tot}^{ATPB}}$
Whole molecule	2110 barns	1882 barns	0.89
Ammonium	338 barns	110 barns	0.33
Phenyl	1772 barns	1772 barns	1

Table 5 *Total scattering cross sections. The ratios were either considered for the entire molecule or the ammonium ion or the phenyl groups in ATPB-d and ATPB.*

This comparison shows that none of the inelastic peaks in this energy region result exclusively from the ammonium ions. The peak ν_2 is assigned here to the phenyl rings in agreement with a previous study of Roberts et al. [41], they did not observe this band in phenyl deuterated ATPB (see ***Fig 4-21***). Roberts et al. interpreted their observation of peak ν_4 and ν_5 to result from ammonium, as they did not observe a significant intensity change comparing non-deuterated and phenyl-deuterated ATPB. Their observation showed instead a frequency shift of ν_4 and ν_5, which was interpreted as a result of the cation-anion coupling. For the ammonium deuterated ATPB, we did not observe a significant intensity change of ν_4 and ν_5, as is expected for the ammonium ion modes. The slight, but noteworthy, intensity changes of these modes moreover assigns them to the

entire molecule. The frequency shift observed by Roberts et al. can now be understood as a result of the larger mass (increase by twenty protons) of the phenyl deuterated molecule. The mass of our ammonium deuterated ATPB increased only by 3 protons, and thus it is too small to observe a frequency shift at our experimental resolution. The modes ν_1 and ν_3 are also related to the entire molecule, as they show a small intensity decrease for ammonium deuterated ATPB at room temperature. At lower temperatures these modes behave differently, an observation which will be discussed more detailed in ***section 4.3.2.*** Roberts et al. interpreted these modes as librations of the ammonium ions or alternatively as free rotations, at low temperatures $T \leq 80K$. Our result for the high temperature spectra is clearly in contradiction with that of Roberts at al. Anyhow we can find an agreement of our interpretation with another study of Jayasooriya et al. [45], where they have measured several tetraphenyl compounds, like $C(C_6H_5)_4$, using the NEAT spectrometer and they found five torsional modes of phenyl rings at similar energy transfer values as the inelastic modes observed in this work. This shows that the phynyl rings contribute strongly to the inelastic spectra and that the ammonium ion librations are strongly coupled with the torsional vibrations of the phenyl rings.

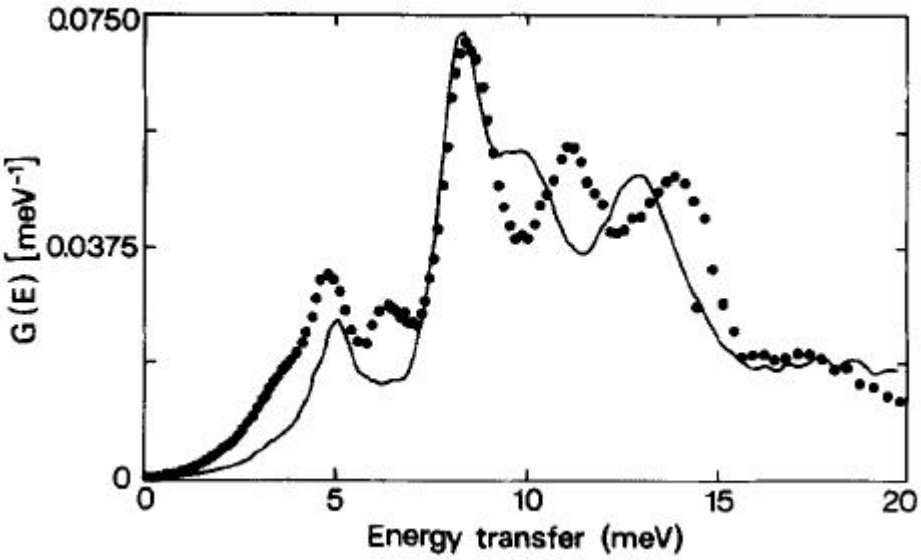

Fig 4-21 *INS spectrum of the ATPB (dotted line) and the phenyl deuterated ATPB (solid line) measured at the IN6 spectrometer at ILL at an energy resolution of about 500μeV, a wave-vector of about 2Å^{-1} and T=80K [41].*

4.3.2 Temperature development of the inelastic modes

For a qualitative explanation of the inelastic modes, a model involving six damped harmonic oscillators (DHO) [46], [47] was used and combined with a phenomenological quasielastic contribution. (The inelastic mode, denoted with ν_1 in the previous section, in fact contains two neighbouring peaks, both of them now explained as a DHO.) The scattering function for this model is

$$S(Q,\omega) = F \cdot e^{-Q^2\langle u^2\rangle} \cdot e^{-\frac{\hbar\omega}{kT}} \cdot \left\{ A_0(Q)\delta(\omega) + [1 - A_0(Q)]\frac{1}{\pi}\frac{\Delta(Q)}{\omega^2 + \Delta(Q)^2} + \frac{\omega}{1 - e^{\frac{-\hbar\omega}{kT}}} \cdot \left[e^{\langle u^2\rangle_{DHO} Q^2} - 1 \right] \cdot \sum_{j=1}^{6} \frac{D_j f_j^2}{\left(f_j^2 - \omega^2\right)^2 + \omega^2 D_j^2} \right\} \otimes R(Q,\omega)$$

Eq 4-46

where D_j are the damping factors, f_j the oscillator frequencies and $R(Q,\omega)$ is the energy transfer dependent resolution function given in the reference [33]. The energy transfer dependent evolution of the peak width is shown in ***Fig 4-26*** at used energy resolutions 32μeV and 98μeV. The inelastic scattering contributions of the vibrational motions of all components are taken into account by the global and DHO Debye-Waller factors, $e^{-Q^2\langle u^2\rangle}$ and $e^{-\langle u^2\rangle_{DHO} Q^2}$ where $\langle u^2\rangle$ and $\langle u^2\rangle_{DHO}$ are the average mean square displacements of the whole assemble of vibrational motions and the DHO, respectively.

The damping lowers the oscillator energy and broadens the line shape towards the quasielastic region. Roughly it can be stated that if the damping factor is higher than the oscillator energy it appears as a broad quasielastic contribution. The behaviour of a damped inelastic mode at ±6meV is illustrated in ***Fig 4-23***. During the fitting procedure of the expression of the six DHO, the damping factors were kept smaller than the corresponding oscillator energy, in order to avoid undesired shifts of these components to the quasielastic region, which would occur due to the correlation between diffusive and damping effects in the scattering function.

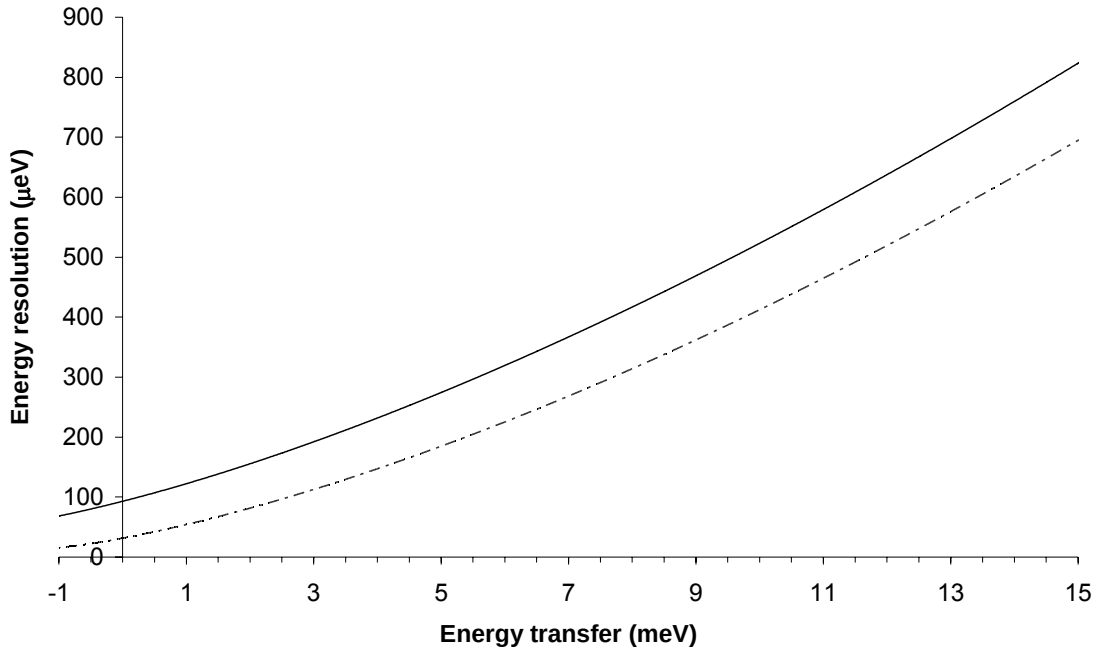

Fig 4-22 *Resolution function for 32μeV and 98μeV at the NEAT.*

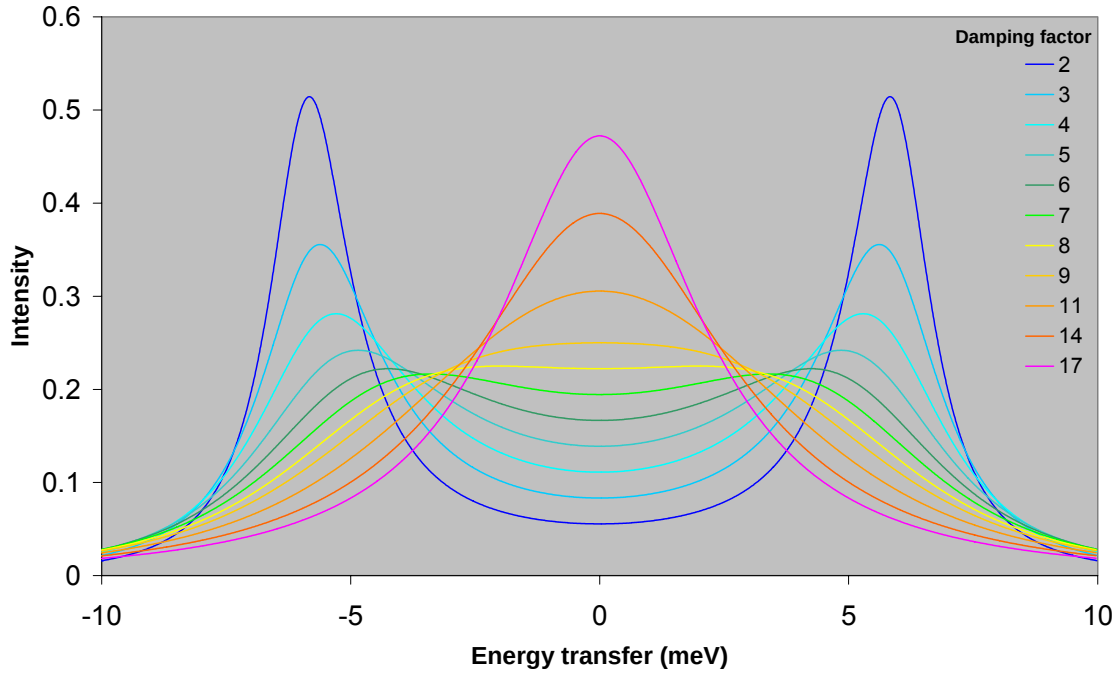

Fig 4-23 *Behaviour of a damped inelastic mode at ±6meV, as a function of damping.*

The DHO-model has been used to reproduce the experimental data over the entire temperature range measured. In ***Fig 4-24*** two selected temperatures are shown, (a) T=300K and (b) T=20K. The experimental data are well reproduced at temperatures above 100K. For temperatures below 100K, this model could not explain the experimentally obtained data, as the intensities of some modes decrease (ν_2 ,ν_4 & ν_5) while the intensities of others do not change or even increase (ν_1 & ν_3).

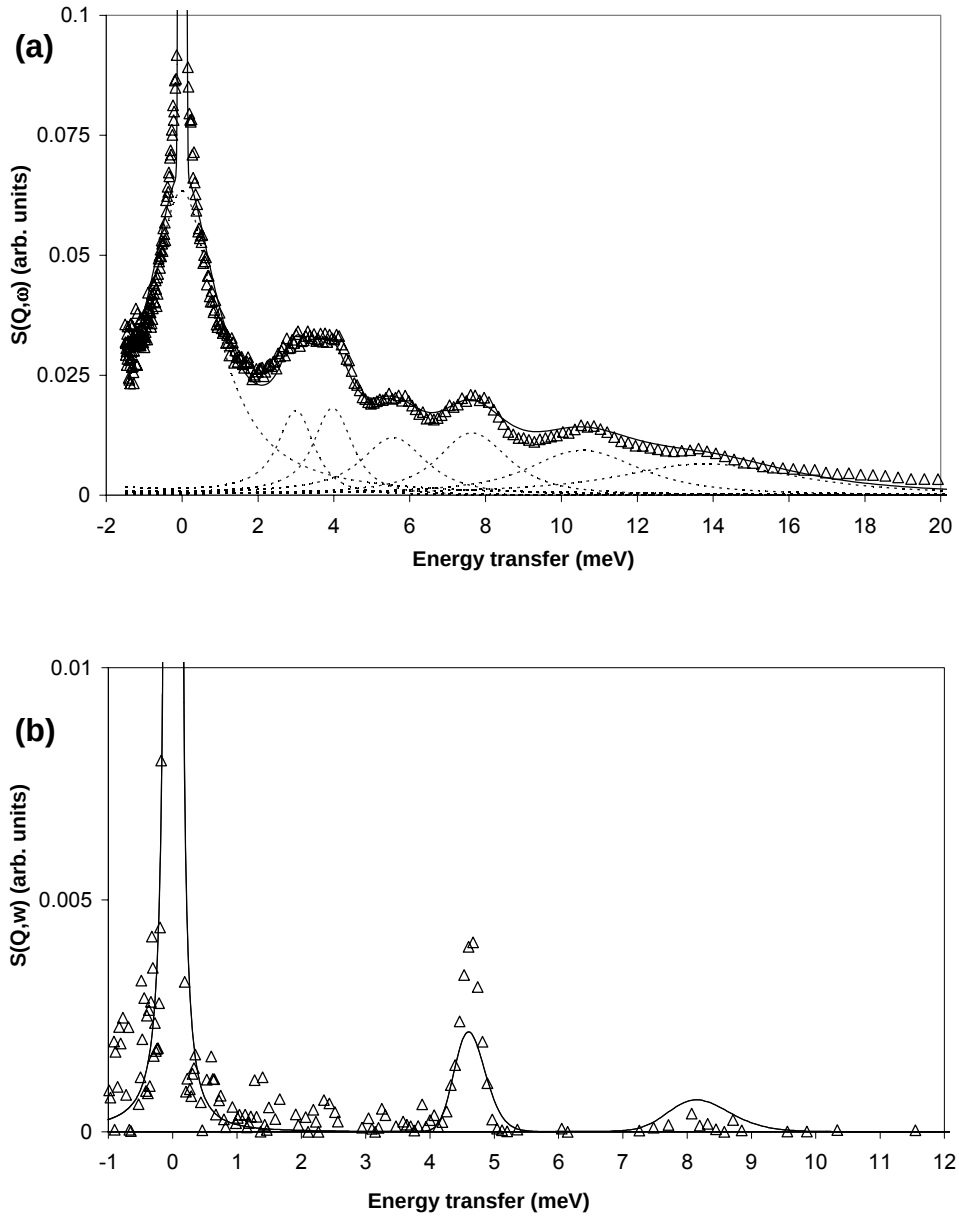

Fig 4-24 *The DHO-model fitted (solid black line) to the experimental data (triangles), at ΔE=98μeV, Q=2Å^{-1}, and (a)T=300K and (b)T=20K.Each contribution is shown with as a dashed line.*

The temperature development of the inelastic frequencies is shown in ***Fig 4-25.*** Above 100K the behaviour of the inelastic modes is normal, i.e. the modes slightly soften with increasing temperatures. On cooling some of the modes disappear (ν_2 and ν_4 below 50K and ν_5 below 100K), which can be explained by thermal activation, since we work in the energy gain side. However, ν_1 and ν_3 show an anomalous behaviour at low temperatures (ν_1 below 50K and ν_3 below 100K) slightly hardening at increasing temperatures. Below 100K the intensities of these peaks also show a rather anomalous behaviour (see ***Fig 4-26***). Let us for example consider the case of 100K compared with 50K. While the other modes are hardly visible at 50K, the intensity of ν_1 does not change and the intensity of ν_3 decreases only slightly and not as much as the other modes. ν_1 and ν_3 still exist at 20K. The classical description of thermal activation has no explanation for this phenomenon.

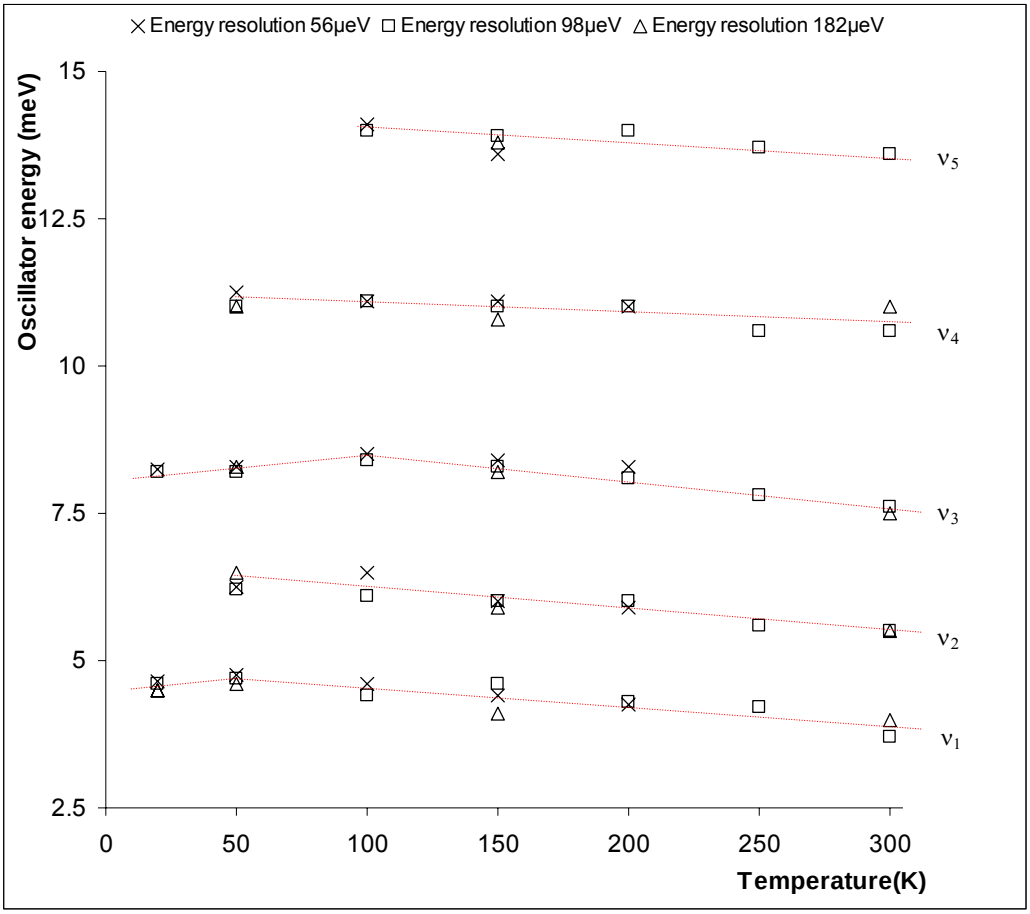

Fig 4-25 *Thermal behaviour of the IN frequencies obtained at NEAT measurement at three energy resolutions. The red lines are guides to the eye.*

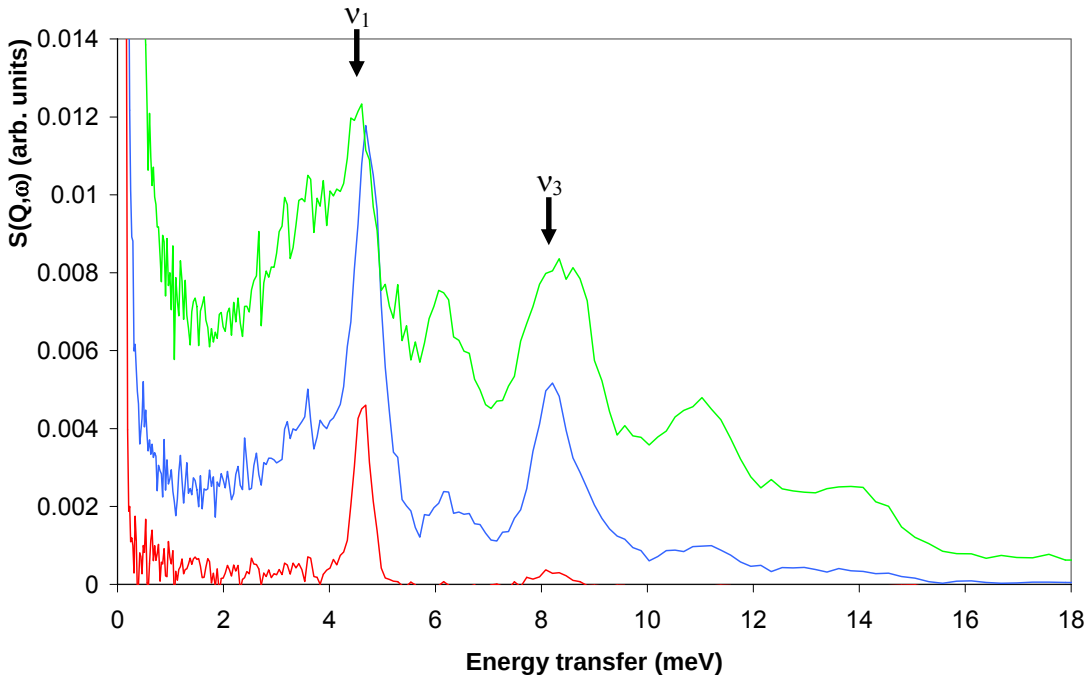

Fig 4-26 *Temperature dependence of the IN intensities at ΔE=98μeV, Q=2.1Å^{-1} and three different temperatures, T=100K (green line), T=50K (blue line) and T=20K (red line).*

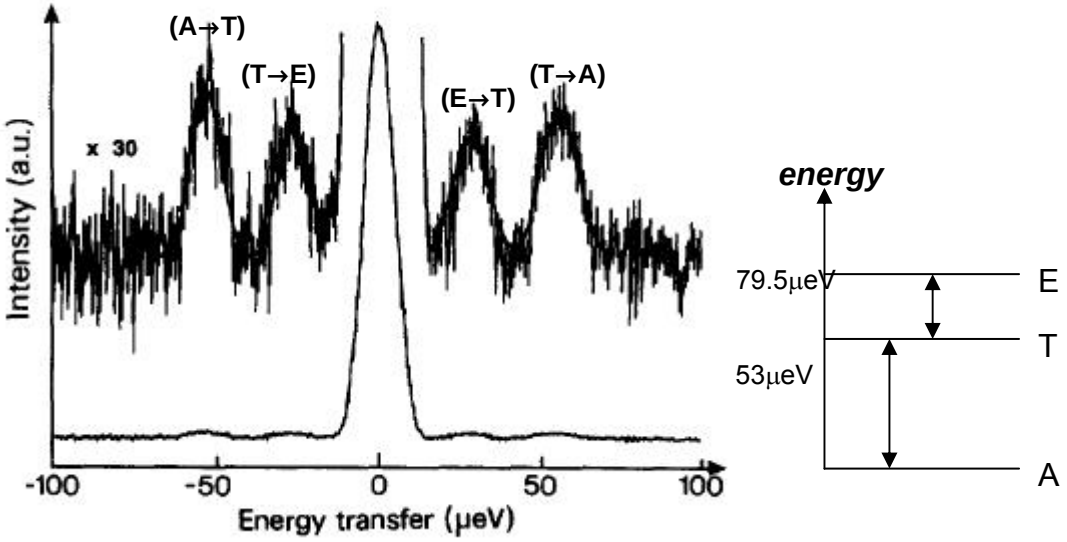

Fig 4-27 *INS rotational tunneling spectrum of the ammonium ion in phenyl deuterated ATPB at 1.5K recorded at the IN5 spectrometer (ILL) at λ=12Å, an energy resolution of 10μeV and at Q=0.8Å^{-1} [41].The upper trace is magnified 30 times. The energy level scheme of the NH_4 librational ground state is shown on the side. The inelastic lines are attributed to the indicated transitions.*

In the temperature range of 100K to 50K the anomalous behaviour of the inelastic modes ν_1 and ν_3 is observed while the quasielastic component due to the ammonium rotation around the C2 axis disappears (see ***section 4.2***). This observation can be explained as a continuous transition from the quantum–mechanical rotation of the ammonium ion at low temperatures to classical diffusive rotational motion at high temperatures. Several examples of this type of behaviour in ammonium salts have been reported previously, e.g. [48], [49], [50], [51] & [52].

In [41], Roberts et al. reported tunneling splitting of the ammonium ion in ATPB at 1.5K, see ***Fig 4-27***. The energy level schemes for rotational ground state splitting of a tetrahedral molecule at sites of different symmetry are well known [53], [54] & [55]. At transitions A⇔T the energy transfer is twice as high as at transitions T⇔E, and the relative intensities of these transitions are 5:4, respectively [56]. Therefore the bands at ±53μeV result from A⇔T transitions and the bands at ±26.5μeV from T⇔E transitions of ammonium ions at the cubic site. Roberts et al. [41], [57] also discussed the inelastic modes we referred to ν_1 and ν_3 and they provided two alternative interpretations for these modes. The first possibility is that ν_1 and ν_3 are librations of two inequivalent ammonium ions, one of which occupies a cubic and the other one a tetrahedral site. The second possible interpretation is the free-rotor model according to which the modes ν_1 and ν_3 result from 0-2 and 0-3 transitions, respectively. None of these two interpretations conclusively explains the INS spectra measured. The 0-1 transition expected according to the free-rotor model at 1.5meV was not found in the INS spectra. A value of 12.4meV was calculated for the ammonium libration in the tetrahedral site symmetry [41] using the tunneling frequencies. It is questionable if ν_3 at 8.2meV can be interpreted as a libration of the ammonium ion at the tetrahedral site. In a crystalline field with a symmetry lower than T_d, the librational frequency of the ammonium ion splits [58], and thus the ammonium libration at the cubic site cannot be explained by ν_1 only .

According to [59] and [60] the ammonium ions in ATPB are in a D_{2d} site with very little distortion from the T_d site. The rotational excitations of the ammonium ions in other compounds of the cubic site have been studied previously, e.g. [48], [50], [56] & [61] and the tunneling energies are found to be connected with excited librational states via the so-called random average model [62], [63]

$$\omega_0(T) = \frac{\sum_{n=0}^{N} \omega_n(T=0) e^{-E_n/kT}}{\sum_{n=0}^{N} e^{-E_n/kT}} \qquad \textit{Eq 4-47}$$

where ω_n is the tunnel frequency of the nth librational state and E_n is its energy. In this model the temperature dependence is explained in terms of a dynamical averaging between the two frequencies, the tunnel splitting of the ground state and the first excited state. Prager et al. [48] measured the temperature dependence of ammonium tunneling in $(NH_4)_2SnCl_6$ and fitted the experimental observed data with the random average model and confirm that the observed inelastic mode at 13.4meV is the first and the one at 30meV the second excited librational state. In their measurement the tunneling lines shifted to a lower energy transfer with increasing temperatures. The relation $E_{A\Leftrightarrow T}/E_{T\Leftrightarrow E}\approx 2$ remains valid at all temperatures, but the tunneling lines do not broaden with increasing temperature, as some theories e.g. [62] suggest. The librational excited states get more intense at low temperatures when tunneling is observed.

A comparison of our observation and the work of Prager et al. [48] indicates that the inelastic modes ν_1 (4.3meV) and ν_3 (8.2meV) are probably the first and the second excited librational state. As expected for the librational excitations ν_1 and ν_3 are considerably stronger than the thermally activated phonons at low temperatures. According to [58], the librational frequency of tetrahedral molecule splits at the cubic site, which is also in agreement with this interpretation. Because the temperature dependence of the ammonium tunneling in ATPB has not been measured yet and the existing theories cannot explain this phenomenon, we cannot perform fits using ***Eq 4-47*** like Prager et al. [48]. However, we have performed calculation based on the same theory

(***Eq 4-47***) to estimate the temperature dependence of the tunneling frequency $\omega_0(T) = E_{A \Leftrightarrow T}(T)$ for two different interpretations:

(a) N=2: The experimentally determined values ν_1 and ν_3 were chosen to be the librational energies of the two excited states and the corresponding tunneling frequencies were the observed values 53μeV and 26.5μeV, respectively.
(b) N=1: The experimentally determined value ν_3 was chosen to be the first excited librational state and ν_1 was the corresponding tunneling frequency.

In ***Fig 4-28*** the calculated functions of $\omega_0(T)$ are shown for both cases. Interpretation (b) shows that the tunneling frequency rapidly decreases above 10K and disappears at 22K. Interpretation (a) shows that the tunneling frequency slowly decreases at temperatures above 10K. This means that the quantum effects get excited slowly at decreasing temperatures below 100K, which is in agreement with our observation from the INS spectra. Therefore interpretation (a) is more favorable. We can close this discussion with the conclusion, that the observed IN mode at 4.3meV (ν_1) is the first excited librational state and the observed IN mode at 8.2meV (ν_3) is the second excited librational state of the ammonium ion.

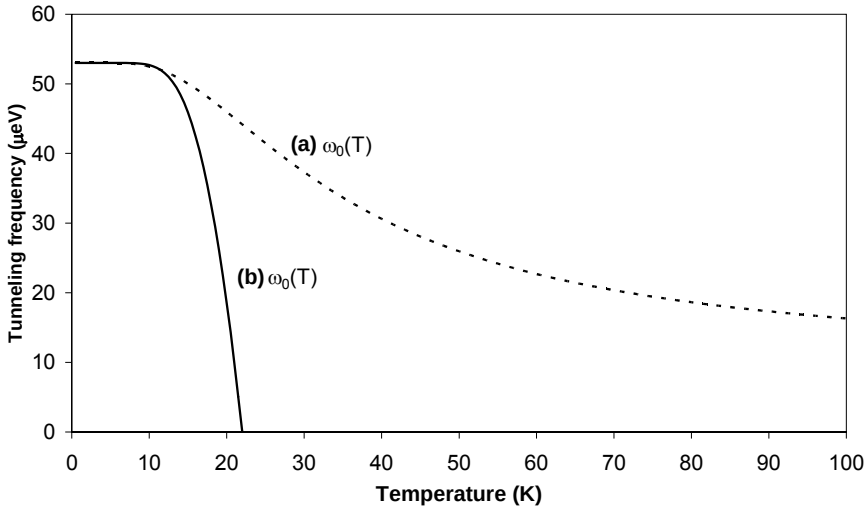

Fig 4-28 *Temperature dependence of tunneling splitting as obtained by analysing the low temperature INS spectra of ATPB with respect to two different interpretations (a)-dashed line and (b)-solid line.*

4.3.3 Conclusions of the inelastic modes

Five inelastic modes at energy gain side between 3meV and 15meV were observed at room temperature. These modes result from strongly coupled librational motions of ammonium ions and torsional vibrations of phenyl rings. When cooling down below 100K, the torsional vibrations of the phenyl rings are weakening due to thermal activation and vanish below 50K. Two inelastic modes remain rather intense even at the lowest measured temperature (20K), where thermal activation can be excluded as explanation. These modes are explained in this work as excited librational states of those ammonium ions that perform rotational tunneling [41].

5 CONCLUSIONS AND DISCUSSION

In the framework of this study the dynamics of the ammonium ions and the phenyl rings, creating an aromatic H-bonding in the ammonium tetraphenyl-borate, were studied in a comprehensive way with incoherent neutron scattering. The measured quasielastic and inelastic neutron scattering spectra were explained over a broad temperature range ($20 \leq T \leq 350K$). A continuous transition from quantum–mechanical rotations of the ammonium ions, at low temperatures, to classical diffusive rotational motion at high temperatures was discovered. Furthermore, local diffusive motions of reorientation of the phenyl rings were found to contribute to the measured quasielastic incoherent neutron scattering spectra at temperatures above 200K.

In a temperature range of $67K \leq T \leq 350K$ the quasielastic incoherent neutron scattering spectra showed classical diffusive rotations of the ammonium ions around the C_2/C_3 axis. The correlation time for this motion varies from 12.5ps at T=350K to 1253ps at T=67K and the activation energy for these rotations was determined to be 3.2kJ/mol. This result shows that the ammonium ions have to overcome an exceptionally low barrier to rotate. Our results regarding the ammonium ion rotations around the C_2/C_3 axis in ammonium tetraphenylborate are partly consistent with a previous study of Lucazeau et al. [60], who found an activation energy of 2.9kJ/mol for this dynamical process. But, our analysis is more precise, as we used a higher experimental energy resolution and a more accurate model which included also the contribution due to the motions of the phenyl rings to reproduce the experimental spectra.

At low temperatures (below 67K) quantum–mechanical rotations of the ammonium ions were discovered. Tunneling of the ammonium ions has already been reported [41]. We could not observe this tunneling with the used experimental resolutions. Instead, a narrow quasielastic component at temperatures below 67K, which could not be explained as a classical diffusive rotation, was seen. We allege that this component is indicative of the tunneling. Additionally, analysing the measured inelastic neutron scattering spectra, we found excited librational states of ammonium at 4.3meV and 8.2meV, which are linked to the tunneling frequencies via the so-called random average model. Future investigations of this subject should involve the study of the temperature

dependence of ammonium tunneling with a back-scattering spectrometer (e.g. IN10 or IN16 at ILL or IRIS at ISIS). This could further a better understanding of the transition from quantum–mechanical rotations to classical diffusive rotations.

Another interesting result of the work presented here concerns the motions of the phenyl rings at temperatures above 200K. On the time scale of our QENS experiments, damped librational motions of the phenyl rings were observed. We have described these motions using a reorientational jump-diffusion model to reproduce the quasielastic neutron scattering spectra. The reorientation angle and the jump rate of the librations of the phenyl rings increase with increasing temperatures. At room temperature the librations of the phenyl rings were found to have a reorientation angle of α=7°±2 and a correlation time of 150±50ps. This result sheds new light on the phenomenon of the aromatic H-bonding.

Contrary to previous studies the dynamics of the phenyl rings are discussed in the framework of aromatic hydrogen bonding here. This new approach shows that aromatic hydrogen bonds are extremely flexible and allow for reorientation of both, the donor and the acceptor. This is an important result which might have important implications in the field of biology.

Based on the results presented here, further studies are required for a precise explanation of the dynamics of the phenyl rings. For this purpose ammonium deuterated ATPB should be investigated with a backscattering spectrometer (e.g. IN10 or IN16 at the ILL or IRIS at the ISIS) to study the temperature dependence of the reorientations of the phenyl rings. These investigations would also provide an answer to the question whether the phenyl rings flips also occur.

Appendix A

Instrument data of NEAT:

Neutron guide:	NL 2 (upper part)
Guide cross-section:	30 x 55 mm2
Double-trumpet cross-section at chopper (1,2):	15 x 55 mm2
Chopper windows:	15 x 60 mm2, 30 x 60 mm2 and 60 x 60 mm2
Distance chopper (1,2) chopper (6,7):	11970 mm
Chopper speed range:	750 rpm, 1000 rpm to 20000 rpm
Incident wavelength range for monochromatic measurements:	0.18 nm <= λ <= 1.9 nm;
White beam spectrum:	0.1 <= λ <= 6.0 nm
Elastic energy resolution (FWHM) at SD:	6 μeV <= ΔE <= 5400 μeV
Elastic energy resolution (FWHM) at MD:	2 μeV <= ΔE <= 3800 μeV
Flux at the sample for λ = 0.6nm (example):	2 · 104 n/cm2s for the following elastic energy resolutions: ΔE = 250 μeV (FWHM) for SD ΔE = 130 μeV (FWHM) for MD
Range of scattering angles for SD:	13.35° <= Φ <= 136.65°
Angular range accessible to MD elements:	1° <= Φ <= 137°
Distance sample-SD:	2500 mm
Distance sample-MD:	4080 mm <= L <= 7300 mm
Sample environment:	maxi-cryostat 1.5 K <= T <= 300 K (100 mm diam.) cryofurnace 1.5 K <= T <= 570 K (80 mm diam.) HT-furnace 300 K <= T <= 1270 K (70 mm diam.)

Appendix B

Data processing:

- **Correction for detector efficiency**

The double differential cross-section is the measured quantity. The connection between theory and the experiments can be described as

$$\frac{\partial^2\sigma}{\partial\Omega\partial E_1} = \frac{C}{\Phi N\Delta\Omega\Delta t\eta(E_1)}$$	**Eq A-1**

C on the right hand side of the equation represents the count rate of the scattered neutrons counted at a detector with an efficiency $\eta(E_1)$, placed on a solid angle $\Delta\Omega$ between the times t and Δt, from the incident neutron beam with a flux density Φ. The flux density is not exactly known from the measurements, instead a relative density can be used, as a tiny portion of the monochromatic incident neutron beam is detected at the monitor.

The detector efficiency is calibrated by using a vanadium spectrum as an indicator. The detector efficiency $\eta(E_1)$ depends on the energy of the scattered neutrons as a consequence of the energy dependence of the neutron absorption. Therefore the detector efficiency must be corrected for the different detected neutron energies detected. Vanadium scattering is known to be purely incoherent, thus it is independent of the scattering angle. A measurement of a vanadium plate of the same geometry as the sample was therefore used for this purpose.

- **Sample absorption correction**

If the sample contains N molecular units per unit volume with a cross section σ, the count rate is attenuated by a factor

$$A = \frac{1}{V}e^{-N\sigma(p+q)dV}$$	**Eq A-2**

where $p+q$ is the path length of a scattered neutron through the sample of volume V, i.e. p is the distance that the incident neutron travels from the surface of the sample to the point where the scattering happens and q is the path length from this point to the surface of the sample. The attenuation depends on the sample geometry, how the sample is placed in the neutron beam and finally on the scattering angle. Detailed expressions for sample attenuation at different experimental conditions can be found in literature e.g. [64].

- **Background subtraction**

To isolate neutron scattering which results only from the sample, sample environment effects (including e.g. sample container, cryostat, furnace and exchange gas) must be subtracted from the spectra. For this purpose the empty sample container is measured on similar conditions as the sample to obtain identical effects.

- **Conversion to energy scale and interpolation to constant Q**

The counted neutrons are recorded and histogrammed with respect to their time-of-flight. The neutrons that arrive to the detectors between times t_j and Δt are grouped in the histogram j. The double differential cross-section for time-of-flight measurement can be given as follows

$$I(\phi,t)=\frac{\partial^2\sigma}{\partial\Omega\partial t}\Delta\Omega\Delta t\Phi\eta$$	**Eq A-3**

It describes the probability that a neutron is scattered into a group of detector defined by a mean angle ϕ, between the times t and δt. $\Delta\Omega$ is the solid angle subtended by the group, Δt is the width of the time window, Φ is the flux density of the neutrons incident on the sample and η is the detector efficiency.

Overall scale factors that do not depend on time or neutron energies can be left out in the conversion calculations, in order to obtain a simpler formalism. The double differential cross-sections taken with respect to time are connected to double differential cross-sections with respect to energy

$$\left(\frac{\partial^2\sigma}{\partial\Omega\partial\omega}\right) \propto \left(\frac{\partial^2\sigma}{\partial\Omega\partial E_1}\right)\left(\frac{dE_1}{dt}\right) \propto \left(\frac{\partial^2\sigma}{\partial\Omega\partial t}\right)t^3$$	**Eq A-4**

where E_1 is the final energy of the scattered neutron.

The scattering function can now be given as

$$S(\phi,\omega) \propto \frac{1}{k_1}\left(\frac{\partial^2\sigma}{\partial\Omega\partial t}\right)t^3 \propto \frac{I(\phi,t)t^4}{\eta(\omega)\Phi}$$	**Eq A-5**

Because the neutron scattering data are collected as a function of the scattering angle ϕ, the corresponding momentum transfer values will be calculated. For the elastic scattering the magnitude of the wave vector is conserved and the momentum transfer is given as

$$\vec{Q} = \frac{4\pi\sin\left(\phi/2\right)}{\lambda}$$	**Eq A-6**

where λ is the wavelength of the incident neutrons. For the inelastic scattering the momentum transfer depends on both, the direction and the magnitude of the incident and scattered wave vectors. Therefore the connection between the momentum transfer $\vec{Q}$ and the scattering angle ϕ for inelastic scattering is given as

$$Q^2 = k_1^2 + k_0^2 - 2k_1k_0\cos\phi$$	**Eq A-7**

Appendix C

Calculations to determine the deuteration percentage of ATPB-d:

In literature [24] the absorption values are normally given for a wave length of 1.794Å. The absorption values in the last column have been corrected for the used wavelength of 8Å.

Atom	**Atomic mass** M [g/mol]	**Total scattering cross section** σ_{sc} [$cm^{2}\cdot10^{-24}$]	**Absorption cross section for 1.794Å** σ_{abs} [$cm^{2}\cdot10^{-24}$]	**Absorption cross section for 8Å** σ_{abs} [$cm^{2}\cdot10^{-24}$]
H	1.008	82.03	0.3326	1.4832
D	2.0155	7.64	0.000519	0.0156
C	12.01	5.559	0.00353	0.0023
N	14.01	11.51	1.9	8.4727
B	10.81	5.24	767	3420.290

The scattering probability of ATPB [NH_4 $(C_6H_5)_4B$] is

$$P_{sc}^{ATPB} = 1 - (P_{tr}^{ATPB} + P_{abs}^{ATPB})$$

$$= exp\left[-\frac{\sigma_{abs}^{ATPB} \cdot N_A \cdot m^{ATPB}}{M^{ATPB} \cdot \pi \cdot r^2} \right] - exp\left[-\frac{(\sigma_{sc}^{ATPB} + \sigma_{abs}^{ATPB}) \cdot N_A \cdot m^{ATPB}}{M^{ATPB} \cdot \pi \cdot r^2} \right]$$

$$= exp\left[-\frac{(24 \cdot \sigma_{abs}^{H} + 24 \cdot \sigma_{abs}^{C} + \sigma_{abs}^{N} + \sigma_{abs}^{B}) \cdot N_A \cdot m^{ATPB}}{(24 \cdot M^{H} + 24 \cdot M^{C} + M_s^{N} + M^{B}) \cdot \pi \cdot r^2} \right] -$$

$$exp\left[-\frac{[24 \cdot (\sigma_{abs}^{H} + \sigma_{sc}^{H}) + 24 \cdot (\sigma_{abs}^{C} + \sigma_{sc}^{C}) + \sigma_{abs}^{N} + \sigma_{sc}^{N} + \sigma_{abs}^{B} + \sigma_{sc}^{B}) \cdot N_A \cdot m^{ATPB}}{(24 \cdot M^{H} + 24 \cdot M^{C} + M_s^{N} + M^{B}) \cdot \pi \cdot r^2} \right.$$

$$= 0.091058$$

Eq A-8

The scattering and absorption probabilities of ATPB-d [$N(D_x H_y)_4 (C_6H_5)_4 B$] can be given as functions of x

$$P_{tr}^{ATPB-d}(x) = \exp\left[-\frac{[4x\cdot(\sigma_{sc}^{D}+\sigma_{abs}^{D}-\sigma_{sc}^{H}-\sigma_{abs}^{H})+\sigma_{sc}^{ATPB}+\sigma_{abs}^{ATPB}]\cdot N_A\cdot m^{ATPB-d}}{[4x\cdot(M^{D}-M^{H})+M^{ATPB}]\cdot\pi\cdot r^2}\right]$$	**Eq A-9**
$$P_{abs}^{ATPB-d}(x) = 1-\exp\left[-\frac{[4x\cdot(\sigma_{abs}^{D}-\sigma_{abs}^{H})+\sigma_{abs}^{ATPB}]\cdot N_A\cdot m^{ATPB-d}}{[4x\cdot(M^{D}-M^{H})+M^{ATPB}]\cdot\pi\cdot r^2}\right]$$	**Eq A-10**

Then the scattering probability of ATPB-d as a function of x is

$$P_{sc}^{ATPB-d}(x) = 1-\left(P_{tr}^{ATPB-d}(x)+P_{abs}^{ATPB-d}(x)\right)=$$ $$\exp\left[-\frac{[4x\cdot(\sigma_{abs}^{D}-\sigma_{abs}^{H})+\sigma_{abs}^{ATPB}]\cdot N_A\cdot m^{ATPB-d}}{[4x\cdot(M^{D}-M^{H})+M^{ATPB}]\cdot\pi\cdot r^2}\right]-$$ $$\exp\left[-\frac{[4x\cdot(\sigma_{sc}^{D}+\sigma_{abs}^{D}-\sigma_{sc}^{H}-\sigma_{abs}^{H})+\sigma_{sc}^{ATPB}+\sigma_{abs}^{ATPB}]\cdot N_A\cdot m^{ATPB-d}}{[4x\cdot(M^{D}-M^{H})+M^{ATPB}]\cdot\pi\cdot r^2}\right]$$	**Eq A-11**

Appendix D

The FORTRAN code to calculate the structure factors for the 7-site jump model

Following characters in the FORTRAN code correspond to the variables as given:

- Q is momentum transfer vector
- d is the N-H distance
- mu is the tilt angle called θ
- p is the probability of site S_1

EISF, $A_{07}(Q)$

```
real function sf0(Q,d,mu,p)
real Q
real d
real mu
real p
real t1
real t10
real t11
real t12
real t15
real t20
real t21
real t22
real t23
real t24
real t27
real t3
real t30
real t4
real t46
real t48
real t49
real t5
real t50
real t51
real t53
real t56
real t57
real t58
real t6
real t61
real t66
real t67
real t68
real t78
real t79
real t81
real t85
real t9
  t1 = p**2
  t3 = sqrt(2.E0)
  t4 = t1*Q*t3
  t5 = d**2
  t6 = cos(mu)
  t9 = sqrt(-t5*(-1+t6))
  t10 = t9*t5
  t11 = sqrt(3.E0)
  t12 = t10*t11
  t15 = t6**2
  t20 = Q*t3
  t21 = t20*t9
  t22 = sin(t21)
  t23 = p*t22
```

```
      t24 = t5*t11
      t27 = t24*t15
      t30 = t1*t22
      t46 = -1+t15
      t48 = sqrt(-t5*t46)
      t49 = Q*t48
      t50 = sin(t49)
      t51 = t50*t3
      t53 = t9*t11*t48
      t56 = t51*t9
      t57 = t11*t48
      t58 = t57*p
      t61 = t57*t1
      t66 = sin(Q*t11*t48)
      t67 = t66*t3
      t68 = t9*t48
      t78 = sin(2*t49)
      t79 = t78*t3
      t81 = t79*t9
      t85 = -14*t4*t12+14*t4*t10*t11*t15-
24*t23*t24+24*t23*t27+24*t30*
    #t24-24*t30*t27-
2*t20*t12+2*t21*t27+4*t21*t24*p-
4*t21*t24*p*t15-4*t
    #51*t53+8*t56*t58-4*t56*t61-
4*t67*t68+8*t67*t68*p-4*t67*t68*t1-t79*
    #t53+2*t81*t58-t81*t61
      sf0 = t85*t3*t11/Q/t9/t5/t46/72
      return
     end
```

EISF, $A_{17}(Q)$ corresponding to the HWHM $\Delta_{17} = \kappa_C + \kappa_R$

```
     real function sf1(Q,d,mu,p)
     real Q
     real d
     real mu
     real p
     real t1
     real t11
     real t12
     real t18
     real t2
     real t20
     real t21
     real t22
     real t23
     real t26
     real t3
     real t30
     real t31
     real t36
     real t37
     real t6
     real t7
      t1 = d**2
      t2 = Q*t1
      t3 = sqrt(3.E0)
      t6 = cos(mu)
      t7 = t6**2
      t11 = p*Q
      t12 = t1*t3
      t18 = -1+t7
      t20 = sqrt(-t1*t18)
      t21 = Q*t20
      t22 = sin(t21)
      t23 = t22*t3
      t26 = t20*p
      t30 = sin(2*t21)
      t31 = t30*t3
      t36 = sin(Q*t3*t20)
      t37 = t36*t20
      sf1 = -(2*t2*t3-2*t2*t3*t7-
2*t11*t12+2*t11*t12*t7+2*t23*t20-2*t2
    #3*t26-t31*t20+t31*t26-
2*t37+2*t37*p)*t3/Q/t1/t18/18
      return
     end
```

EISF, $A_{27}(Q)$ corresponding to the HWHM $\Delta_{27} = \kappa_C + 4\kappa_R$

```
      real function sf2(Q,d,mu,p)
      real Q
      real d
      real mu
      real p
      real t1
      real t11
      real t12
      real t18
      real t2
      real t20
      real t21
      real t22
      real t23
      real t26
      real t3
      real t31
      real t32
      real t37
      real t38
      real t6
      real t7

        t1 = d**2
        t2 = Q*t1
        t3 = sqrt(3.E0)
        t6 = cos(mu)
        t7 = t6**2
        t11 = p*Q
        t12 = t1*t3
        t18 = -1+t7
        t20 = sqrt(-t1*t18)
        t21 = Q*t20
        t22 = sin(t21)
        t23 = t22*t3
        t26 = t20*p
        t31 = sin(Q*t3*t20)
        t32 = t31*t20
        t37 = sin(2*t21)
        t38 = t37*t3
        sf2 = -(2*t2*t3-2*t2*t3*t7-
     2*t11*t12+2*t11*t12*t7-4*t23*t20+4*t2
     #3*t26+4*t32-4*t32*p-
     t38*t20+t38*t26)*t3/Q/t1/t18/36
        return
      end
```

EISF, $A_{37}(Q)$ corresponding to the HWHM $\Delta_{37} = \kappa_C + 3\kappa_R$

```
      real function sf3(Q,d,mu,p)
      real Q
      real d
      real mu
      real p
      real t1
      real t11
      real t12
      real t19
      real t2
      real t21
      real t23
      real t24
      real t28
      real t3
      real t30
      real t31
      real t33
      real t35
      real t36
      real t6
      real t7

        t1 = d**2
        t2 = Q*t1
        t3 = sqrt(3.E0)
```

```
      t6 = cos(mu)
      t7 = t6**2
      t11 = p*Q
      t12 = t1*t3
      t19 = -1+t7
      t21 = sqrt(-t1*t19)
      t23 = sin(Q*t3*t21)
      t24 = t23*t21
      t28 = Q*t21
      t30 = sin(2*t28)
      t31 = t30*t3
      t33 = t21*p
      t35 = sin(t28)
      t36 = t35*t3
      sf3 = -(2*t2*t3-2*t2*t3*t7-
2*t11*t12+2*t11*t12*t7-2*t24+2*t24*p+
     #t31*t21-t31*t33-
2*t36*t21+2*t36*t33)*t3/Q/t1/t19/18
       return
      end
```

EISF, $A_{47}(Q)$ corresponding to the HWHM $\Delta_{47} = \kappa_C / p$

```
      real function sf4(Q,d,mu,p)
      real Q
      real d
      real mu
      real p
      real t11
      real t15
      real t17
      real t21
      real t22
      real t28
      real t3
      real t30
      real t31
      real t32
      real t35
      real t4
      real t40
      real t46
      real t5
      real t6
      real t9

       t3 = sqrt(2.E0)
       t4 = Q*t3
       t5 = d**2
       t6 = cos(mu)
       t9 = sqrt(-t5*(-1+t6))
       t11 = sqrt(3.E0)
       t15 = t4*t9
       t17 = t6**2
       t21 = sin(t15)
       t22 = t21*t5
       t28 = -1+t17
       t30 = sqrt(-t5*t28)
       t31 = Q*t30
       t32 = sin(t31)
       t35 = t9*t11*t30
       t40 = sin(Q*t11*t30)
       t46 = sin(2*t31)
       sf4 = -p*(-1+p)*(-
14*t4*t9*t5*t11+14*t15*t5*t11*t17+24*t22*t
11-2
     #4*t22*t11*t17-4*t32*t3*t35-
4*t40*t3*t9*t30-t46*t3*t35)*t3*t11/Q/t9
     #/t5/t28/72
       return
      end
```

Appendix E

Calculations to determine the scattering probabilities of the QE components:

The masses of the samples are m^{ATPB}=0.6g and $m^{ATPB\text{-}d}$=0.41g. N_A is the Avogadro's number ($6.022 \cdot 10^{23}$mol^{-1}), the radius of the sample container is r=2.5cm, the molecular mass of the samples are M^{ATPB}=337.25g/mol and $M^{ATPB\text{-}d}$=340.38g/mol. The scattering and the absorption cross sections are given in the ***Appendix*** C. The scattering probability of the 77% deuterated ammonium groups in the ATPB-d is

$$P_{sc}^{ATPB-d}\left[(D_4)_{0.77}(H_4)_{0.23}\right] = 1 - P_{tr}^{ATPB-d}\left[(D_4)_{0.77}(H_4)_{0.23}\right] - P_{abs}^{ATPB-d}\left[(D_4)_{0.77}(H_4)_{0.23}\right] = \exp\left[-\frac{4\cdot(0.77\cdot\sigma_{abs}^{D}+0.23\cdot\sigma_{abs}^{H})\cdot N_A\cdot m^{ATPB-d}}{M^{ATPB-d}\cdot\pi\cdot r^2}\right] - \exp\left[-\frac{[4\cdot(0.77\cdot\sigma_{sc}^{D}+0.77\cdot\sigma_{abs}^{D}+0.23\cdot\sigma_{sc}^{H}+0.23\cdot\sigma_{abs}^{H})\cdot N_A\cdot m^{ATPB-d}}{M^{ATPB-d}\cdot\pi\cdot r^2}\right] = 0.00364 \quad \text{Eq A-12}$$

The scattering probability of the ammonium groups in ATPB is

$$P_{sc}^{ATPB}\left[H_4\right] = 1 - P_{tr}^{ATPB}\left[H_4\right] - P_{abs}^{ATPB}\left[H_4\right] = \exp\left[-\frac{4\cdot\sigma_{abs}^{H}\cdot N_A\cdot m^{ATPB}}{M^{ATPB}\cdot\pi\cdot r^2}\right] - \exp\left[-\frac{[4\cdot(\sigma_{sc}^{H}+\sigma_{abs}^{H})\cdot N_A\cdot m^{ATPB}}{M^{ATPB}\cdot\pi\cdot r^2}\right] = 0.01768 \quad \text{Eq A-13}$$

Bibliography

[1] LATIMER, W. M. & RODEBUSH, W. H. (1920) *Journal of the American Chemical Society*. **Vol. 42**, 1419-1433.

[2] STEINER, T. & KOELLNER, G. (2001) *J. Mol. Biol.* **Vol. 305**, 535-557.

[3] LEVITT, M., & PERUTZ, M. F. (1988) *J. Mol. Biol.,* **Vol. 201**, 751-754.

[4] WORTH, G. A. & WADE, R. C. (1995) *J. Phys. Chem.,* **Vol. 99**, 17473-82.

[5] AUBRY, A., PROTAS, J., MORENO-GONZALES E. & MARRAUD, M. (1977) *Acta Cryst.* **B33**, 2573-2578.

[6] STEINER, T. & MASON, S. A. (2000) *Acta Cryst.* **B56**, 254-260.

[7] STEINER, T., MASON, S. A. & TAMM, M. (1997) *Acta Cryst.* **B53**, 843.

[8] NAKATSU, K., YOSHIOKA, H., KUNIMOTO, K., KINUGASA, T. & UEGI, S. (1978) *Acta Cryst.* **B34**, 2357-2359.

[9] STEINER, T., STARIKOV, E. B., AMADO, A. M. & TEIXEIRA-DIAS, J. J. (1996) *J. Chem. Soc. Perkin Trans. 2*, 67-71.

[10] DESIRAJU, G. R. & STEINER, T. (1999) *The Weak Hydrogen Bond in Structural Chemistry and Biology.* Oxford University Press.

[11] PERUTZ, M. F., FERMI, G., ABRAHAM, D., J., POLYART, C. & BURSAUX, E. (1986) J. Amer. Chem. Soc. **108**, 1064-1078.

[12] BURLEY, S. K., & PETSKO, G. A. (1985) Science, **229**, 23-29.

[13] BURLEY, S. K., & PETSKO, G. A. (1986) FEBS Letters, **203**, 139-143.

[14] ARMSTRONG, K. M., FAIRMAN & R., BALDWIN, R. L. (1993) J. Mol. Biol, **239,** 315-331.

[15] PERUTZ, M. F. (1993) Phil. *Trans. Soc. A.* **Vol. 345**, 105-112.

[16] PARKINSON, G., GUNASEKERA, A., VOJTECHOVSKY, J., ZHANG, X., KUNKEL, T. A., BERMAN, H. & EBRIGHT, R. H. (1996) *Nat. Struct. Biol.* **Vol. 3**, 837-841.

[17] KOLLER, J. (1999) *Acta Chim. Slov.* **Vol. 46(4)**, 493-500.

[18] PACE, N. C., (1990) Trends Biochem. Sci. **15**, 14-17.

[19] BAKSHI, P. K., LINDEN, A., VINCENT, B. R., ROE, S. P., ADHIKESAVALU, D., CAMERON, T. S. & KNOP, O. (1994) *Can J. Chem,* **72**, 1273-93.

[20] LECHNER, R. E. (1983) *Mass Transport in Solids.* Plenum Press, New York, *pp.169-226*.

[21] SQUIRES, G., L. (1978) Introduction to the Theory of Thermal Neutron Scattering. Cambridge University Press.

[22] LOVESEY, S., W. (1984) Theory of Neutron scattering from Condensed Matter. Oxford Science Publications.

[23] KOESTER, L., RAUCH, H., SEYMANN, E. (1991) Atomic Data and Nucl. Data Tab. **49,** 65.

[24] SEARS, V. F. (1984) Thermal-neutron scattering lengths and cross-sections for condensed matter research. Chalk River Nuclear Laboratories, Chalk River, Ontario, Canada.

[25] WESTERHAUS, W., KNOP, O. & FALK, M. (1980) *Can. J. Chem.* **Vol. 58.** 1355-1364.

[26] SCHUMAKER, N. E., GARLAND, C. W. (1970) *J Chem Phys.* **Vol. 53(1)**, 392-407.

[27] LECHNER, R. E. (1992) *Physica* **B180-181**, 973.

[28] LECHNER, R. E.et. al. (1996) *Physica* **B226**, 86.

[29] RUFFLE, B., OLLIVIER, J., LONGEVILLE, S., R.E. LECHNER. (2000) *Nucl. Inst. and Meth. in Phys. Res.* **A 449**, 322.

[30] LECHNER, R. E. (2001) JAERI-Conf 2001-002, Proceedings of the ICANS-XV Meeting Tsukuba 2000, Japan Atomic Energy Research Institute.

[31] SMIT, J. G., DACHS, H & LECHNER, R. E. (1975) Solid State Commun. 29, 219-223.

[32] RUFFLE, B. (2000) User Manual for Fitmo2 (Tof-Data Analysing Program). BENSC, Berlin.

[33] LECHNER, R. E. (1985) IAEA-CN-46/72P. Vienna.

[34] PRESS, W. (1981) *Springer Tracts in Modern Physics* **92**, Single-Particle Rotations in Molecular Crystals.

[35] SEARS, V. F. (1967) *Can J. Phys.* **45**, 237.

[36] RUBIN, J., BARTOLOME, J., ANNE, M., KEARLEY, G., J. & MAGER, A. (1994) *J. Phys. Condens Matter* **6**, 8449.

[37] MUKHOPADHYAY, R., GOYAL, P. S. & CARLILE, C. J. (1993) *Physical Review* **B 48**, 2880.

[38] LECHNER, R. E., BADUREK, G., DIANOUX, A. J., HERVET, H. & VOLINO, F. (1980) *J. Chem. Phys.* **73**, 934.

[39] A. DESMEDT, private communication.

[40] BÉE, M. (1988) *Quasielastic Neutron Scattering.* Adam Hilger, Bristol.

[41] ROBERTS, M. P., LUCAZEAU, G., KEARLEY, G. J. & DIANOUX A. J. (1990) *J. Chem. Phys.* **93**, 8963.

[42] BÉE, M., DIANOUX, A. J. & VOLINO, F. (1984) *Mol. Phys,* **51**, 221.

[43] ARRESE-IGOR, S., ARBE, A., ALEGRIA, A., COLMENERO, J. & FRICK, B. (2004) *J. Chem. Phys.* **120**, 423-436.

[44] BROWN, C. M. & MANSON, J. L. (2002) *Am. Chem. Soc,* **124**, 12600.

[45] JAYASOORIYA, U. A. & STRIDE J. A. (1996) *BENSC Experimental report*, Mechanism of Myon Spin Relaxation in Tetraphenyl Compounds of Group XIV Elements.

[46] LONGEVILLE, S. & LECHNER, R. E. (2000) *Physica B*, **183**, 276-278.

[47] AREE, T., OLLIVIER, J., SAENGER, W. & LECHNER, R. E. *to be published.*

[48] PRAGER, M., PRESS, W., ALEFELD, B. & HÜLLER, A. (1977) *J. Chem. Phys,* **67**, 5126.

[49] PRAGER, M. & PRESS, W. (1981) *J. Chem. Phys,* **75**, 494.

[50] PRAGER, M., SCHIEBEL, P. & GRIMM, H. (2002) *J. Chem. Phys,* **116**, 10338.

[51] KEARLEY, G. J., COCKCROFT, J. K., FITCH, A. N. & FENDER, B. E. F. (1986) *J. Chem Soc., **Commun.*****1040**, 1738.

[52] KEARLEY, G. J. & BLANK, H. (1988) *J. Chem. Phys Letters,* **89 (2)**,1199.

[53] HÜLLER, A. (1977) *Phys Rew. B,* **16**, 1844.

[54] HÜLLER, A. & PRESS, W. (1981) *Phys Rew. B,* **24**, 17
.

[55] SMITH, D. (2000) *Chem. Phys*. **264**, 145.

[56] PRAGER, M., PRESS, W., HEIDEMANN, A. & VETTIERS, J. (1984) *J. Chem. Phys,* **80**, 5126.

[57] ROBERTS, M., CAVAGNAT, R. M., LUCAZEAU, G. & STRAUSS, H. (1990) *J. Chem. Phys,* **93**, 7632.

[58] SMITH, D. (1994) *Chem. Rev.* **94,** 1567.

[59] ROBERTS, M., CLAVELL-GRUNBAUM, D. & STRAUSS, H. (1987) *J. Chem. Phys.* **87**, 6393.

[60] LUCAZEAU, G., CHAHID, A., BOCQUET, J. F., DIANOUX, A. J. & ROBERTS, M. P. (1990) *Physica* **B 164**, 313.

[61] ECKERT, J. & PRESS W. (1980) *J. Chem. Phys*. **73**, 451.

[62] ALLEN, P. S. (1974), *J. Phys.* **C 7**, L22.

[63] SVARE, I. (1979) *J. Phys.* C 12, 3907.

[64] WINDSOR, C. G. (1982) *Pulsed Neutron Scattering.* Taylor & Francis LTD, London.